DEVELOPMENT AND EVALUATION OF A PROCESS TO ISOLATE PICOLITRE COMPARTMENTS OF A MICROFLUIDIC BIOASSAY TO SEARCH FOR NEW MICROBIAL COMPOUNDS

Dissertation
for obtaining the degree of

DOCTOR RERUM NATURALIUM (DR. RER. NAT.)

submitted to the
Faculty of Mathematics and Natural Sciences
at the
Technical University Ilmenau
by

M. SC. THOMAS WEBER

SUPERVISOR
Prof. Dr. Johann Michael Köhler

REVIEWERS
Prof. Dr. Johann Michael Köhler
Prof. Dr. Andreas Schober
Prof. Dr. Marc Thilo Figge

DATE OF SUBMISSION
20.08.2018

DATE OF SCIENTIFIC DISCUSSION
29.04.2019

Dedicated to my beloved wife.

$2017 - \infty$

ABSTRACT

Microfluidic emulsion-based droplet systems have a great potential for inexpensive ultrahigh-throughput experimentation. Yet, picking single/unique picolitre-sized droplets of interest out of million others for upscaling and deeper analysis is still a fundamental limitation. In order to overcome this missing gap, a system was developed in which sorted droplets of interest are redirected into a capillary and pass through a refraction-based sensor before exiting. The signal of each droplet triggers a positioning algorithm that ultimately places the flowing droplet into an addressable compartment in either a microtiter plate or a Petri dish. Results indicate the effective isolation of a fraction of single droplets. However, it is crucial to monitor the droplet frequencies and flow rates, as multiple droplets can be deposited together if sorted within a short time interval. Nevertheless, the possibility to isolate a significant fraction of single droplets without disrupting the experimental workflow provides a necessary feature for interfacing droplet microfluidics with standard laboratory analysis and processing.

ZUSAMMENFASSUNG

Verglichen mit etablierten industriellen Hochdurchsatz-Anlagen entwickelten sich mikrofluidische, emulsionsbasierte Tropfensysteme in den letzten Jahren zu einer günstigen Alternative. Jedoch ist es derzeit nicht möglich, einzelne Tropfen im Pikoliter-Volumenbereich aus einer Vielzahl anderer Proben für anschließende Analysen zu isolieren. Diese Arbeit präsentiert ein Verfahren, um Tropfen mittels fluidischer Kanalstrukturen zu isolieren und über einen Brechungsindex-Sensor zu detektieren. Das erzeugte Signal ermöglicht eine automatisierte Einzelablage von Tropfen in adressierbare Kompartimente, wie beispielsweise in Petrischalen oder Mikrotiterplatten. Ergebnisse zeigen eine effektive Extraktion einzelner Tropfenfraktionen. Dennoch bedarf es einer kontinuierlichen Überwachung von Prozessparametern wie Flussrate und Tropfendurchsatz, um eine Trennung der einzelnen Tropfen zu gewährleisten. Gleichwohl bietet dieses online-Verfahren eine Möglichkeit, allgemeine Laborprotokolle und Analysetechniken mit Tropfenbasierter Mikrofluidik zu vereinen.

CONTENTS

LIST OF FIGURES

LIST OF ABBREVIATIONS

AM . . . .   Additive manufacturing
AMR . . . .   Antimicrobial resistance
API . . . .   Application Programming Interface
ASCII . . . .   American Std Code for Information Interchange
CW . . . .   Constant wavelength
CWI . . . .   Chip-to-world interface
DAQ . . . .   Data acquisition
DEP . . . .   Dielectrophoresis
DOI . . . .   Droplet of interest
DPSS . . . .   Diode pumped solid state
EBR . . . .   Edge bead removal
FEP . . . .   Fluorinated ethylene propylene
FPGA . . . .   Field programmable gate array
FWHM . . . .   Full width at half maximum
HF . . . .   Hydrofluoric acid
HVA . . . .   High-voltage amplifier
IDC . . . .   Inter-droplet candidate
LabVIEW® . . . .   Laboratory Virtual Instrumentation Engineering
                                    Workbench
Laser . . . .   Light amp. by stimulated emission of radiation
LC . . . .   Lucent connector
LOD . . . .   Limit of detection
MDR . . . .   Multidrug resistance
PDMS . . . .   Polydimethylsiloxane
PMT . . . .   Photomultiplier tube
PTFE . . . .   Polytetrafluoroethylene
PWM . . . .   Pulse Width Modulation
RIE . . . .   Reactive Ion Etching
RMS . . . .   Root Mean Square
SNR . . . .   Signal-to-noise ratio
SPICE . . . .   Simulation Program /w Integrated Circuit Em-
                                    phasis

Surfactant .... Surface active agent
TTL .... Transistor-Transistor-Logic
UL .... Universal Library

INTRODUCTION

1.1 THE POWER OF EVOLUTION

MICROORGANISMS were the first and still most ubiquitous forms of life due to their mere endless adaptability to any environmental condition. These pioneers of the earth were discovered in the late 16th century by van Leeuwenhoek and Hooke, but first scientifically explored almost 200 years later by Koch and Pasteur [1]. Until then, humankind unconsciously benefited from their basic ability to make a vast array of complex biomolecules from simple elements and compounds, *e.g.* by ethanol fermentation [2] or simply by their presence in the intestine [3]. Though, throughout history humans suffered infections from diseases (cholera, pest, tuberculosis) caused by the same life forms they were unaware of.

The discovery of penicillin by Fleming in 1928 was a serendipity that heralded the era of antibiotics. It seemed that the final frontier was reached and any infection could now be cured. However, evolution found and continues to find ways to overcome such microbial weaponry, as a penicillinase was already discovered 12 years after Fleming's find [4]. This makes in principle any active existing compound vulnerable due to selection pressure that leads to microbial adaptation [5]. Such processes can be significantly slowed down by medical treatments in a controlled way [7]. This knowledge, however, was discovered lately when antimicrobial and multidrug resistance (AMR/MDR) was already on the rise [8]. In 2014 the World Health Organisation stated that AMR is a "major threat to public health" resulting in millions of deaths per year [9]. Hence, new antibiotics and generally new natural bioactive compounds are urgently needed.

An exception to this rule appears to be teixobactin [6]

Over 90 % of all known antibiotics originate from the phylum *Actinobacteria* [10]. Interestingly, genomic analyses revealed that current findings in those culturable sources seem to be only the tip of the iceberg [11]. A literal treasure-hunt begun to discover all those promising active substances. Back then, manpower was step-by-step substituted with fully-automated 24/7 working robotic screening systems [12, 13]. This, unfortunately, led more to the introduction of modifications of known scaffolds than to new antibiotic classes [14, 15] with marginal success against AMR. In spite of the last years changed

strategy from molecular target screening approaches back to pheno-typic 'classical pharmacology' drug discovery [16], the lack of rapid and efficient high-throughput-screening (HTS) systems is still a major bottleneck [17]. Miniaturisation efforts that were performed to accelerate throughput and save consumables soon reached physical limitations and stopped further downsizing approaches.

1.2 PROMISING MINIATURISATION

With the development of inkjet-printing in the 1980s, steady interest of fluids on the micro scale arose [18] and resulted in a manifold of inventions like capillary electrophoresis [19], DNA-chips [20] and further lab-on-chip technologies [21]. These miniaturisation approaches became primarily popular due to their handy size that previously required bulky and expensive laboratory devices. Associated high surface-to-volume ratios enable shorter diffusion distances and therefore better mass transfer [22] allowing for accelerated and optimised processes like in chemical reactions [23, 24]. Also other sectors started using microfluidics, *e. g.* the food industry for safety analysis [25], medical settings for on-site patient monitoring [26] and biotechnology for microbioreactors [27].

The idea of microscopic two phase-based reaction vessels facilitated approaches to encapsulate and analyse a vast amount of different substances in a large number without high reagent consumption [28]. Pioneers like Quake and Whitesides developed techniques to manufacture micrometer sized channels and actuators, thus enabling a reproducible control of fluids [29, 30]. The development and introduction of *surfactants*[1] set the way for droplet-based microfluidics [31]. This permitted, for the first time, an easy bulk storage of encapsulated material and opened up unprecedented experimental possibilities reflected in a multitude of scientific reports on single molecules [32, 33], cells [34–37], organs [38] and whole organisms [39, 40].

Soon, the idea came up to substitute bulky and expensive state-of-the-art HTS systems with microfluidic droplet-based approaches (Figure 1 on the facing page), especially at the picolitre scale, to screen for millions of samples per day at still affordable costs (Table 1 on the next page).

Since then, a number of microfluidic screening setups have been realised in search of new antibiotics [42, 43], antibodies [44], optimised enzymes [45–47] and various cell cultivation strategies [48–52]. Hence, many techniques were developed to efficiently handle droplets for their specific tasks. Key operations include droplet generation [53, 54], splitting [55], fusing [56], injection [57] and sorting [58–60]. Yet, none of these are able to *easily* isolate a single droplet of interest (DOI)

---

1 Surfactant, a.k.a. surface active agents: an amphiphatic molecule that locates in-between two phases and lowers the surface tension.

Table 1: Comparison of classical HTS methods (cHTS) and droplet-based microfluidic approaches (µFL), adopted from Agresti *et al.* [41]

Descriptor	cHTS	µFL
Total reactions	5×10^7	
Reaction volume	100 µl	6 pl
Total volume	5000 l	150 µl
Reactions/day	73 000	1×10^8
Total time	≈2 years	≈7 h
Number of plates/device	260 000	2
Cost of plates/device	$520 000	$1.00
Cost of tips	$10 million	$0.30
Amortised cost of instruments	$280 000	$1.70
Substrate	$4.75 million	$0.25
Total cost	$15.81 million	$2.50

out of a million others to a specific external compartment. This can be wells of a microtiter plate (MTP) or Petri dish. Such a fluidic operation would be highly required in screening assays, upscaling approaches and the big omics field. The reason for its unavailability is that handling and detection of individual, fast flowing micro-sized droplets in a so-called *chip-to-world-interface* is hardly feasible.

The difference between a 1536 well plate (10 µl) and a picolitre droplet (100 pl) is more than five orders of magnitude.
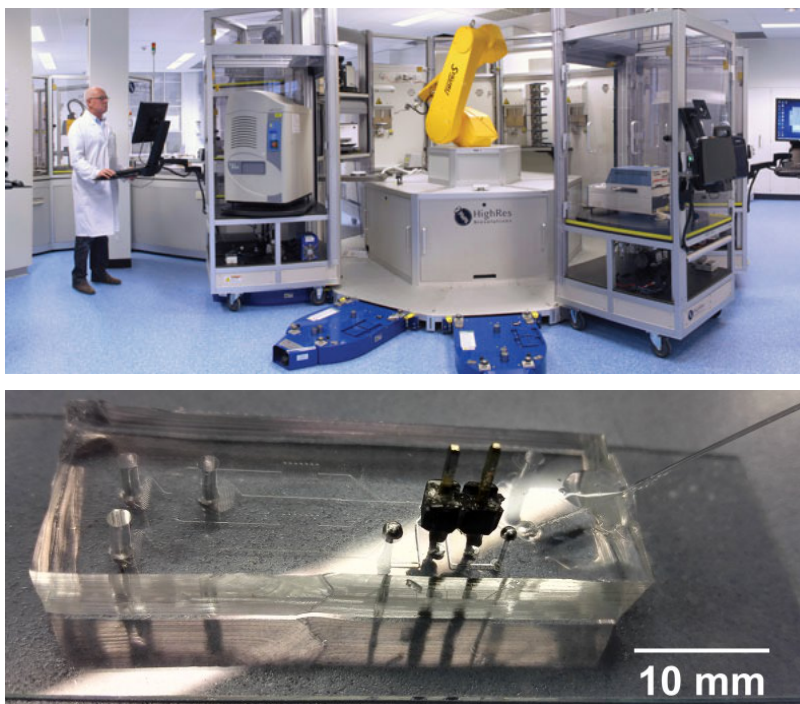
Figure 1: State-of-the-art high-throughput screening system (Pivot Park, Netherlands) compared to a microfluidic sorting chip on a microscope slide.

1.3   GOAL AND TASKS

To overcome the gap between nowadays limited HTS efforts and promising microfluidic droplet screenings, a fully automated process needed to be developed. This included the extraction, transfer and tracking of a single screened droplet of interest to a specific external location for further processing. It consisted of the following tasks to be accomplished:

a) Development of a microfluidic sorting structure to sort and lock-out single droplets of interest.

b) Establishment of a chip-to-world interface to transfer droplets to an external distinct position.

c) Development of a detection unit that recognises a single pico-litre droplet to trigger its own positioning and dispensing.

d) Design and development of necessary soft- and hardware to monitor and control an automated single droplet dispensing.

e) Combination, validation and characterisation of developmental stages a–d into a droplet screening process (Figure 2 on the facing page):

Figure 2: Schematic showing the process of single picolitre droplet screening. The workflow comprises droplet generation, incubation of microcultures in droplets, real-time sorting, transfer, sensing and depositing as well as subsequent analyses.

2

MATERIALS, METHODS, DEVICES AND COMPON-
ENTS

2.1 MICROFLUIDIC CHIP FABRICATION
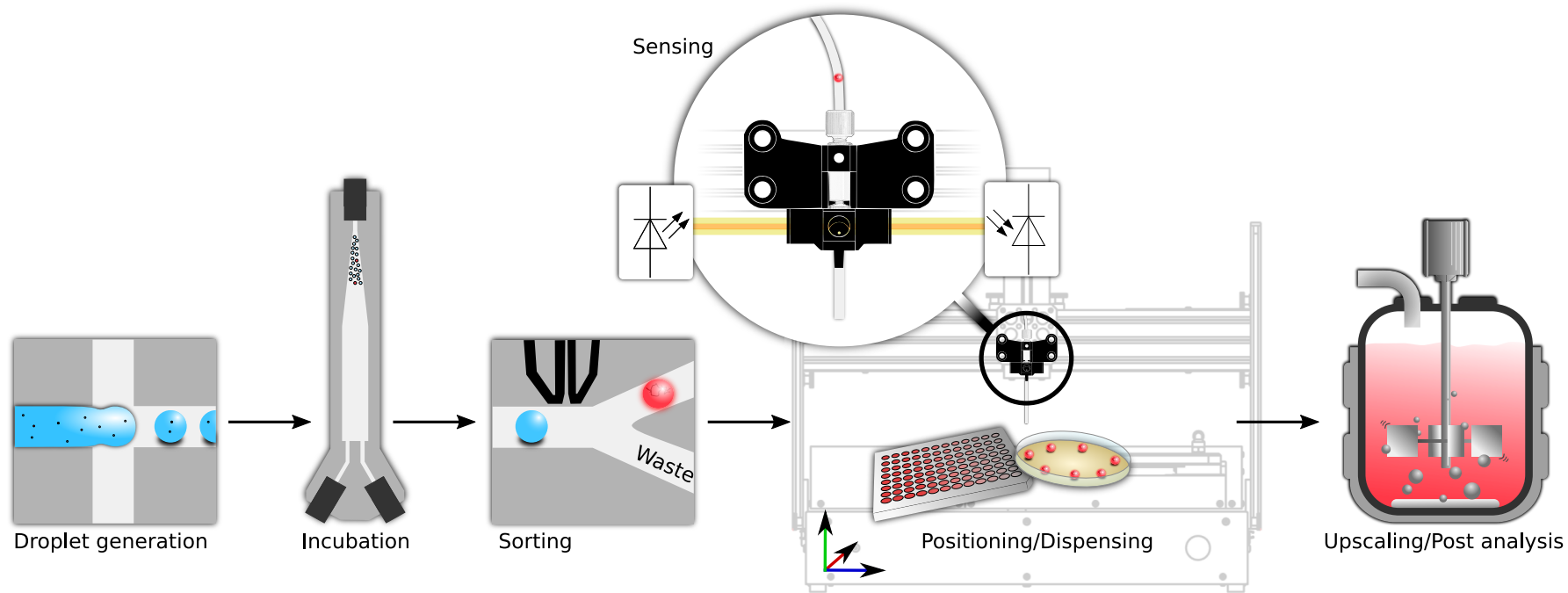
The general workflow for PDMS chip production can be divided into
five steps and are described in detail in the following sections.

1. Design of fluidic channel structures, stored as CAD file

2. Production of a high resolution photomask based on the CAD
   draft

3. Manufacturing of a master silicon wafer with prior printed chan-
   nel structures on the photomask (hard lithography)

4. Generation of PDMS stamp by using the silicon master mould
   (soft lithography)

5. Linking of PDMS stamp to a suitable (glass) matrix via plasma
   bonding.

2.1.1 Chip-design

Fluidic chip layouts were designed in-house using AutoCAD 2015.
Designs were then used to produce high-resolution emulsion photo
mask (128 000 dpi) by JD Photo Data (UK) for subsequent photolitho-
graphic production in-house or at Microstructure Facility (Technical
University Dresden).

2.1.2 Photolithographic master mould production

Photolithography was performed in three steps. Step one consisted of
pouring SU-8 2025 photoresist (Michrochem Corp.) on a three inch sil-
icon wafer (Silicon Materials, Germany) mounted on a self-made spin-
coater (see Section 3.4.3 on page 53). Coating was done by spinning
at 880 rpm for 50 s and subsequently 1600 rpm for 50 s to reach an
approximate coating thickness of 50 µm. A final spinning at 3000 rpm
for 6 s was conducted to remove residual edge beads (EBR). The resist
was then soft baked at 65 °C for three minutes and at 95 °C for five
minutes. In the second step the prior manufactured emulsion pho-
tomask was aligned on top of the coated wafer and fixed between

two fused-silica glass plates in a sandwich-like principle with strong paper clips. A self-made UV light source (see Figure 32 on page 55) was located on top of the wafer at an exposure time of 30 s at highest power ($\approx$ 780 mW). In the third and last step the exposed wafer was post-baked for five minutes at 95 °C and subsequently developed in SU-8 developer (Microchem Corp.) for five minutes on a rocker (IKA®-Werke GmbH) at an agitation rate of 100. Undeveloped resin was washed away via isopropyl alcohol for ten seconds. Developing and washing steps were repeated until resin debris was completely removed.

2.1.3 Soft lithographic chip production

Soft-lithographic chip production was performed by pouring a 1:10 mixture of degassed silicone elastomer Sylgard 184 (Dow Corning) and curing agent on the developed silicon wafer followed by a four hours heat treatment at 70 °C. After polymerisation of PDMS replica, fluidic connections were made using 0.35 mm biopsy puncher (World Precision Instruments) for capillary outlet, 0.5 and 0.75 mm biopsy puncher (Harris Uni-Core) for electrodes and 1.5 mm biopsy puncher 15110-15 (Ted Pella) for 1/16″ PDMS tubing. PDMS bonding was performed by oxygen plasma treatment for thirty seconds at 50 % relative power and 0.3 mbar oxygen in a Zepto plasma oven (Diener electronic). Subsequent heat treatment was applied for thirty minutes at 65 °C on soda-lime glass object slides 0656 (Roth) for droplet generation and one-sided ITO coated glass slides CG-51IN-5204 (Delta Technologies Inc.) for dielectrophoretic droplet sorting. Microfluidic channels were hydrophobised by injecting Novec 1720 fluorosilane polymer (3M), followed by heat treatment on a heating plate MR 3001 (Heidolph) at 150 °C for ten minutes. Electrodes were manufactured by inserting the low melting Indium Alloy 19 (Indium Corp.) into the glass bonded PDMS chip at 100 °C.

2.2 FLUIDS AND ACTUATION

While generating and reinjecting droplets Novec HFE-7500 (3M) perfluorinated oil with 0.5 % (v/v) Pico-Surf I (Dolomite) was used as continuous phase. Droplet spacing was achieved by using perfluorinated oil with < 0.5 % (v/v) surfactant. Dispersed phase consisted of culture growth media (LB or TB) with 1×10^{-6} spores of cells per millilitre and the block copolymer Pluronic® F-68 (Gibco) at 10 % (v/v) to lower unspecific cell and protein adhesion to PDMS. All fluids were actuated by pressure pump OB-1 MK2 (ELVESYS®), pressure pump MFCS™-EZ (Fluigent) or syringe pump neMESYS (CETONI) and guided to the chip using PTFE tubing (d_o/d_i = 1/16″/0.25 mm).

2.2.1 Droplet populations

To evaluate the system's performance, three different droplet populations were generated in a microfluidic chip with flow-focusing geometry:

POPULATION 1: *Escherichia coli* ECJW992 carrying an expression plasmid for the fluorescent protein mCherry and an amp^R gene [61] at OD_{600} = 1 ($\approx 1 \times 10^9$ cells/ml) in medium containing 0.2% (v/v) ampicillin.

POPULATION 2: *E. coli* ECJW992 as in 1) with an additional fluorescein label at c = 0.5 g/l, used to set-up sorting at droplet ratio of 1:10.

POPULATION 3: The to-be-sorted population of droplets with fluorescent polystyrene microparticles (Distrilab) at c = 1.25×10^8/ml, 1% (v/v) tetracycline and an additional fluorescein label (c = 5 g/l). This population was generated at an observed ratio of 1:75 to the other droplets.

Plates/Petri dishes for subsequent droplet dispensing were prepared with either LB agar medium plus 100 µg/ml ampicillin or Chromocult® Coliform agar medium (Merck) with equal amounts of ampicillin to detect *E. coli* and coliform bacteria.

2.3 OPTICAL SET-UP

All experiments were conducted on an inverted Axio Observer.Z1 (Carl Zeiss) microscope. Droplet fluorescence signals for sorting were acquired by coupling and positioning a DPSS Laser (LASOS) at λ 488 nm into the workstation via DirectFRAP (Carl Zeiss). Emitted fluorescent light was extracted by utilising optical filters (AHF analysentechnik) and split using a beam splitter cube (Thorlabs) equipped with a dichroic mirror (variable wavelength). Filtered light was directed to a detector (PMT module H10723-20/H10721-20 (Hamamatsu Photonics) or a silicon photodiode detector) and a camera.

An InGaAlP light source type QL65D7S-A-L (Quantum Semiconductor Intl. Co.) was used for the refraction sensor. It was boxed and configured to be used with a single mode fibre, equipped with an universal 2.5 mm connecting ferrule and a visible light output at λ_p = 650 nm at typical fibre coupling power of 500 µW (IMM Photonics GmbH, Germany).

2.3.1 Droplet imaging

Depending on the experimental purpose, imaging was performed by various cameras coupled to the Axio Observer.Z1 microscope. High-speed recordings at high resolution (4 MP) were done using a Mikrotron EoSens® 4cxp camera. Standard colour imaging was performed

by an acA1920-150uc (Basler) camera. Low-speed yet high-quality monochromatic droplet imaging was conducted by a PIKE F032-b/c (Allied Vision Technologies) camera. For imaging of stationary droplets in observation chambers a pco.edge 5.5m (PCO) was employed. Image recording at positioning system site was performed by utilising a DigiMicro 2.0 camera (dnt).

2.4 SORTING SET-UP

Dielectrophoretic sorting was accomplished either via absorbance-based signals, fluorescence-based signals or counting threshold-based (see Listing 2 on page 97, appendix). Generated TTL-signals from a Schmitt-trigger based circuitry or microcontroller were fed to a function generator trigger input (Agilent/Keysight 33210A) that was configured to perform a burst output of square-wave signals between 4–6 kHz and 350–450 mV$_{pp}$. Cycle bursts were set according to droplet throughput and spacing rate between 20 and 40. The output was amplified via a TREK-623b high-voltage amplifier (HVA) at factor 1000 and sent to electrodes on-chip. ITO-coated glass slides were grounded using earthed alligator clamps.

2.5 SIMULATIONS

2.5.1 Refraction-based droplet sensing

Optical simulations of the refraction-based sensor were performed using TracePro® 6.0 (Lambda Research). The sensor installation was simulated by constructing a three-dimensional model (Figure 3) using the following parameters: 1) A circular-shaped optical multi mode fibre of d = 50 µm delivering unpolarised light with a NA of 0.22 having a Gaussian beam profile with uniform flux and weighted position and angle. A random annular pattern was chosen as origination for 10 000 rays at λ 650 nm with a total flux of 1 mW; 2) A cylindrical capillary, positioned 500 µm away from the optical fibre consisting of an outer coating simulating fluorinated acrylate (TSH, n = 1.415), a capillary body made of fused silica (n = 1.45654) and an inner channel filled with NOVEC 7500 oil (n = 1.287); 3) A water sphere (droplet) of different diameters (n = 1.33136); 4) An optical opposite located detecting single mode fibre of 9 µm circular diameter made of fused silica, positioned 500 µm away from the capillary and used for irradiance measurement. Scheme, a dialect of the LISP language [62], was used in conjunction with TracePro to automatically change object properties enabling the simulation of droplet and capillary movement. It furthermore automated raytracing computations and was used for data extraction.
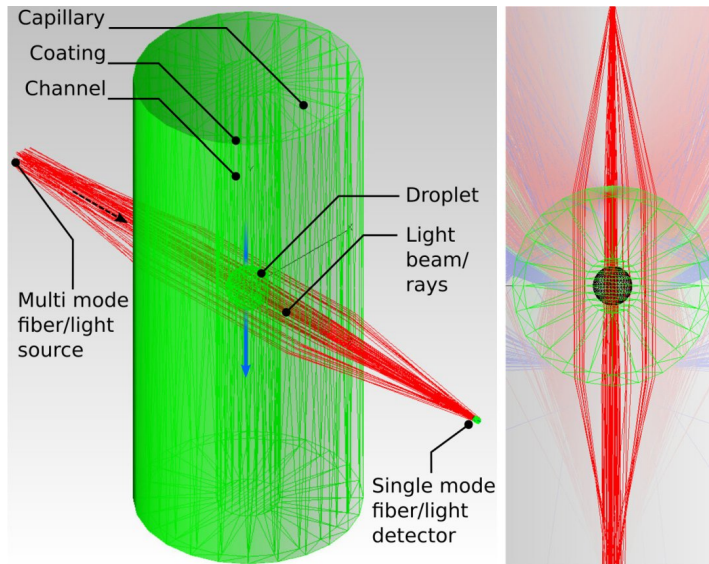
Figure 3: Setup of raytracing simulation of the refraction sensor. Left: 3D-model of the experimental setup with selected rays that hit the light detector. Right: 2D-view from top showing all additionally generated, reflected and refracted rays in different colours at reduced opaqueness.

2.5.2 DEP-based sorting

Studies on droplet behaviour at DEP-based sorting events were performed using COMSOL Multiphysics 5.3 (Comsol AB), a software that utilises the finite element method (FEM)—a numerical simulation approach. There, 2D-channel and electrode structures were imported via AutoCAD using the R12/LT2 DXF format. Four physics modules were applied in a primary study to solve fluid dynamics at steady-state conditions and the electrical potential on the frequency domain (1. stokes/creeping flow at no slip boundary condition, 2. electric currents, 3. particle tracing for fluid flow including drag forces and DEP-forces and 4. fluid-particle interaction). In a subsequent time dependent study the acquired solutions were used to estimate particle trajectories without and with applied DEP-forces. Aqueous droplets were emulated as cell-like compartments with a thin 8 nm dielectric shell [63]. The applied carrier fluid was parametrised as NOVEC 7500 oil. All further necessary parameters are listed in Table 2 on the following page.

2.6 DATA ACQUISITION AND ANALYSIS

Experimental data was acquired by various data acquisition cards, particularly USB-1608FS, USB-1608FS-PLUS and USB-1608GX (Measurement Computing). Analogue signals from light detectors, trigger circuits and other sources (HVA, lock-in amplifier) were sampled at

Table 2: Parameters for FEM-based droplet sorting simulation.

Medium conductivity in S/m		Dynamic viscosity in $Pa{\cdot}s$	
Fluid	0.055	Fluid	$1.2428{\cdot}10^{-3}$
Particle	0.1	Particle	$6.71{\cdot}10^{-3}$
Shell	$1{\cdot}10^{-6}$		
Relative permittivity		**Velocity in m/s**	
Fluid	5.8	Primary oil	$2{\cdot}10^{-2}$
Particle	80	Biasing oil	$6{\cdot}10^{-3}$
Shell	6		
Density in kg/m^3		**Miscellaneous**	
Fluid	1614	Particle diameter	$6{\cdot}10^{-5}$ m
Particle	1000	Shell thickness	$8{\cdot}10^{-9}$ m
		DEP frequency	$5{\cdot}10^{6}$ Hz
		DEP voltage	± 65 V

10 kHz and ± 10 V input voltage range. An in-house written software was used for data acquisition (see Section 3.4.2 on page 49).

2.6.1 Peak recognition

Raw data was processed by subtracting baseline signals based on a noise filter that was calculated by the sum of the signal mean value and a multiple of its standard deviation. Filtered signal data was then applied to an algorithm[1] in R [64] that detects peaks in multiple steps (Listing 1). Firstly, the difference between consecutive data points is calculated (*diff*), the resulting algebraic sign extracted and binarised (*sign*) and again differences computed. Secondly, predecessors z and successors w of detected peaks x are calculated with an adjustable parameter m. A final validation evaluates if detected peaks are signal or noise related. This was accomplished by the afore computed values of w and z.

Listing 1: R-code for peak detection

```r
find_peaks <- function (x, m = 7){
    shape <- diff(sign(diff(x, na.pad = FALSE)))
     pks <- sapply(
       which(shape < 0), FUN = function(i){
         z <- i - m + 1
         z <- ifelse(z > 0, z, 1)
         w <- i + m + 1
         w <- ifelse(w < length(x), w, length(x))
         if(
           all(
             x[c(z : i, (i + 2) : w)] <= x[i + 1]
               )
```

---

1 developed by Lisa Mahler

```
13          ) return(i + 1)
14          else return(
15                  numeric(0)
16              )
17      } #end which
18    ) #end sapply
19  pks <- unlist(pks)
20  pks
21  }# end find_peaks
```

2.6.2   SNR calculation

The signal-to-noise ratio (SNR) was computed by dividing experimental data into two subsets. One subset contained only baseline signals (see Section 2.6.1 on the preceding page) whereas the second subset comprised of peaks that were found via the aforementioned peak detection algorithm. The SNR (db) was then calculated using the following formula:

$$\text{SNR}_{\text{db}} = 20 \cdot \log_{10}\left(\frac{\text{RMS}_{\text{Peaks}}}{\text{RMS}_{\text{Noise}}}\right) \tag{1}$$

$$= 20 \cdot \log_{10}\left(\frac{\sqrt{\sum_i^N \left(\frac{p_i^2}{n_i}\right)}}{\sqrt{\sum_i^N \left(\frac{x_i^2}{n_i}\right)}}\right) \tag{2}$$

Here, RMS refers to the root mean square, p_i to a peak value (detected local maximum) and x_i to a noise value, i.e. all data below signal average minus two times signal standard deviation.

2.7   HARDWARE COMPONENTS

2.7.1   Photodetector control circuit

This circuit is originally based on a design by Matthias Urban (Leibniz IPHT Jena) and was modified marginally to fit the experimental purpose (Figure 44 on page 93). It consists of a silicon photodiode adapted to human eye sensitivity (400–800 nm), a transimpedance amplifier to convert the output current into voltage and a programmable amplifier including a RC bandwidth filter switch (1/40 kHz). Similar to the electronic trigger circuit, a PCB for the transimpedance circuitry was designed in Target 3001! and manufactured at Beta LAYOUT. The amplifier circuit design was copied with permission from M. Urban and manufactured at Beta LAYOUT. All components used for the photodiode PCB and the amplifier circuit are enlisted in Table 7 on page 95 (appendix).

2.7.2   Schmitt-Trigger and valve controller

All components used to build a Schmitt-trigger-based circuit for TTL-conversion of experimentally derived analogue signals to digital ones

are listed in Table 8 on page 96 (appendix). For it's development please see Section 3.4.1 on page 48. Every electronic component used for the assembly of the valve controller are listed in the same table (appendix). For its development please see Section 3.4.4 on page 54.

RESULTS

Within this chapter a detailed summary of every developmental phase is given that was necessary to reach the goal of a single droplet dispensing system. This can be divided into five phases (see also Section 1.3 on page 4). In the initial phase, efforts were made to establish a fluidic sorting structure to reproducibly reroute DOIs at real-time. The second phase focuses on the establishment of an interface that enables the transport of sorted DOIs out of the microfluidic chip to a specified target. To automate the subsequent single droplet dispensing, a detection unit needed to be constructed, which is described in the third phase. Last but not least, the fourth phase explicates all soft- and hardware developments that were necessary to control, monitor and automate the aforementioned processes. The fifth stage describes steps to characterise, validate and optimise all components when assembled together in the final setup.

```
┌─────────────────────────────┐
│  1. Development of fluidic   │
│     sorting structures       │
└─────────────────────────────┘
              │
              ▼
┌─────────────────────────────┐
│  2. Establishment of a       │
│     chip-to-world-interface  │
└─────────────────────────────┘
              │
              ▼
┌─────────────────────────────┐
│  3. Construction of a        │
│     single droplet detection unit │
└─────────────────────────────┘
              │
              ▼
┌─────────────────────────────┐
│  4. Soft- and hardware/      │
│     Process control and automation │
└─────────────────────────────┘
              │
              ▼
┌─────────────────────────────┐
│  5. System evaluation        │
│     and characterisation     │
└─────────────────────────────┘
```
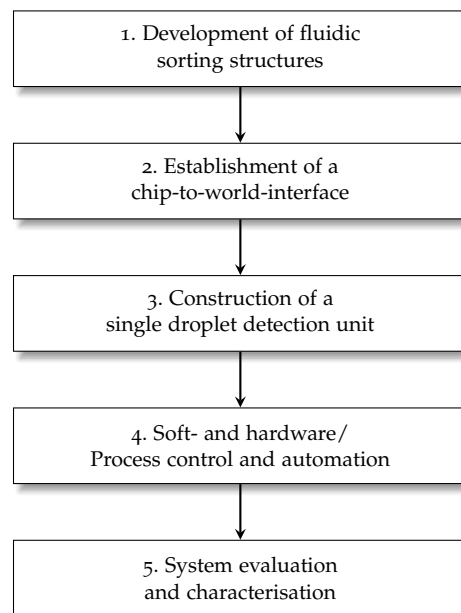
The goal of rerouting a micrometer-sized DOI from a microfluidic chip to an external location should not be considered a trivial problem. To illustrate that in a better way and understand the complexity of the system, the following facts should be kept in mind:

- The surfactant-stabilised DOI is a liquid and fragile object with a diameter of $< 100\,\mu m$ prone to break at certain external forces.

- The DOI selection takes part in a microfluidic sorting unit, *i. e.* a miniaturised and automated screening system, where possible hits are selected at a throughput of hundreds of droplet samples per second.

- The distance between microfluidic chip and positioning area necessitates a transfer that guarantees the integrity of a single droplet.

- Due to the unknown time a sorted droplet arrives at the fluidic outlet, an object detection unit needs to be integrated to control a single DOI positioning and dispensing. This sensor should neither interact with the droplet nor influence it. It should furthermore be able to differentiate between a single picolitre droplet of interest, possible satellites (split former droplet parts at femtolitre level ($\varnothing \leqslant 10\,\mu m$)) and groups of droplets to ensure only single droplets of correct size to be dispensed.

- All processes can barely be observed by the naked eye and impossibly controlled manually, therefore requiring a fully automated supervision.

3.1   FLUIDIC SORTING STRUCTURES FOR SINGLE DROPLET DISPENSING

The reader should be advised that most of the here presented developments occurred simultaneously in time. As the nature of reading does only allow for a serial information flow, it was sometimes all but impossible to not reference certain future topics.

Conducting a microfluidic screening process requires a structure suitable to separate DOIs from a flowing bulk. Such a structure can be imagined as a T-junction where one incoming channel splits up into two outgoing ones. The separation process can then ultimately be realised by a droplet deflecting unit. In reality however, a reliable sorting structure is much more sophisticated and depends on many conditions that need to be fulfilled. The following example should help in understanding those requirements:

Assuming that in a real screening process at a throughput of one hundred droplets per second one rare hit per one million samples occurs. This translates to one sorting event in almost three hours. During this time a sorting unit needs to work flawlessly (no false positive and/or negative events), even at significantly higher droplet throughput rates. Various setup parameters affect this sorting process, *e. g.* a transferring tube that lead DOIs from the chip outlet to a suitable dispensing location. Due to its length and the applied dispensing mode the tube exit might generate fluctuating pressure states that influence the upstream situated sorting. Hence, microfluidic droplet picking becomes a dynamic pressure regulated process that needs an active feedback control and instant monitoring but should in an ideal case

also compensate fluidic variations passively. The development and evaluation of sorting structures for this special application ideally require a proper screening. Due to practical reasons a simplified and well-thought-out model needed to be established.

3.1.1 A matter of inter-droplet distance enlargement

An artificial screening that helps to develop a precise droplet sorting and positioning system would be the mimicking of DOIs arriving in time intervals in the range of seconds at the fluidic dispensing outlet. This temporal distance is defined by physical limitations of the downstream located positioning unit (event processing >1 Hz). A simple commercially available T- or cross junction is not able to separate two proximate DOIs by a secondary carrier oil stream to high inter-droplet distances above 1 Hz. This is due to the crossing's insufficient inner diameter that by far exceeds the here used droplet diameter ($d_T \gg d_{DOI}$) and is described more in detail in a later section 3.2.3 on page 27. One straightforward method to overcome this issue can be the use of chip-based fluidic reinjection structures at droplet scale (here at $\approx$50 μm channel width). However, these result in a very limited inter-droplet distance between two proximate droplets of $\ll$ 1 s. While this strategy was sufficient enough for Küster *et al.* [65] to sequentially dispense and position droplets at comparably high speed (4 Hz) and low inter-droplet distance of up to 140 ms, their application for MALDI-MS sample acquisition differed significantly and did not target a screening-like goal. A more complicated yet promising strategy would be the use of sorting structures. Those were apparently developed for a purpose of selection but might serve as efficient enlargement units for the inter-droplet distance.

Many fluidic channel designs already exist [66–69] and were successfully implemented in multiple applications [70, 71]. Yet, applying those in an own setup mostly needs adaptation due to different manufacturing processes, materials, used liquids/chemicals, pressure regimes, droplet size as well as the applied principle of sorting. Commercially available cell sorters might do the job. However, this requires—beside the device itself—a hydrophilic droplet shell [72] that introduce a significant amount of complexity but also huge restrictions to the system. Developing a suitable microfluidic sorting unit is therefore the most straightforward approach. Chips previously used at the microfluidic laboratories of HKI were manufactured by LioniX BV (Netherlands) via reactive ion etching (RIE) in fused silica as substrate. Channel properties included minimum structural details below 10 μm with a depth of 50 μm. Droplet deflection was accomplished by applying dielectrophoretic (DEP) forces that implied the integration of electrodes. Those structures were also manufactured via RIE on a separate layer following sputtering treatment for metal deposition [60] (Figure 4 on the next page). This approach had many ad-

vantages regarding re-usability, stability and bio-compatibility. However, high production costs and time, troublesome connectivity and maintenance as well as a limited observability and electric shielding performance made it unattractive and inflexible when evaluating new designs. A rapid development of fluidic sorting structures including an optimisation of existing issues therefore required a drastic change in chip production. With the nowadays widespread application of PDMS-based microfluidic chips [30, 73] hard-lithography manufacturing on silicon substrate was established to make it less cost-intense and more flexible. By this approach it was now possible to produce new polymer-based chip generations in approximately three weeks while the previous method for glass chips took more than three month.
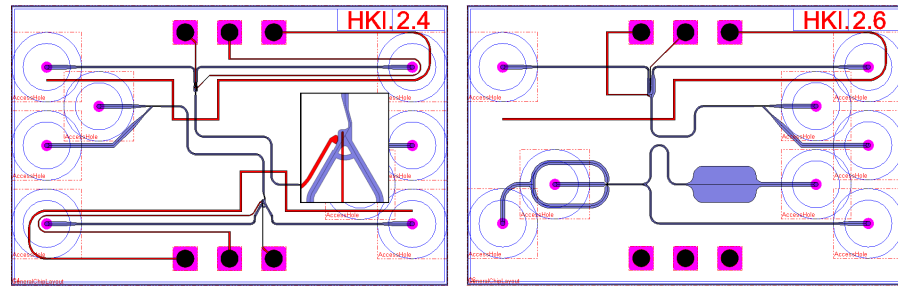

Figure 4: Two examples of a previous chip generation made of fused silica via RIE at LioniX BV (Netherlands).

Various parameters influence the behaviour of a precise, reproducible and long-term stable sorting. The hydrodynamic pressure regime is primarily based on the geometry/the capacity of every fluidic channel, the fluid itself and therefore the hydrodynamic resistance. The resulting system pressure/flow rate is then actively controlled by pumps using feedback loop control engineering (PID or PID-like approaches). Apart from fluid dynamics comes electrokinetics. DEP-forces influence the droplet's trajectory due to an electric field dispersion by sorting electrodes. Their shape and position introduce further complexity into a microfluidic system.

All such structures were targeted for optimisation by performing empirical studies based on previous experimental results, *i. e.* by modifying various channel and electrode geometries that have a major impact on the sorting behaviour. This included droplet spacing structures to generate a spatial gap between two adjacent reinjected droplets without inducing shear forces that might break droplets and additionally control their trajectory at sorting site (biasing). Further structural examinations comprised the bifurcation wall's curvature [59], the channel width and depth of the two chip outlets, the outlet's geometry itself and the above mentioned electrode design (Figure 5 on the facing page). In addition, electrode pairs were placed on both channels sides inspired by a publication of Frenzel and Merten [74],

who developed a strategy to actively sort DOIs as well as non-DOIs into their intended channels. One of many empirically developed sorting structures was extensively tested positive regarding spacing, biasing, pulling efficiency and outlet control (Figure 5, bottom left) and is described in more detail in the following section.
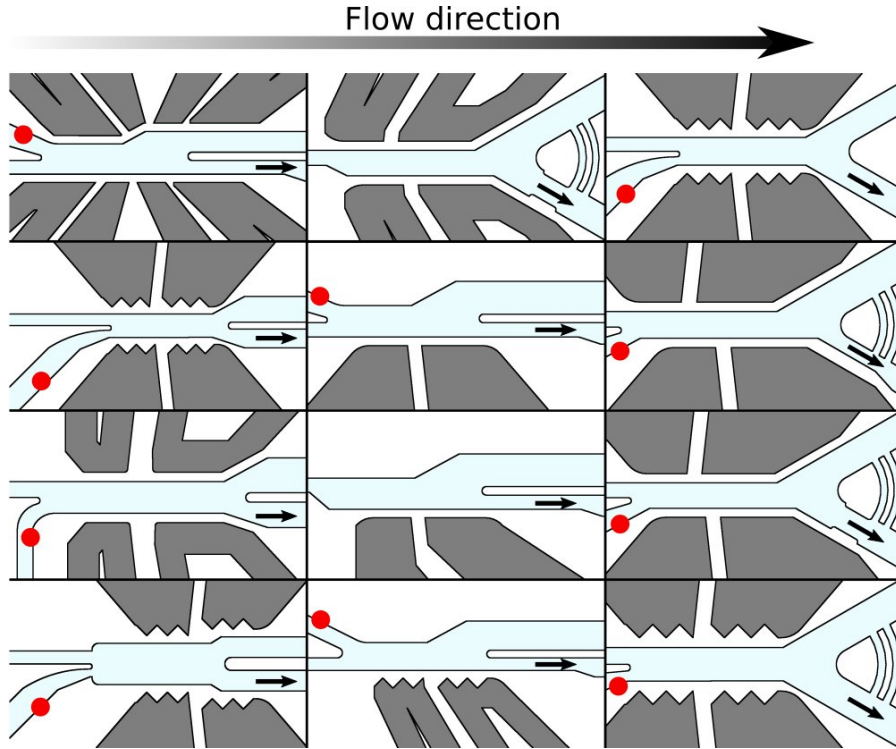

Figure 5: Prototypes of fluidic sorting structures for the final picolitre droplet sorting, sensing and positioning approach. Light blue coloured section marks fluidic channel region, electrodes are drawn grey, red dots mark the biasing channel and black arrows depict positive sorting outlets. Empirical studies showed design at bottom left as most efficient sorting structure.

3.1.2 Optimised sorting structure

The developed and optimised sorting structure includes a cross-sectional primary spacing unit with chamfered outlets (not shown) to a $50\,\mu m$ constricted channel that leads to the sorting area (Figure 6 on page 21, top right), *i.e.* a $160\,\mu m$ high and $500\,\mu m$ long sector—the relaxation zone—equipped with electrode structures on top and bottom. Using equal-sized channel outlets and a biasing channel, the droplets trajectory was assumed to be controlled more precisely and with greater flexibility then before.

Analyses of high-speed recordings and flow simulations in a previous chip generation (Figure 6 on page 21, top left and bottom A) and in the optimised sorting design (Figure 6, top right and bottom B) proofed the hypothesized structural optimisation efforts. In both ex-

amined structures, incoming droplets undergo a shape deformation upon entering the sorting site due to an abrupt change in pressure (relaxation zone) and continue to flow towards a predominant direction along distinct streamlines[1] shown as gray solid lines. As the geometry of the relaxation zone affects the droplet velocity, a certain impact energy combined with the shape of the bifurcation was observed to affect the droplet's integrity. The optimised structure was therefore equipped with a wider relaxation zone that significantly slows down incoming droplets (see simulations: 20 mm/s (old design), 13 mm/s (new design)) to have a more accurate control over the droplet's trajectory and a wider bifurcation area (30 μm (old), 50 μm (new)) that minimised splitting events. In addition, the shape of electrodes were changed to zig-zag-like structures, resulting in increased local field strength due to acute geometries and simultaneously broadened electrical field dispersion. Further shifting of electrodes proximate to the bifurcation zone significantly decreased the escaping of already sorted droplets as seen in prior sorting designs due to prevalent pressure/flow state (not shown). Equalizing microchannels at the bifurcation zone in the previous chip design were added to further resolve this issue (see Sciambi *et al.* [59]), but were discarded as no further improvements could be observed. During sorting, void droplets are intended to passively move to the waste-defined channel or in case a DOI occurs, to be actively deflected towards the positive channel via DEP-forces. As previous chip generations comprised a constriction on the positive channel (20 % reduced width compared to the negative channel), a predominant direction bias occurred towards the negative channel distant from the bifurcation area. This was intentionally designed to regulate sorting efficiency by minimising false positive hits, but due to the actual setup's capillary connected to the positive outlet an additional pressure increase occurred. As a result, an even stronger biasing behaviour towards the waste channel took place that decreased the efficiency of the DEP-based sorting process. Further pressure adjustments were therefore necessary to adapt the predominant flow regime. Hence, the optimised chip generation was designed with two equal-sized outlets. This optimised design was experimentally tested in sorting and positioning experiments of eight hours duration (see Section 3.5 on page 62).

Note: Effects of electromagnetic fields on biological samples were not investigated during this work.

3.2 CHIP-TO-WORLD-INTERFACE

Microfluidic applications mostly require unique interfaces by means of fluidic, optical or electrical connections. Thus, a variety of so-called chip-to-world-interfaces (CWI) have been developed [75–77]. In this work a unique droplet transition needed to be invented to guarantee

---

1 Layers of certain velocities slipping on top of each other due to a laminar flow regime.
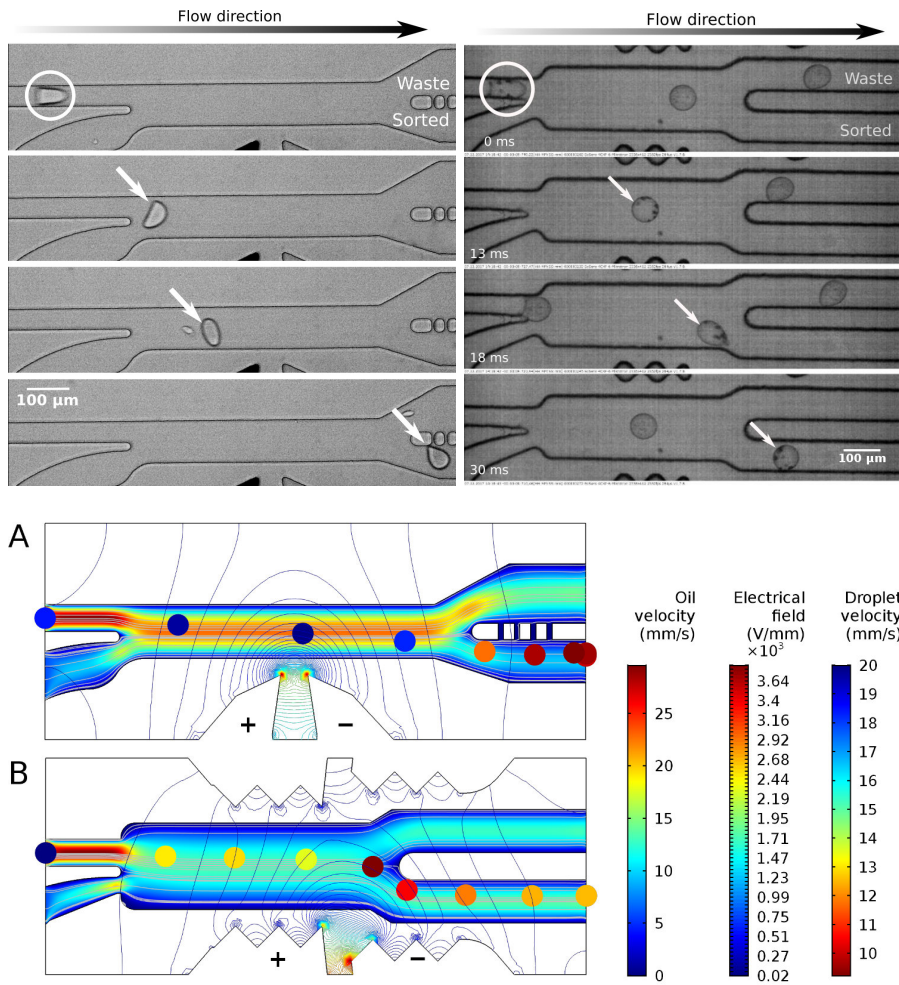
Figure 6: Theoretical and practical analyses of droplet behaviour during DEP-based sorting. Top: Sorting on a previous (left) and optimised sorting structure (right). The upper right channel depicts the direction to waste, the lower channel guides sorted droplets. Dark coloured structures on top and bottom depict electrodes where, in case of the optimised structure, only the lower entity triggers the generation of electrical fields. The biasing channel is shown on bottom left. Bottom: Simulation of DEP-based particle sorting inside two microfluidic structures using COMSOL Multiphysics. A) shows previous used sorting structure and B) the optimised design. Streamlines are shown in gray, the fluid velocity is depicted in colours from blue (low speed) to red (high speed). The particle velocity colour is illustrated inverse for better contrast (red: low speed, blue: high speed). The electrical displacement field is shown as a coloured contour with blue as lowest and red as highest density. A plus sign indicates the electrode's positive terminal whereas a minus sign shows the negative pole.

a reliable and robust single DOI transfer from a chip onto a suitable external location. Crucial prerequisites were to ensure the droplets integrity, to maintain spatial and temporal information as well as to sense a droplet while being transferred. Various efforts were ventured to understand and control the droplet flow inside a tubing for a CWI assembly. This included theoretical studies on hydrodynamic resistance, practical transfer studies in different sized tubings of various materials as well as transition approaches to ensure single picolitre droplet tracking.

The former glass chip generation (Figure 4) required a flexible polymer tube with an OD of 1/16" for a proper connection. As later sections will show, picolitre droplet sensing is not possible in those tubings. Hence, droplet transport was assumed through two transitions: 1) The transfer of droplets from chip into the polymer tubing and 2) the interface to a sensing tubing, *i. e.* a highly translucent pipe. Hence, for choosing the right geometry and estimating a resulting pressure drop, preliminary theoretical pressure studies were conducted.

3.2.1   Pressure studies

Based on the equation of motion, the Navier-Stokes equation can be used to describe the motion of of incompressible, viscous fluids [78]. This enables to illustrate the flow in a microfluidic system, where fluids are pressure-actuated inside a rigid channel to an assumed steady-state flow. For a channel with circular cross-section, the non-linear differential Navier-Stokes equation then simplifies to the law of Hagen-Poiseuille (Equation (3))

$$\Delta p = R_h \, Q = \frac{128 \, \mu \, l}{\pi \, d^4} \, Q \tag{3}$$

where Δp describes the pressure difference between beginning and end of the considered tubing, R_h the hydrodynamic resistance, Q the volumetric flow rate, μ the dynamic viscosity of the fluid, l the length of the tubing and d the tubing diameter. With this, a pressure drop simulation of tubing with different length and diameter at a constant flow rate of carrier fluid can be performed (Figure 7 on the facing page). With an expected transfer length of 800 mm and a default inner diameter of 250 µm, the generated hydraulic resistance/pressure drop stays below 100 N/m² (100 Pa). Due to d^{-4} the impact on the pressure drop becomes more significant the smaller the inner diameter.

Considering a setup with two connected straight channels of differing diameters (PTFE-tubing and glass capillary), the pressure drop can still be approximated as Poiseuille flow, as long as a laminar flow regime (small Reynolds number) is assumed. In that way, serial hydraulic resistances can be added up like in electric circuits to
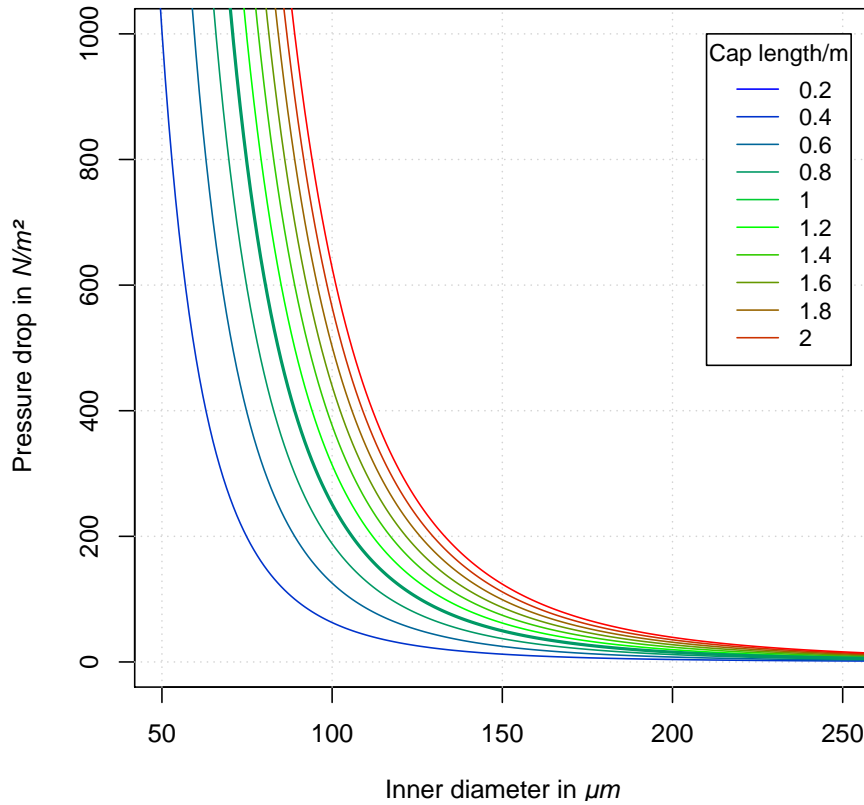
$$R = R_1 + R_2 \tag{4}$$

Figure 7: Pressure drop of capillaries with different lengths and diameters at carrier oil flow of 100 nl/s and a dynamic viscosity of 0.77 cSt. Bold green plotted line depicts the possible minimum transfer distance from microscope to positioning system (0.8 m).

so that

$$\Delta p = (R_1 + R_2)\, Q \tag{5}$$

and will help to estimate the pressure drop in following transition prototypes.

3.2.2 Transition from tubing to capillary

Initially, borosilicate and fused silica capillaries with an outer/inner diameter of 250/50 μm (Hilgenberg GmbH) were tested. This allowed for a simple insertion into standard 1/16" PTFE tubing that matches the capillary's inner diameter of 250 μm. A short length of 50 mm was chosen to have the capillary mounted at the end of the long 800 mm transition line and right before sensing. The sharp transition resulted in an accumulation of droplets, *i.e.* stopping of droplet flow and therefore losing temporal and spatial information that is required in a final screening approach (Figure 8 on the next page).
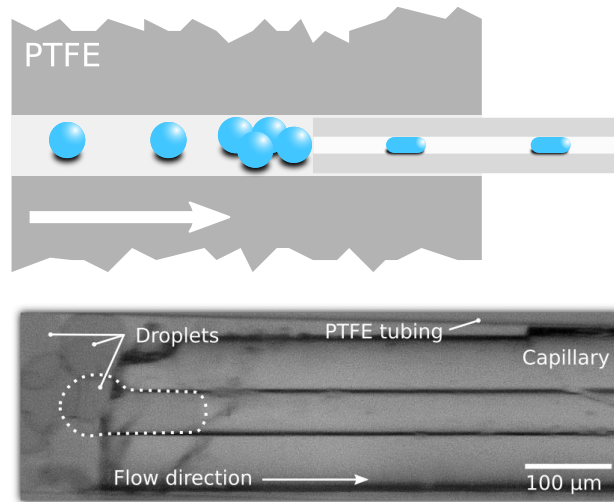
Figure 8: Droplet-capillary transition. Left: Schematic of droplet flow from PTFE-tubing to glass capillary. Right: Microscopic image of a transition area with accumulated droplets entering the capillary with 50 µm inner diameter.

A straightforward solution to this problem was to modify the orthogonal cut capillary ending to a funnel-shaped one (Figure 9). While attempts with conical drill bit machining were unfeasible, an alternative approach with a controlled etching process by hydrofluoric acid (HF) was not carried out. This requires special safety equipment and facilities as well as fully qualified personnel due to the extremely harmful nature of HF and additionally would have had introduced another level of complexity. The crucial transition area was then substituted by a real funnel at micrometer scale (Figure 10 on the next page) that bypasses the problem of modifying brittle glass capillaries. Prototypes of those micrometer-sized, precision-turned workpieces were manufactured by Mikro-Präzision Wilfried Nippel GmbH (Germany) out of a polymer. While manufacturing was possible at high precision, handling was unfeasible.
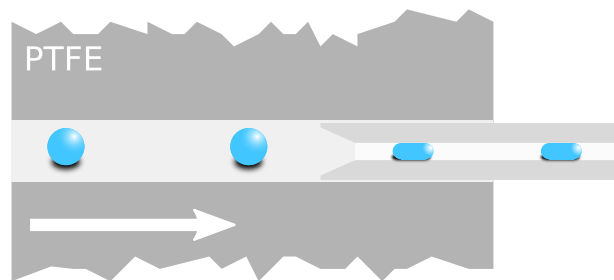

Figure 9: Design of modifying a capillary end section, either mechanically or via chemical treatment, to obtain a smooth droplet transition area.

A fourth approach was to expand the inner tubing diameter to the outer diameter of a capillary, making both inner diameters fit to
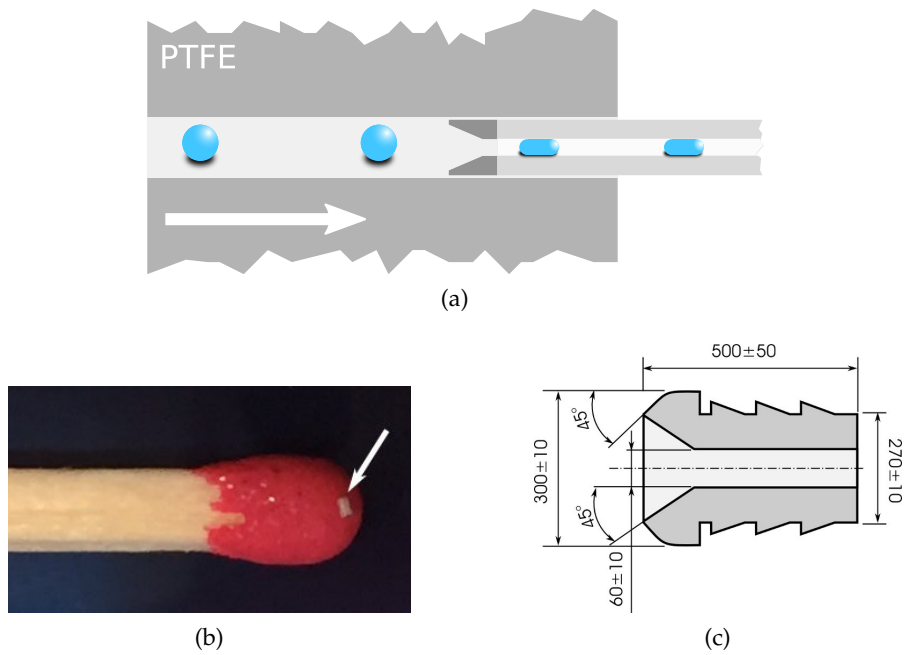
(a)

(b)

(c)

Figure 10: Micro-funnels from Mikro-Präzision Wilfried Nippel GmbH (Germany) to be inserted into a microfluidic tubing. (a) shows the intended smooth transition model, (b) manufactured micro-funnels in comparison to a match and (c) the 2D sketch, respectively.

each other. By a subsequent laser-controlled capillary tapering, the diameter would be diminished to a level that meets the required geometric specifications. This would additionally decrease the capillary's wall thickness, hence minimising optical aberrations at sensing site but may probably introduce brittleness to the system.

TAPERING   . . . approaches were performed in cooperation with Andreas Houben (Leibniz-Institut für Pflanzengenetik und Kulturpflanzenforschung (IPK Gatersleben)). Borosilicate capillaries (1 mm inner/300 µm outer diameter) were fixed in a device having a counter-directional pulling mechanism and a platinum wire as a central heating unit (Figure 11a on the following page). The moment the material's melting point was reached, the mechanism's pulling forces automatically elongated the mounted capillary resulting in a reduced diameter (Figure 11b on the next page). Evaluation of the tapered capillary by droplet injection showed an intended smooth transition, yet introduced a predetermined breaking point making a capillary handling extremely difficult. An alternative tapering approach was therefore considered.

In cooperation with Dr. Steffen Böhme (Fraunhofer IOF Jena) a capillary was tapered from 1000/250 µm (Art. Nr. 1470472, Hilgenberg GmbH, Germany) to 250/50 µm over a length of 50 mm (Figure 12a on page 28). In comparison to the tapered capillary at IPK

(a)   (b)

(c)

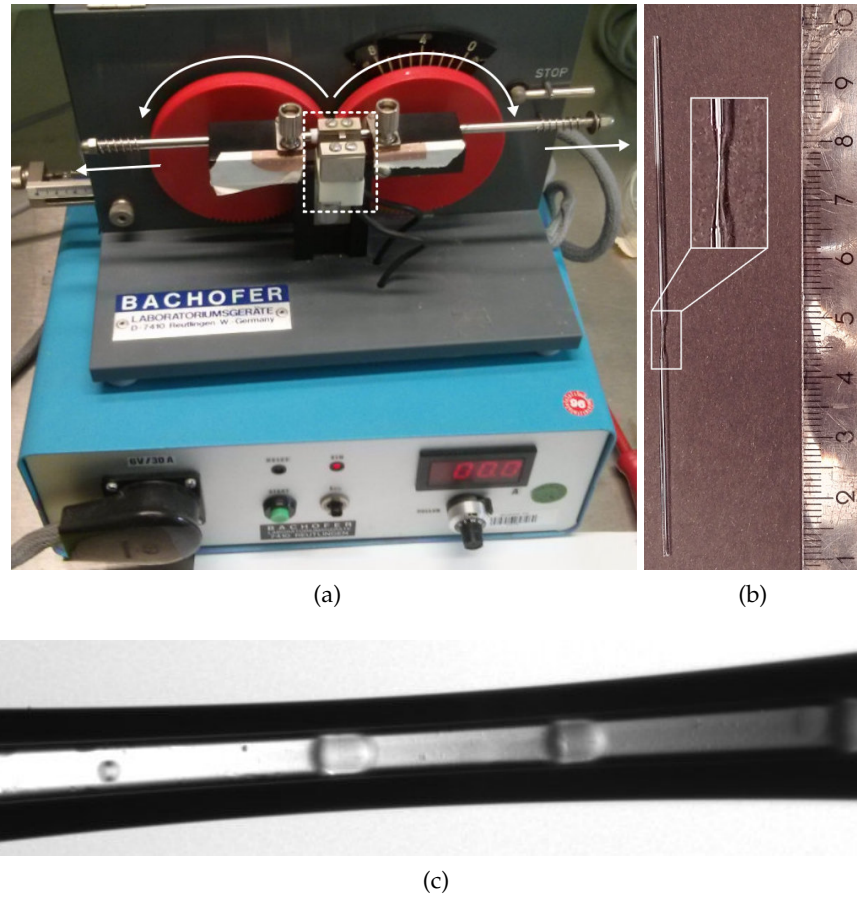Figure 11: Approach to modify a capillary for droplet transition and detection at IPK Gatersleben. (a) shows a pulling device (Bachofer GmbH) utilised to locally constrict a fixed capillary via a counter-directional pulling mechanism (white arrows) and a controlled heating unit (dashed rectangle). (b) depicts a tapered glass capillary, and (c) shows a microscopic image of droplets flowing through a locally constricted capillary.

Gatersleben this approach showed significant better diameter downsizing and stability properties. To connect this modified capillary with standard tubing an one millimetre hole was manufactured via a precise drilling machine to one inlet of a PTFE tubing (Figure 12b). Successive microscopic observation revealed a 300 μm gap at transition site plus further gaps between inner PTFE diameter and outer capillary diameter (Figure 12c). Though this micrometre distance seemed negligible, a vast amount of droplets were lost, *i.e.* stopped moving due to this compartment free of flow. Such an interfacial behaviour would be fatal in a final droplet dispensing setup, where every single droplet is a crucial hit. Further optimisation was limited by mechanical crafting abilities. Minimising the gap by applying adhesives clogged the channel due to strong capillary forces at the respective regions. This plug-in technique could not be assembled free of leakage.

THE MICROTIGHT$^{®}$ ADAPTOR   ... is an interface by IDEX to facilitate tubing capillary connections at "zero dead volume". A first droplet transfer was realised with standard PTFE-tubing (1/16" outer/250 μm inner) and a fused-silica capillary (360/100 μm), typically used in High-Pressure Liquid Chromatography (HPLC) applications. Reproducible spaced droplets were injected into a PTFE-tubing via counting threshold-based droplet sorting every hundred events (Listing 2 on page 97) generating an inter-droplet distance of ≈1.5 s.

As the transition inside the adaptor can not be observed due to its opaque material (PEEK, Polyether ether ketone), droplets were observed before entering and after exiting the interface. Figure 13 on page 29 shows successful transported droplets inside a capillary after the critical adaptor transition. Yet, droplet grouping occurred with significantly minimised inter-droplet distance at the millisecond scale and additional recurring air droplets. It is assumed that due to a pressure build-up at the interconnection, a periodic stop-flow and relaxation event took place. This explains the generation of air droplets—which did not appear before the transition—and also the grouping of droplets. However, also droplet behaviour inside the afferent polymer tubing plays an important role in the observed results and will be further discussed in the next section.

3.2.3 Tubing transfer studies

Investigations on droplet flow inside a tubing were performed with standard PTFE tubing (1/16"/250 μm) and no subsequent capillary transition. Droplets were again homogeneously spaced on-chip and sent to the connected tubing (Figure 14 on page 31). Depending on the tubing's spatial orientation, different scenarios were observed: While droplets exited the chip upwards (at vertical tubing alignment), the inter-droplet distance started diminishing compared to spacing seen
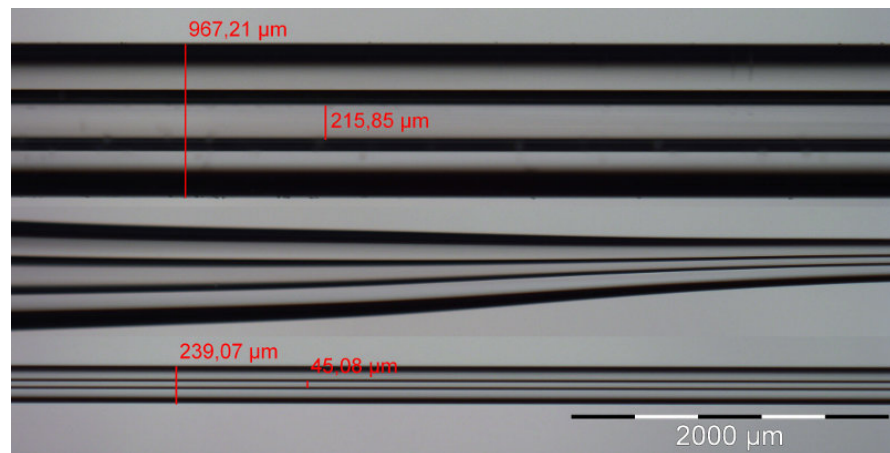
(a) Capillary tapering approach from d_o/d_i = 1000/250 µm down to 250/50 µm. Images by courtesy of Dr. Steffen Böhme (IOF Jena).
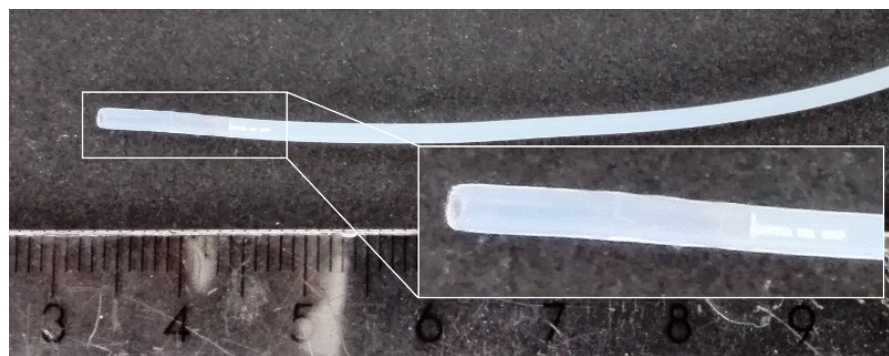
(b) PTFE tubing with drilled one millimetre hole to insert a capillary of equal outer diameter.
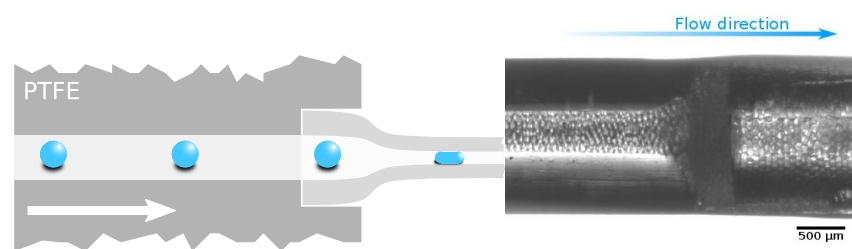
(c) Left: Schematic for smooth polymer-capillary-transition. Right: Microscopic image of a glass capillary inserted into a PTFE tubing with droplets entering the capillary.

Figure 12: Laser-controlled capillary tapering approach

Figure 13: Testing of the PTFE-capillary transition using the MicroTight® adaptor (top). Periodically inserted droplets were injected into a PTFE-tubing flowing through the adaptor transition into a capillary. Bottom: Images of periodically occurring grouped liquid droplets and an air droplet.

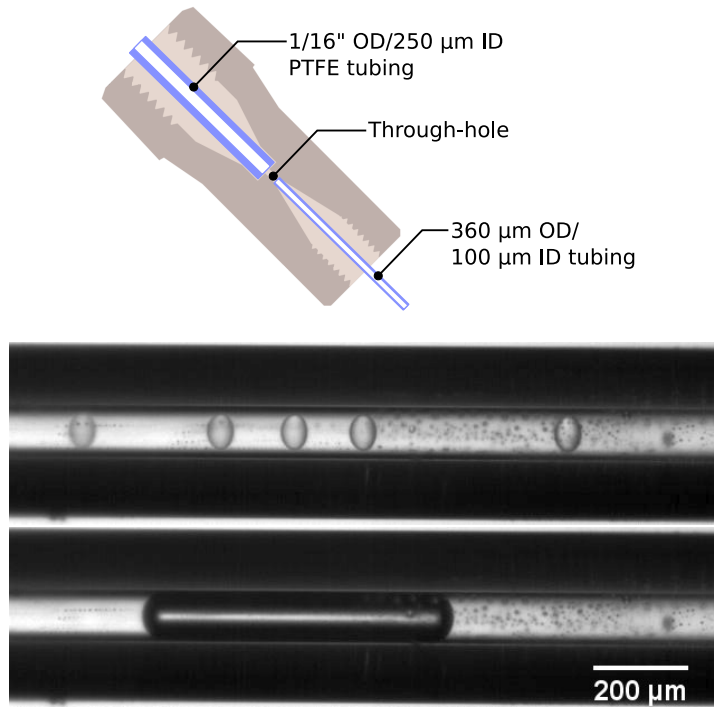on chip. Nevertheless, droplets kept their sequential position (Figure 14a). At horizontal tubing orientation, droplets started contacting each other, aggregating close to the inner wall (Figure 14b). At vertical tubing alignment (downward droplet flow) the previous droplet sequence could barely be observed (Figure 14c). Spatial and temporal information loss occurred the longer the droplets were pushed downwards in the transfer tubing (Figure 14d). Two reasons are causing this phenomenon: As $d_{i,tubing} \gg d_{drop}$, carrier fluid bypasses droplets and transfers only partial amounts of its kinetic energy to a droplet. In addition, due to $\rho_{drop} > \rho_{oil}$, droplet buoyancy acts against the predominant flow direction and further decreases the velocity. Therefore, droplets were again injected into tubing with a decreased inner diameter of 100 µm (PM-1148-F, material: FEP). The resulting inter-droplet distance diminished insignificantly; droplets kept their temporal and spatial information over a long distance (Figure 14e on page 31). Droplet grouping, as seen in the previous section, was therefore not only affected by the MicroTight® adaptor transition, but also due to the afferent tubing's inner diameter/injected droplet diameter. Based on those results, the ideal and most simple solution for a CWI is a single polymer tubing from chip to sensor, as it can easily be mounted to a glass-chip and does not include any critical

transitional stage. But compared to glass, FEP-based tubing with significant higher light-transmission properties than PTFE shows material asperities due to an extrusion-based polymer manufacturing process. This causes unreproducible, optical droplet sensing behaviour. Alternative high-tech fluoropolymers such as H-PFA were additionally tested and showed similar results. Aberrations can be decreased by imitating a glass-capillary, *i. e.* lowering the tubing's wall thickness, but do result in a drastically reduced tubing stiffness and introduce massive problems regarding the final droplet dispensing mode (Section 3.4.5 on page 56).

A FINAL SOLUTION   ... to transfer picolitre droplets was found by utilising a flexible glass capillary (Model TSH100375, 360/100 µm, Molex) concurrent to the PDMS-based microfluidic chip development (see previous Section 3.1). This fused-silica capillary is coated with a 10–20 µm thin fluorinated acrylate coating (TSH) that enables high flexibility without changing optical properties. With this, it was possible to establish a direct chip-capillary connection using an appropriate biopsy puncher, so that after the bonding process tubing can be inserted into the punched holes. Due to TSH's maximum applicable temperature of 125 °C standard hydrophobisation protocols could be applied. An easy mounting to the droplet detection unit (Figure 24 on page 45) was also realised by using the afore examined MicroTight® adaptor as repurposed fixation tool. Since basic CWI parameters are now identified, the systems pressure drop can now be estimated to 250 Pa, a 2.5 fold increase compared to standard PTFE tubing with an inner diameter of 250 µm.

This final approach reduced one critical droplet transition. Still, a transfer from chip to capillary takes part and needs to be studied in detail, since this is a crucial step towards the first working CWI prototype.

3.2.4   Transition from chip to capillary

The goal was to examine the transfer of sorted droplets from chip into the capillary. Ideally, droplets should enter the capillary without interruption, *i. e.* not losing their spatial information and inter-droplet distance (Figure 15 on page 32, top). To validate that no droplet loss occurred at the chip-capillary-transition, droplets needed to be sorted while being observed when exiting the chip. Due to optical setup restrictions, a droplet sorting was simulated by reinjecting droplets into the sorting chip with the electrodes continuously on, thus sorting all droplets. Thereby, every droplet was redirected into the positive channel heading to the capillary. As PDMS-chip outlets were designed for the insertion of standard-sized 1/16" tubings, the applied capillary's diameter of 360 µm was out of the ordinary. Yet, redesigning and manufacturing a new chip was not performed. Instead, the chip
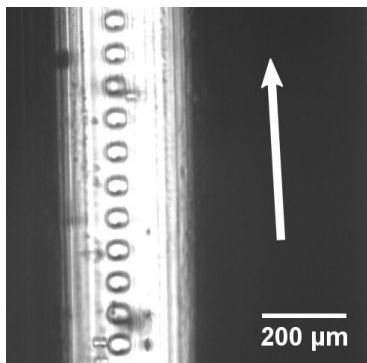
(a) Tubing orientation upwards, inter-droplet distance of spaced droplets low but sequential information ensured.
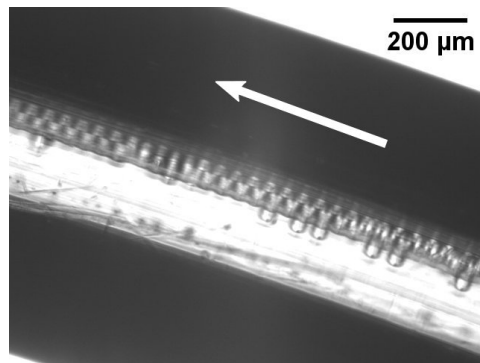
(b) Tubing alignment horizontal, inter-droplet distance lost, spatial information can still be acquired.
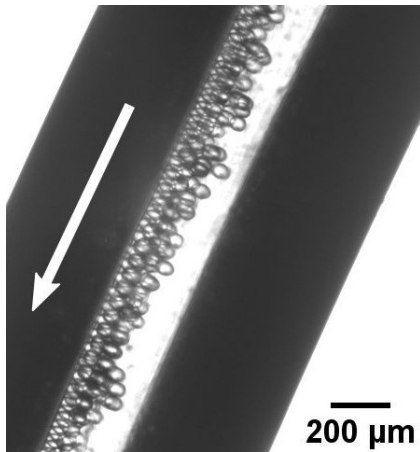
(c) Tubing orientation almost vertical, droplets start reorganising positions, temporal and spatial information terminates.
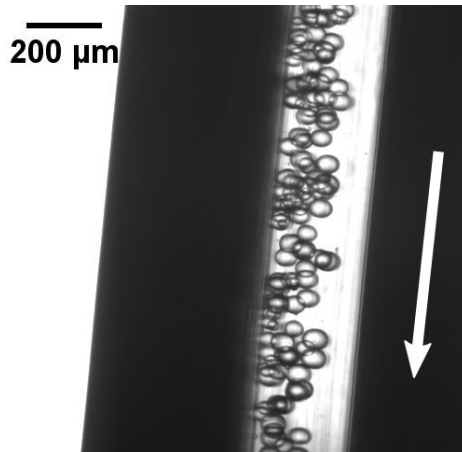
(d) Tubing orientation vertical, chaotic mixing of droplets.
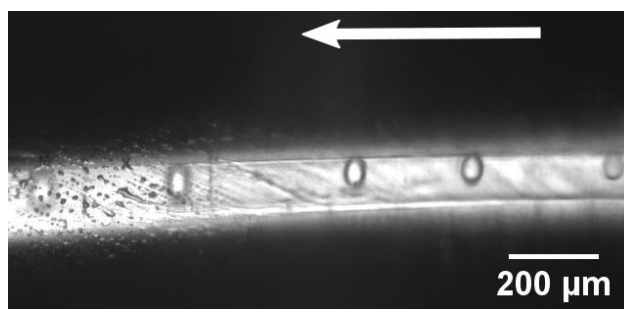
(e) Interspacing studies in a tubing with 100 µm inner diameter.

Figure 14: Studies of droplet flow using on-chip spacing and subsequent tubing injection. Images (a)–(d) show droplet flow inside a different aligned tubing (d_i = 250 µm).

outlet was made using a 350 µm puncher to generate a direct channel-to-capillary interface.
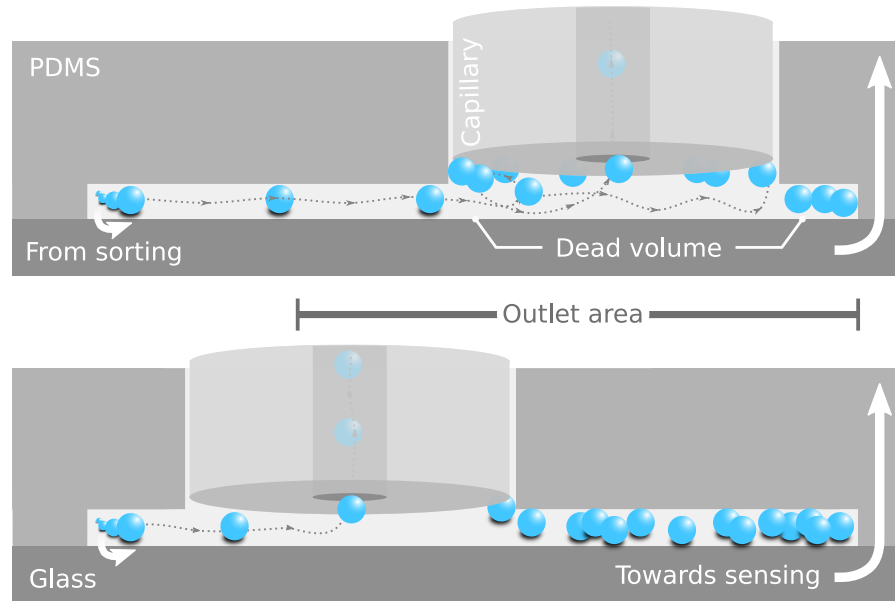
Figure 15: Schematic of ideal (top) and real (bottom) droplet transition from chip to capillary.

Observations showed that depending on the punched location, droplets primarily moved towards the capillary but were also observed in zones of dead volume. In general, droplets that are actuated by carrier oil move on corresponding stream lines towards pressure-preferred channels. Considering a certain amount of kinetic energy of the carrier fluid, a trajectory to alternative locations can occur; in this case areas of dead volume. Hence, the punching location was changed to be as close as possible to the channel exit before expanding to the outlet area. Results showed that at typical sorting pressure regimes all droplets exited the chip without interference, *i. e.* no circulation or parking routes around the capillary entrance site (Figure 16 on the facing page). Too high flow rates—*e. g.* when setting up sorting—led to droplets that overcame the predominant flow towards the capillary into dead volume zones. These droplets could be defined as lost samples, but are considered as negligible as their purpose was to set up sorting. Moreover, no backward-movement towards the capillary was observed as a result of a positive feedback loop: As more droplets enter the outlet area, their volume automatically contribute to a decreased dead volume. In the end, this optimises the droplet flow towards the capillary.

At this point, all occurring droplet transitions were established, evaluated and optimised (see Table 3 on page 34 for full comparison). The last crucial transfer step from capillary to an unloading point (*e. g.* a Petri dish surface) needed to be analysed in detail. In order to un-
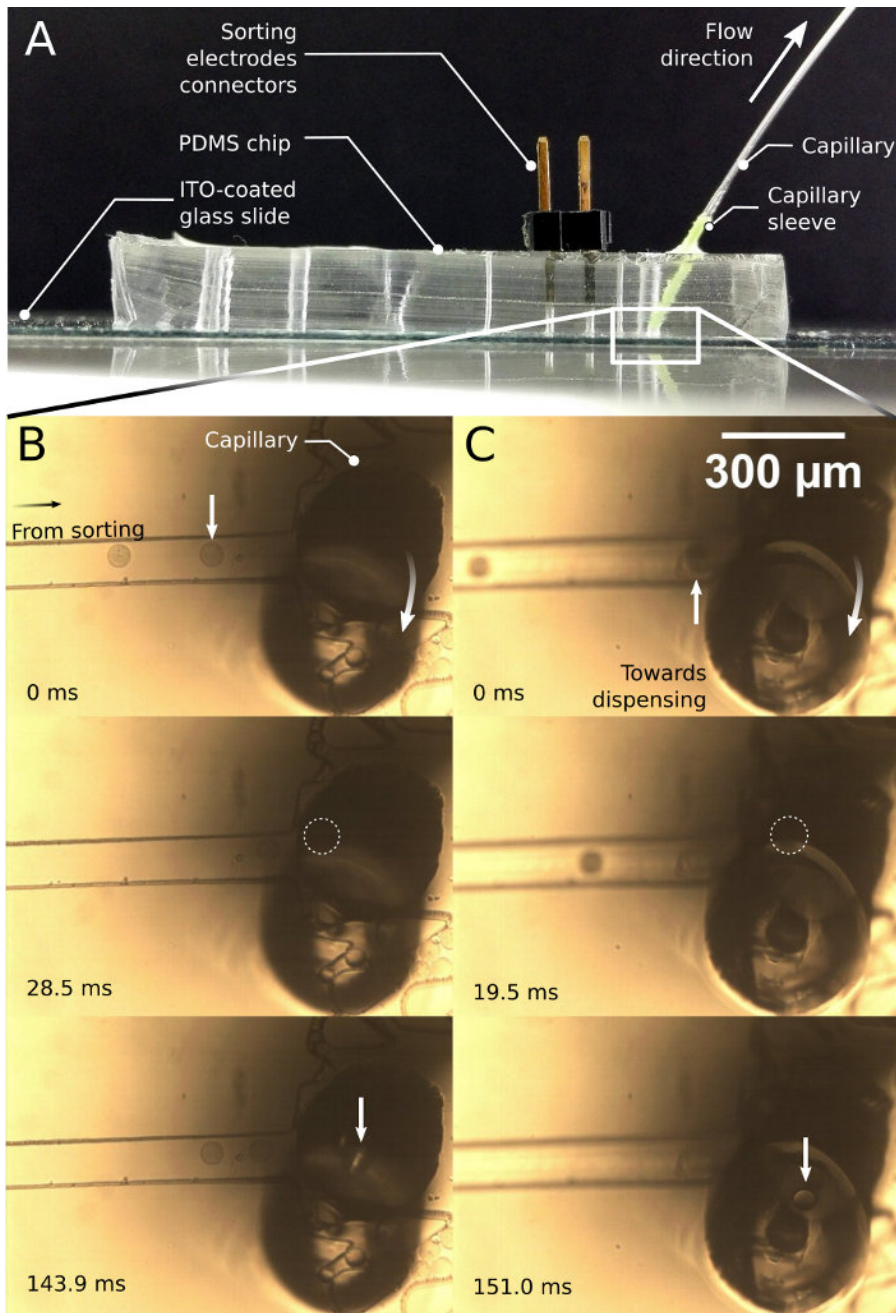
Figure 16: Microfluidic chip-to-capillary interface for single droplet transition. A) PDMS sorting chip on an ITO-coated glass slide with electrode connector pins and mounted capillary. B) and C) Detailed view of chip-capillary transition inside the PDMS chip at different focal distances showing droplets (marked with arrow) moving out of the chip into the capillary.

derstand that transfer, it is necessary to give an introduction on the so-called droplet delay time at the positioning site.

Table 3: Summary of developed and evaluated CWI approaches.

TYPE	TRANSITION	PROS/CONS
PTFE $\rightarrow$ capillary[1]	Abrupt	✓ No tube modifications or special equipment needed ✗ High backpressure, breaking droplets
PTFE $\rightarrow$ capillary[1]	Smooth via etching[4]	✗ Controlled HF etching of glass capillary end too complex/dangerous
PTFE $\xrightarrow{\text{funnel}}$ capillary[1]	Smooth via microfunnel[4]	✓ Microfunnel manufacturing possible ✗ Mounting impossible
PTFE $\rightarrow$ capillary[1]	Smooth via tapering and diameter adjustment	✓ Can be done manually or laser-controlled ✗ Lowers capillary wall thickness, introducing brittleness ✗ Mounting impossible
PTFE $\xrightarrow[\text{adaptor}]{\text{MicroTight}^{®}}$ cap[1]	Gradual diameter decrease via adaptor interface	✓ No tube modifications necessary ✓ Stable and robust mounting ✗ Pressure build-up interferes fluidic sensing ✗ Breaking capillary
PTFE $\xrightarrow[\text{adaptor}]{\text{MicroTight}^{®}}$ pcap[2]	Gradual diameter decrease via adaptor interface	✓ No tube modifications necessary ✓ MicroTight® adaptor for sensor mount ✗ Insufficient light transmission/aberrations
Cap[1] /w pol. coating[3]	No transition	✓ No tube modifications necessary, no pressure build-up ✓ MicroTight® adaptor for sensor mount ✓ PDMS-chip mount possible

[1] "Cap/Capillary" denotes a glass capillary made of either borosilicate or fused silica.

[2] "pcap" defines a capillary made of highly transmissive H-PFA or FEP polymers.

[3] "pol. coating" relates to fluorinated acrylate polymer coating (TSH, Molex) to make glass capillaries translucent and flexible.

[4] Transition stages were hypothesized, as manufacturing or mounting could not be realised.

DROPLET DELAY TIME CALCULATION   A droplet that flows inside the CWI capillary will pass the sensing area and generate a corresponding signal. The sensor is situated a certain distance s above the capillary outlet (Figure 17, A), usually 35 mm. To estimate the time a droplet takes to exit the capillary (delay time t_d), sensed droplets had to be analysed regarding their velocity inside the capillary (v_{cap}) under given flow conditions. Using triggered high-speed micrographs (Figure 17, C) droplets were observed near the capillary exit. From these images, v_{cap} was estimated from a distance s_d by a reference size[2] (here: 900 µm), and the duration t_{cap}, 115 ms in this case. Assuming a constant droplet velocity throughout the capillary, t_d was calculated to Equation (6):

$$t_d = \frac{s}{v_{cap}} = s\frac{t_{cap}}{s_d} = 4.46\,s \qquad (6)$$
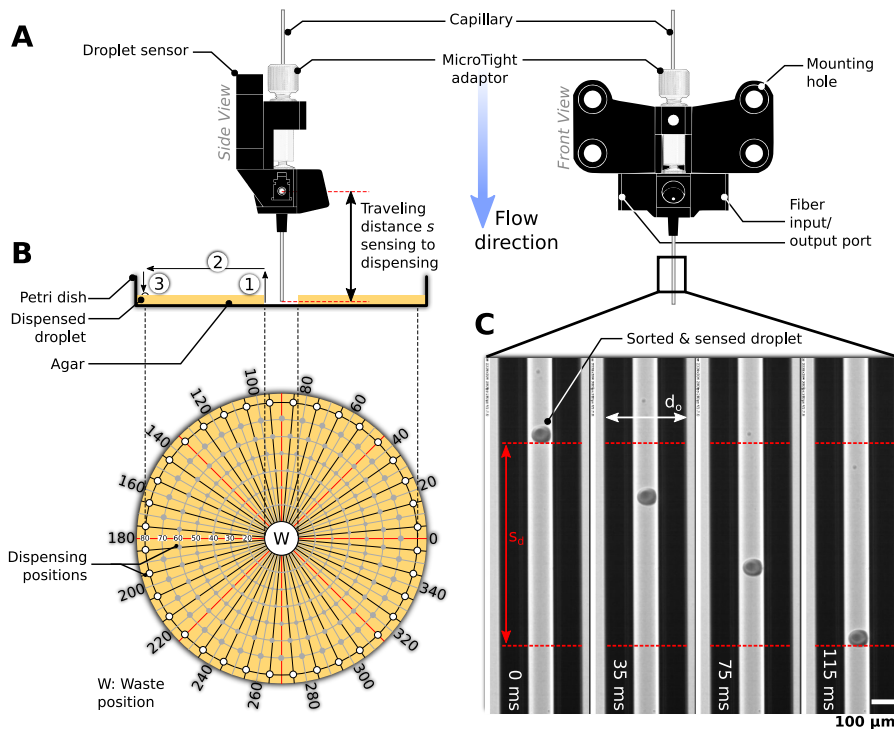
Figure 17: Single droplet sensing, positioning and dispensing. A) Schematic representation of the final refraction-based sensor prototype to detect single, unlabelled picolitre droplets inside a capillary. B) Petri dish filled with agar medium and a central punched waste compartment. Possible positions for single droplet dispensing are coloured grey, where white dots depict the farthest position. Numbers 1–3 illustrate a positioning route (see Figure 34 on page 58). C) Tracking of a sorted and sensed picolitre droplet inside a capillary.

---

2 The outer diameter of the capillary $d_o = 360$ µm was used as a reference, calculated via FIJI [79]

However, it is not possible to have this observation setup during actual positioning into a microtiter plate or a Petri dish. Alternatively, v_{cap} can be estimated after measuring the droplet speed inside the positive channel of a sorting chip v_{chip}. This assumption is based on a constant volumetric flow rate Q and uses the cross-sectional area of both the rectangular microchannel A_{chip} ($\pi \cdot (50 \, \mu m)^2$) and the capillary A_{cap} ($50 \, \mu m \cdot 80 \, \mu m$), respectively.

$$v_{cap} = \frac{Q}{A_{cap}} = \frac{v_{chip} \cdot A_{chip}}{A_{cap}} \tag{7}$$

The obtained speeds using this method correlate with observations at the capillary exit, with an observed velocity v_{chip} = 24.14 mm/s and v_{cap} = 12.23 mm/s, which confirms the assumptions for an estimated time delay. Though, it should be noted that the assumption of constant speed may only partially apply to flowing droplets, since their velocity is subject to other aspects such as size/contact surface, drag and buoyancy.

3.2.5   Transition from capillary to Petri dish

Monitoring the droplet transition between capillary exit and the surface of agar medium in a Petri dish was performed to understand the droplet trajectory and integrity during transition as well as to interpret results of dispensing experiment. Such a transition was examined by emulating a position and contact-based dispensing process. This was achieved by simplifying a positioning to a single z-stroke onto a fully transparent agar medium substitute (PDMS, 1:20) enabling a standard camera transmission record. The trigger signal of a sensed droplet was used to start the record as well as its positioning (Figure 18 on the facing page, t = 0.00 s). Based on the current droplet velocity of ≈11 mm/s, a delay time of 5 s was set. The projected online droplet processing results in a constant carrier fluid flow (here: 90 nl/s) and generates a hanging drop that grows in volume (max. 60 nl) during positioning time t_p (Section 3.4.5 on page 57). The excessive fluid slowly wets the outer coating area of the capillary but flows off immediately when reaching the agar medium surface. With the default location of the capillary less than one millimetre above the waste bottom, a direct contact of outflowing oil to the surface is guaranteed. After a trigger occurs, the capillary moves to a certain position and loses contact during the required positioning time. A transitory droplet then passes the exit at >4.34 s and flows onto the PDMS surface (t = 4.59 s).
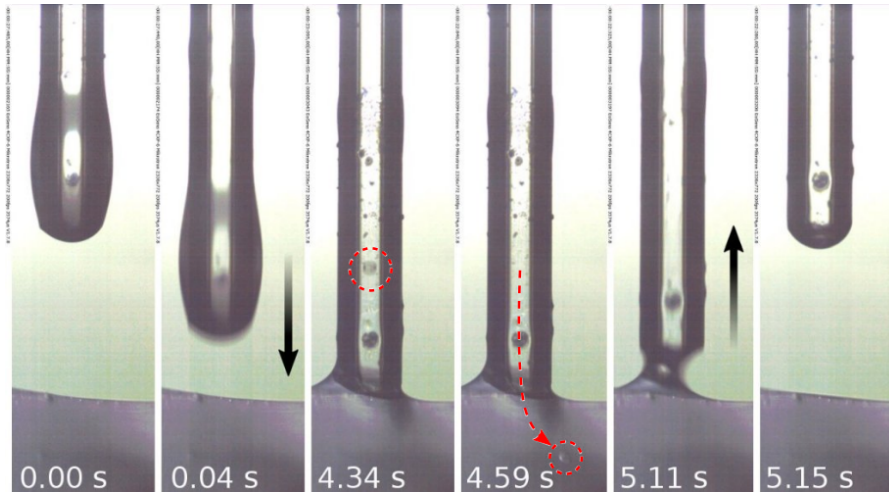
Figure 18: Droplet transition study from capillary to a transparent PDMS-surface that emulates an agar medium surface in a Petri dish. Dark circular shaped spots are located on the outside of the capillary and do not influence the droplet flow and displacement process.

3.3 DROPLET DETECTION UNIT

The moment a droplet of interest is being deflected in a microfluidic chip sorting structure, it starts a long journey inside a tubing that finally leads to a suitable compartment like a MTP or a Petri dish. Assuming the fluidic system is running at fixed flow rates without any change in velocity and no friction, the time a single droplet exits the system could be approximated. But in reality, a microfluidic system will not always operate in a fully controlled manner. There will be changes in carrier fluid or aqueous phase flow due to perturbations which the system is trying to self-equilibrate. In some cases, small particles that passed upstream filter units accumulate inside a chip or on tubing walls and can clog the channel structures, therefore constricting a proper flow of liquids. Also wetting issues due to either incomplete chemical surface treatment or biofilm formation over time might change the behaviour of the whole fluidic system. Changes of atmospheric pressure or temperature of the liquid itself might also result in a changed viscosity hence changing characteristics of the flow. All those factors ultimately lead to a unforeseeable time a droplet exits the system. This makes a sensor unit, installed a certain distance upstream of the system's exit (Figure 17) an essential component. Multiple requirements had to be taken into account:

The 'long' journey of a droplet ($d = 70\,\mu m$) travelling 800 mm is comparable with a human-being walking a route of 20 km!

1. The first and most important premise was that the sensor unit should be able to detect a droplet without influencing it, *i. e.* not changing its track, modifying the (biological) content or even breaking it.

2. It should detect droplets in a reproducible manner. Based on the signal characteristics the experimenter should be able to differentiate between droplets, fragments of former droplets (satellites) and clusters of droplets.

3. The sensor should not be affected by any proximate elements, *e. g.* when the experimenter is moving next to it or any surrounding optical source is to be switched.

4. The last crucial point was the requirement of simplicity and robustness, yet, the sensor should still be sensitive enough to detect picolitre droplets.

In general, a manifold of sensing principles exist. Droplets can be detected electrically via impedance [80], optically via absorbance [81], refraction [82], fluorescence [67], Raman spectroscopy [83] or by digital imaging processing [60, 84].

3.3.1 Optical sensor simulation

Preliminary optical simulations of a light barrier-based sensor were conducted via TracePro® raytracing software (Lambda Research). This approach was necessary to answer the questions if a) the sensor is able to detect droplets at the picolitre scale and if true, b) how the signal is shaped, c) which physical principle it follows, d) if conclusions on the size can be made and d) if it can be easily used for a subsequent automation approach. Simulations are based on *Snell's law* which describes the relationship between incident and refracting angle of light beams/waves when passing the interface of different materials (Equation (8))

$$\frac{\sin \theta_1}{\sin \theta_2} = \frac{\lambda_1}{\lambda_2} = \frac{n_2}{n_1} \tag{8}$$

where $\sin \theta_1$ and $\sin \theta_2$ are angles of incidence and refraction, λ_1 and λ_2 the wavelength in the respective media and n_1 and n_2 the respective refractive indices.

A droplet with a fixed diameter of 60 µm was simulated to move in one micrometre iterations inside a capillary through a light beam (see Section 2.5.1 on page 10). The developed code for this simulation can be seen in Listing 3 on page 97. Results indicate that a transiting droplet changes the way of incident rays due to different phase layers and refractive indices. It shows characteristic shoulders left and right of a peak at position ± 20 µm due to the droplets sphere curvature when entering and exiting the light barrier. At position zero the droplet is acting like a lens that bundles light. This results in a characteristic peak (Figure 19 on the next page) and can be used for automation purposes.

To characterise the sensor regarding sensitivity and the influence of the capillary's position, moving sphere-shaped droplets of different
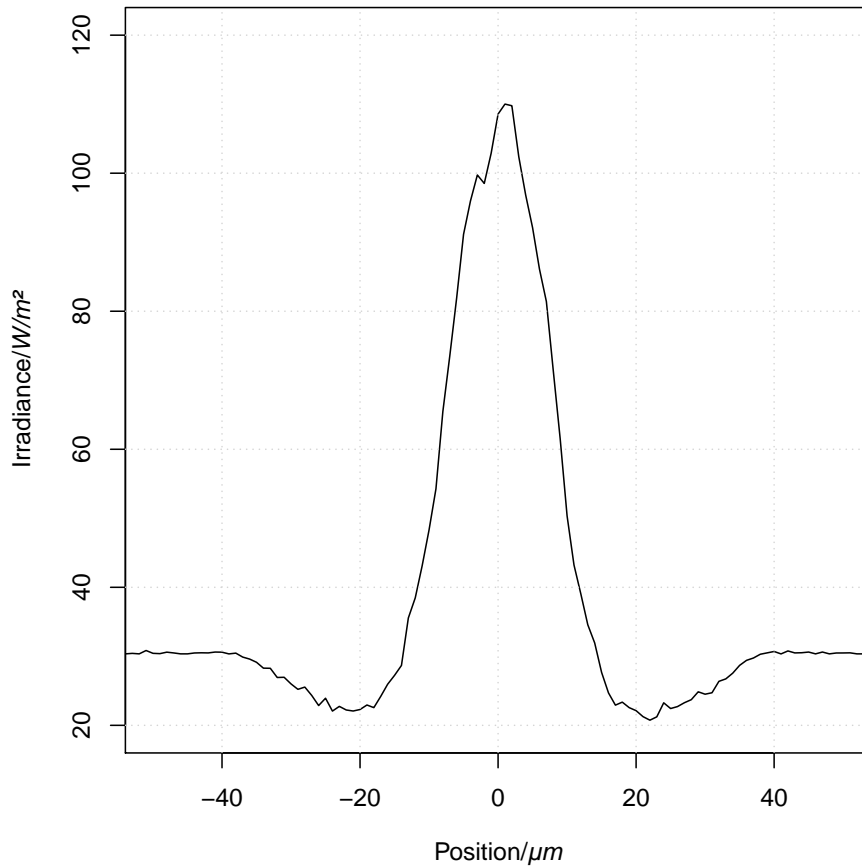
Figure 19: Simulated refraction-based droplet signal generation when passing a light beam inside a hollow glass capillary. The droplet diameter is 60 μm.

diameters were simulated inside the capillary that was also moved perpendicular through the light beam (Listing 3 and Figure 20 on the following page).

While the background level below 40 W/m² is a result of the circular shaped capillary itself, values below or above originate due to a droplet transition (3D-plot, A). Interestingly, peak intensities correlate only partially to the droplet size as shown by extracted data of integrated and averaged intensities at position zero ± 5 μm (Figure 20 on the next page, B). The observed profile is due to the focusing effect caused by the passing droplet. At a radius of $\approx$30 μm, the droplet generates a maximum peak intensity, whereas the limit of detection (LOD) is reached at a radius of $\approx$15 μm. So, depending on the droplet size and therefore its curvature different focal points and thereby different intensities are detected.
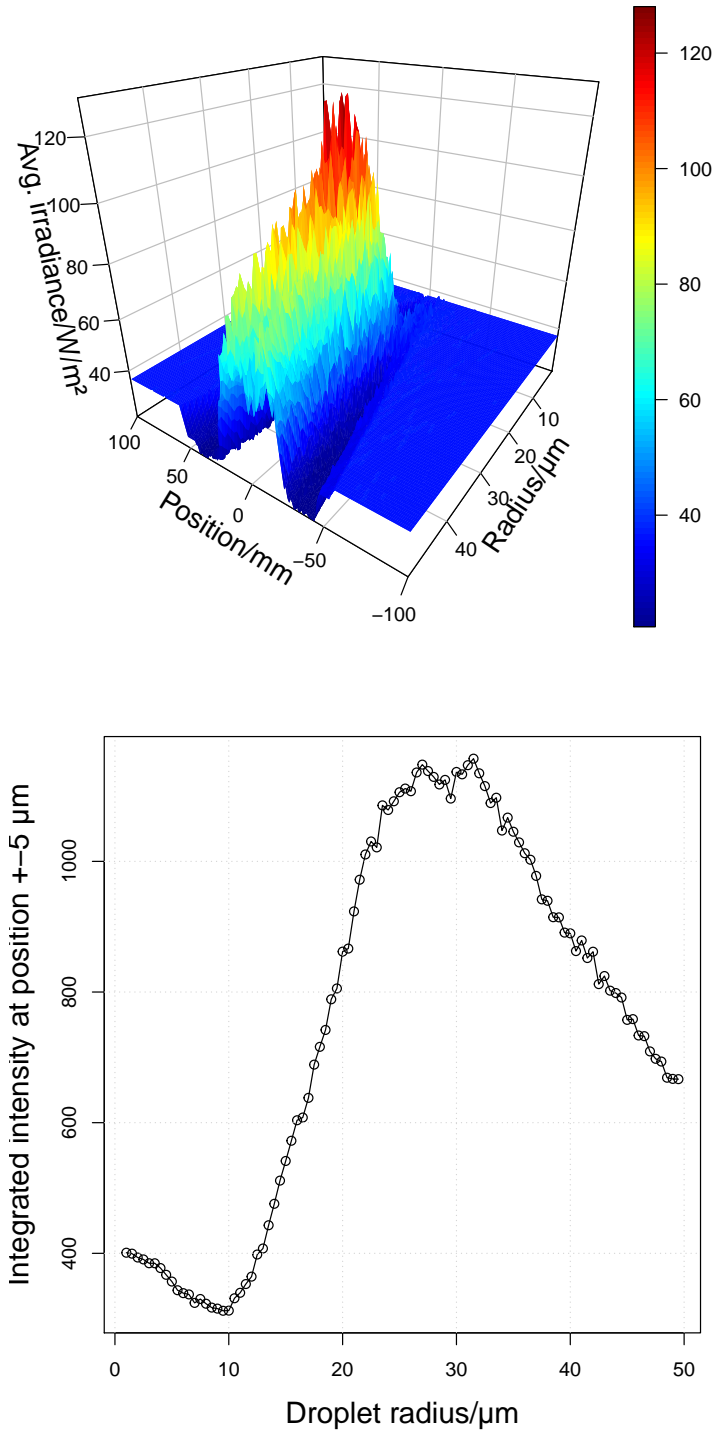
Figure 20: Raytracing simulation showing resulting signals of droplets with varying diameter flowing through a perpendicular moving capillary in which a 650 nm light beam passes at position zero. A) Three-dimensional plot of resulting droplet signals before and after the light beam and radii between 1 and 50 μm. B) Dependency of droplet size plotted against their integrated average peak intensity at position zero ±5 μm.

3.3.2 Initial sensing platform

In a first practical approach, based on publications of Butler *et al.* [85] and Trivedi *et al.* [86], a commercially available laser pointer (Fiber-point ET®, IMM Photonics GmbH, Germany) was coupled to an optical multi mode fibre (50 µm inner core) with a SC-plug (LANCON-NECT GmbH, Germany) via a universal 2.5 mm ferrule. On the fibre's opposite side the LC-plug, coating and cladding was removed, so that the outer 125 µm core could be mounted on a metal plate carrying a V-groove (Thorlabs HFV001). The procedure was repeated for a second light collecting single mode fibre (9 µm core, see Figure 21), which was connected to a photodetector (circuitry see Section 2.7.1 on page 13) via a SC to SM1 adaptor (S120-SC, Thorlabs). Generated signals were then redirected to a DAQ card for signal monitoring and acquisition. In-between the concentric mounted core fibres a hole needed to be drilled to perpendicularly mount the droplet carrying glass capillary (250/50 µm, Hilgenberg GmbH, Germany) that was fixed inside a PTFE-tubing. The borehole-alignment and therefore the capillary to the optical fibre's light barrier had to be extremely precise. In other words: The hole should at least be equal the capillary's outer diameter (250 µm!), though should not be bigger than two times the inner capillary diameter, resulting in a drill hole of 300 ± 50 µm. This could be realised at the IPHT Jena, department of Precision Engineering. A subsequent setup integration was hardly realisable due to the brittle and unstable mounting (Figure 21). Additionally, droplet breakage and clogging was observed due to an abrupt transition from PTFE-tubing to capillary as seen in first tubing-to-capillary transition studies (Figure 8 on page 24).
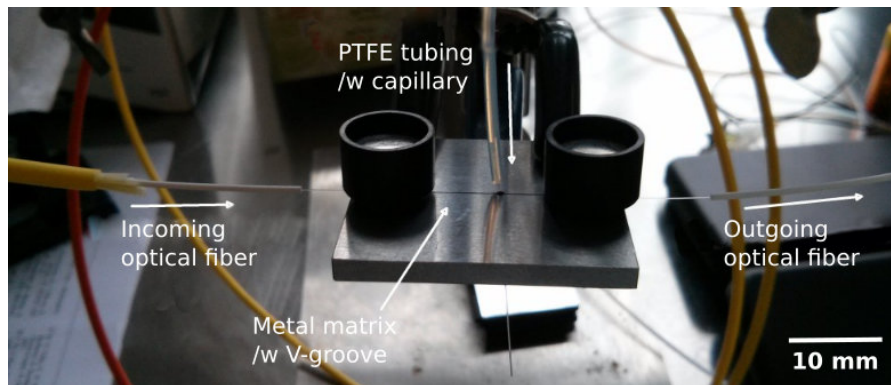
Figure 21: Initial platform for an optical picolitre droplet detection inside a capillary. Thorlabs V-Groove fibre holder with in- and outgoing 125 µm fibre cores fixed with magnetic cylinders and a perpendicular arranged glass capillary inside a PTFE-tubing carrying DOIs.

A solution regarding optical mounting issues was to position all incoming and outgoing components at micrometer precision in a

simple way. The easiest but most expensive alternative included three combined XYZ-positioning stages for a straight forward alignment.

3.3.3   Second sensor generation

A solution for the above discussed issues was the utilisation of additive manufacturing (AM) developed in the 1980s by Kodama *et al.* [87]. Better known as 3D-printing, new ways of prototype manufacturing emerged by building a model layer by layer at micrometre precision level. Hence, a second prototype made of a mechanically stable resin (Prime Gray) was designed in AutoCAD and 3D-printed at i.materialise (Belgium). It integrates an axial and concentric fibre mount similar to the Thorlabs product HFV001 used in the first approach as well as a precise perpendicular capillary mount (Figure 22 on the next page) enabling an optimised optical setup regarding mechanical stability. Albeit having an exact CAD-based design, the final product contained faulty parts such as closed fibre inlets caused by limited production capabilities like resolution of XYZ-layers, material selection and manufacturing technology (*e. g.* stereolithography, laser sintering). Due to limited machine processing an alternative advancement was performed by use of a laser cutting technique at the Günter-Köhler-Institut für Fügetechnik und Werkstoffprüfung GmbH (IFW Jena) by Jan Giesecke. While this new setup was freed from the first prototype's teething troubles, it still showed many issues: 1) imprecise capillary mount that led to unacceptable signal curve progression, 2) a still unstable and complicated axial and concentric fibre mount and 3) a fluctuating light source. For the first time, droplets of $\approx 70\,\mu m$ diameter could be detected, but reflected all the prior mentioned issues (Figure 22e).

3.3.4   Third and final sensing platform

While at this phase of development the potential use of AM was obvious, the utilisation in a final setup (*i. e.* sensor mounting on a moving axis system) still seemed unfeasible due to extreme brittle optical fibres and the glass capillary for droplet transport. To circumvent fibre breakage while maintaining concentricity, a LC shaped plug was introduced into the 3D-design enabling an easy plugging of commercially available pigtailed fibres without further modifications (Figure 23 on page 44). Additionally, a pipette receptacle for microlitre pipette tips was added for an optional contact-free dispensing based on a pressurised air flow (Section 3.4.5 on page 56). With this robust optical mount still changes in the detected baseline signal at Z-axis movement were observed. The cause was found to be in two separate reference systems. By envisioning the optical sensor mounted on a moving Z-axis as system A and a surrounding fixed system B that contains the light source and the detector, a signal change seems ob-
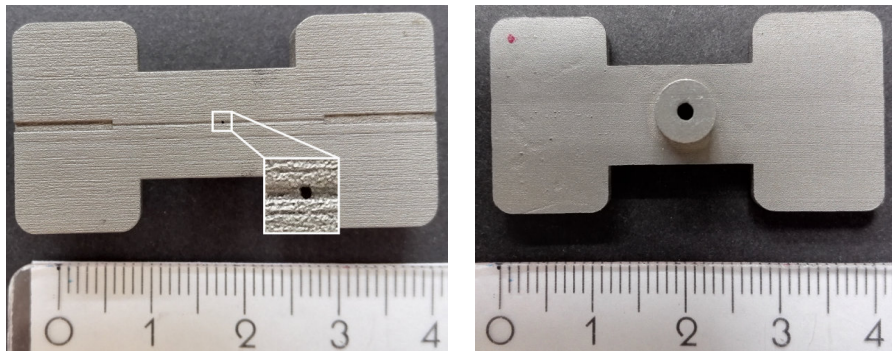
(a) Top view of first 3D-printed sensor prototype. Zoom view shows laser cut through-hole for capillary insertion. Grooves left and right are alignments for stripped optical fibres.

(b) Bottom view of sensor with a cylindrical support for stable capillary mount.
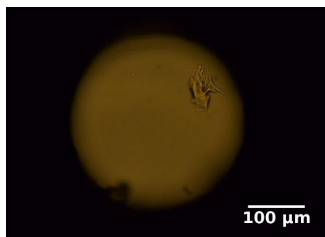
(c) Microscopic image of laser cut through-hole with a diameter of 300 μm.
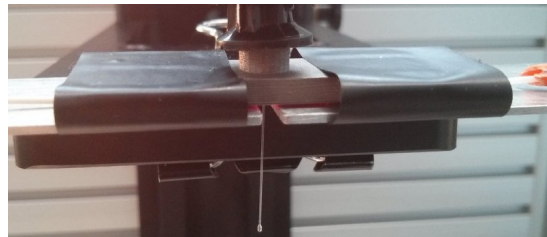
(d) Sensor with concentric fibre mount (hidden below black tape) and perpendicular capillary fixation.
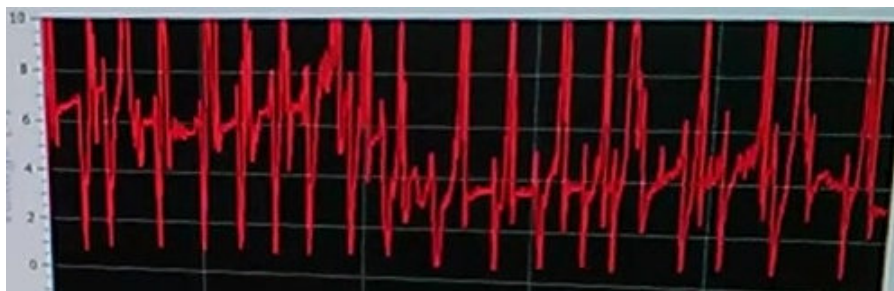
(e) First acquired droplet signals (voltage signals over time) depicting a curve progression as simulated beforehand Section 3.3.1 on page 38. Highly unstable baseline progression between 3 and 6 V and a droplet signal amplitude between 1 and 10 V indicate unstable mounting conditions and non-stabilised light source.

Figure 22: First sensor prototype made of stainless steel via laser sintering.

vious, *i.e.* any movement of system A relative to system B induced a motion of in- and outgoing fibres. A simple solution was found by bending both fibres gently 180 degrees and mounting them in opposite directions on the Z-axis to diminish motion related signal changes.
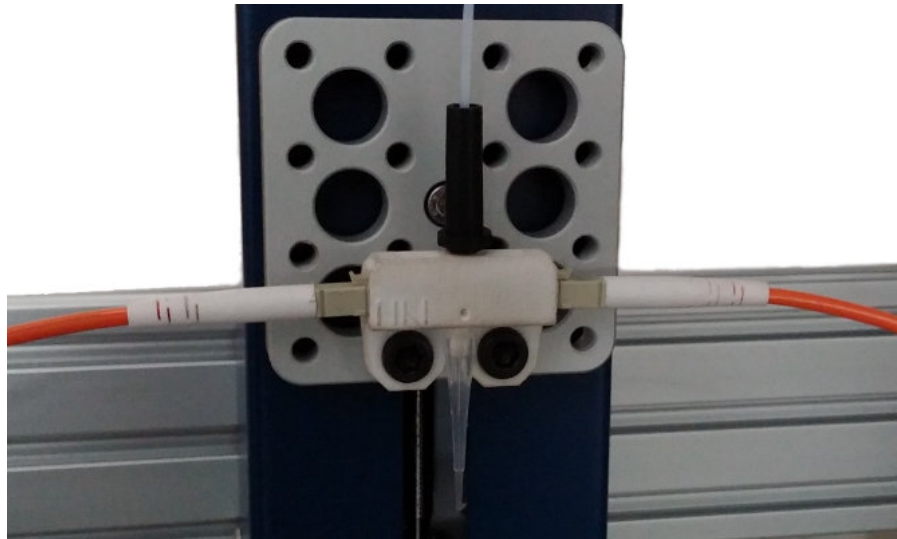
Figure 23: Third generation of the sensor design to detect single picolitre droplets inside a capillary. The AM-based design includes a concentric pigtailed fibre mount, a perpendicular capillary fixation as well as a pipette tip receptacle and an axis mount to a tool mounting plate on the neMAXYS200 positioning system (CETONI).

For the final prototype a secure capillary mount was designed (Figure 24 on the facing page, top and Figure 46 on page 115, appendix). It consisted of an inlet to fix the MicroTight® adaptor P-770 and nut F-125 (IDEX) that holds the CWI capillary in position and can optionally be screw-tightened. In turn, a validation was performed by flowing droplets of 80 µm diameter through the sensor mounted CWI capillary (Section 3.2.3 on page 27). Obtained records showed typical signal characteristics that match the previous simulation studies (Figure 24, bottom) with an average signal to noise ratio of 30 dB. This confirms the sensors ability to reliably detect droplets via refraction. Since the sensor is even able to detect droplets on a single-digit picolitre scale, a trigger threshold can be adjusted to position only regular sized droplets.

Taken together, it could be shown that the here developed compact and low-cost optical sensor is able to detect picolitre droplets of up to $\varnothing$ 15 µm. While first prototypes suffered from an unstable signal progression and an overall complex setup, the final sensor type IV can be installed in any experimental setup and adjusted for precise optical measurements (Table 4 on page 46).
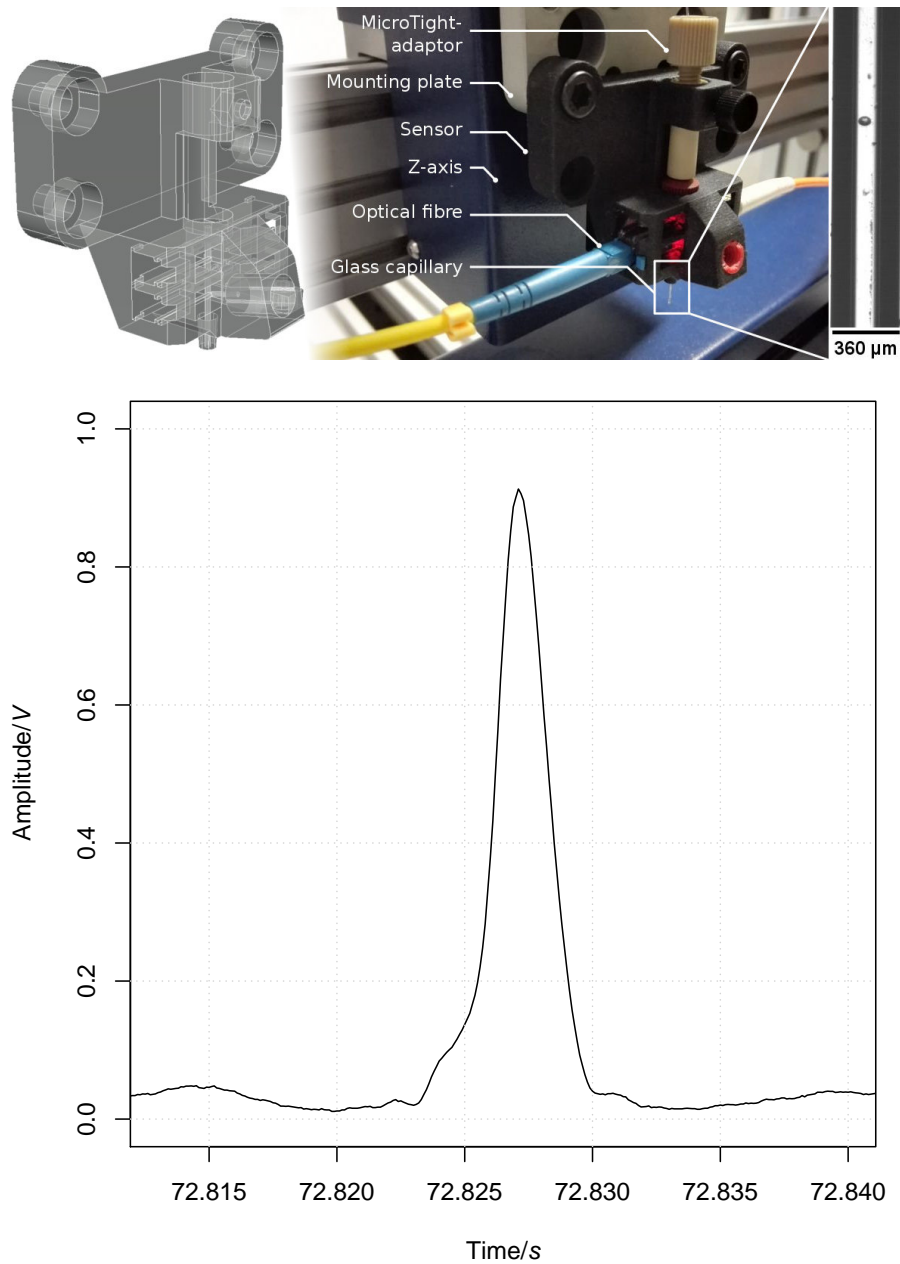
Figure 24: Final sensor design for single picolitre droplet detection in-
side the CWI capillary. Top left: 3D-CAD sensor model. Top
middle: Final 3D-printed sensor prototype with connected in- an
outgoing optical fibres in orange and yellow as well as CWI ca-
pillary mounted by the MicroTight® adaptor; Top right: Record
of a single 80 µm droplet flowing inside the capillary. Bottom:
Recorded droplet signal at 100 µs resolution.

Table 4: Summary of developed sensor prototypes.

TYPE	TECHNOLOGY	FEATURE	PROS/CONS
I/II	Milling/ Sintering	Surface mounted fibre guiding, cylindrical capillary mount	✗ Complex and brittle capillary and fibre mount ✗ Unstable droplet signal progression
III	Additive manufacturing	Fibre and pipette tip receptacle, axis mount	✓ Stable fibre mount ✗ Complicated capillary fixation ✗ Unstable droplet signal progression
IV	Additive manufacturing	Dual fibre mount, MicroTight® capillary fixation /w set screw, axis and pressurised air feed connection	✓ Stable fibre and capillary mount ✓ Adjustable capillary position ✓ Constant droplet signal, high SNR ($\approx$30 dB)

3.3.5   Sensor light-source

To guarantee a single picolitre droplet detection, a stable, reliable and powerful light source was required. To keep the whole setup as simple as possible, any optics for coupling light into fibres were omitted. Here, a commonly used Indium-Gallium-Aluminium-Phosphide-based laser diode type was utilised.

Naturally occurring fluctuations in frequency and amplitude due to temperature variations, misalignment, vibrations and the pumping source [88] make lasers unusable. To stabilise the output power a feedback circuit to the built-in photodiode is essential (Figure 25 on the facing page, A). In cooperation with Dr. Erik Beckert (Fraunhofer Institute for Applied Optics and Precision Engineering) a standard used Precision Laser Diode Driver (LDX-3545, ILX Lightwave, Figure 25, C) was evaluated and compared with an universal LED-driver for CW (constant wavelength) operations (iCSY WK2D, iC-Haus GmbH, Figure 25, B). The LDX-3454 (market value of 3000 €, weight 5.5 kg, volume $\approx$ 7500 cm³) supplied a highly stabilised laser signal but suffered from practically unusable output levels (similar to the photodiode output noise level at $\approx$ 0.1 V). However, the iCSY WK2D (market value of 6 €, weight <10 g, volume $\approx$ 0.4 cm³) showed less stability but was able to limit the laser diode fluctuations at the required power level at a current rating of 25 mA. This ultra-compact and inexpensive laser setup was utilised for all further experiments.
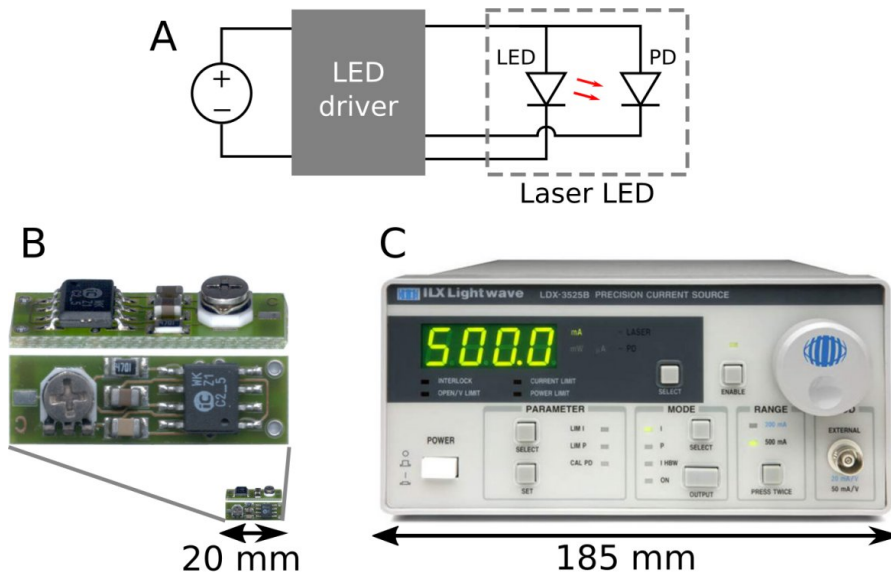
Figure 25: Comparison of possible laser LED-drivers for future setup integration. A) Feedback circuit to control the LED output via a built-in photodiode. B) Module iCSY WK2D with a length of 20 mm compared to a high precision driver LDX-3545 (C). Despite its significant lower performance yet excellent power output, the ultra-compact iCSY driver PCB was chosen for a compact setup integration.

3.3.6 Sensor comparison to commercial products

At the time of completing the droplet sensor setup a commercially available sensor for fluids was released that even included an easy connection for standard 1/16" tubings, a light source at $\lambda = 650$ nm and a handy amplifier. Balluff STM offered a compact sensor BOH-001H (STM-TSL-K16R) and an analogue amplifier BAE00NH (STM-V10-C-00) for evaluation (Figure 26 on the next page). Testing was done by inserting a transparent FEP-tubing ($d_o/d_i = 1.6$ mm/100 µm) into the sensor inlet (as the designated sensor through hole was built for 1/16" diameter tubings). By injecting pure carrier fluid (NOVEC 7500) a baseline signal at 1 V with a noise level at the millivolt range was acquired. Subsequently, 1 mm sized air bubbles were introduced into the system sequentially giving a reproducible and clear signal deviation of up to 10 V. Measurements of droplets ($\varnothing$ 80 µm) generated no signal change and could not be differentiated from a baseline signal. The procedure was repeated as aforementioned now using a fused silica glass capillary (360/100 µm). While air bubbles were recognised by an amplitude of 1 V, droplets could be not detected (signal output at zero volt). To verify the obtained results, the developed droplet sensor was connected to the current setup and showed significant signal deviations at droplet transition. This showed that the commercial liquid sensor did not fulfil the precision required here.
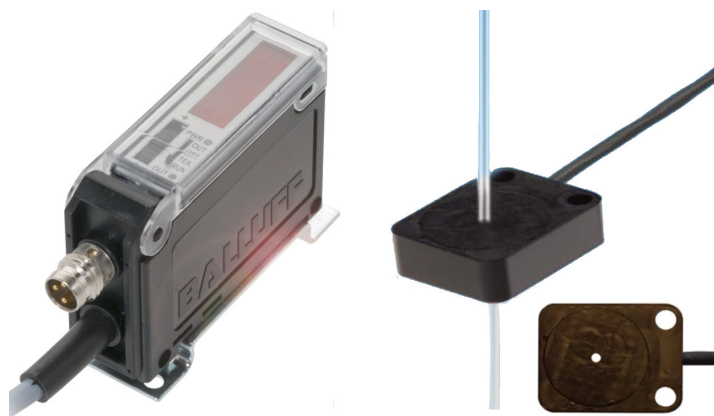
Figure 26: Commercial detection system for liquids in tubings released by Balluff STM. Shown left is the compact analogue amplifier BAE00NH (STM-V10-C-00) and right the liquid sensor BOH001H (STM-TSL-K16R) for 1/16" tubing (Images by courtesy of Balluf STM).

3.4   SOFT- AND HARDWARE DEVELOPMENTS

This section describes the hard- and software developments that were necessary to conduct, automatise and optimise all droplet microfluidic experiments. It includes automation electronics, photolithographic equipment, a valve controller and data acquisition software.

3.4.1   Electronic trigger circuit

As mentioned above, the process of a fast[3] droplet sorting, sensing, positioning and dispensing ultimately required an electronic automation control. To keep the final setup simple, fast responding and reliable a classic Schmitt-trigger-based circuit was chosen (Figure 45 on page 94, appendix). Based on the concept of its inventor Otto Schmitt in the 1930s [89], this circuitry consists of a comparator (TL-331, Texas Instruments), a feedback circuit to generate a so-called hysteresis for noise control, a signal input, an adjustable signal reference and a possibility to switch between inverting and non-inverting states. The output voltage was limited via Zener diodes resulting in an all-purpose 5 V TTL (Transistor-Transistor-Logic) signal. While the signal input originates either from a silicon photodiode and the connected amplifier or a photomultiplier tube, the output was connected to any external devices used in a specific experiment such as cameras, function generators, high voltage amplifier or a positioning system.

Otto Schmidt's ground-breaking invention was devised while he was still an undergraduate!

CIRCUITRY SIMULATION   Before assembly, the Schmitt trigger circuitry was simulated via LTSpice, a free software from Linear Technologies equipped with a SPICE simulator (Simulation Program with

---

3 Here, "fast" defines a droplet throughput of $\geqslant 100$ droplets per second, translating to a FWHM of ≈ 1 ms at given droplet velocity and size.

Integrated Circuit Emphasis). The purpose was to ensure that the planned circuit outputs a TTL-compliant valid signal as well as fast signal processing at experimental conditions. As seen in Figure 27a on the next page the circuit was tested by applying a sine wave at V_{pp} = 4 V and a frequency of 10 kHz with a power supply input between -2 V and $+10$ V; due to any failure within the circuit or the power supply that might lead to an unexpected voltage output, even uncommon situations were evaluated. Furthermore the threshold or reference voltage was set to V_t = 2.5 V and a switching behaviour at hysteresis V_h = 0.5 V). As seen in Figure 27b the simulated inverted Schmitt trigger switches between on and off states at given parameters at high frequencies. At 15, 110 and 220 µs the output slightly forms a decaying shape. When simulating at even higher frequencies (not shown) the discharging time of used capacitors significantly influences the rectangular shaped TTL-output. The current output showed values below 10 mA ensuring no harm to subsequent connected devices (Figure 27b on the following page). With this simulation, it was confirmed that the designed circuit is able to process droplet-generated signals at a rate of 10 kHz.

Subsequently, the circuitry was designed in TARGET 3001! (Engineering office Friedrich) and manufactured at Beta LAYOUT GmbH, Germany. Soldering, mounting and boxing was done in-house (Table 8 on page 96). The final setup included dual trigger functionality, state switching, reference and hysteresis regulation as well as a 15-pin D-SUB interface to standard BNC sockets for external connections (Figure 28 on page 51).

Based on the established Schmitt-trigger circuitry RISC-based[4] microcontrollers of the AVR family (ATmega) were later utilised for optimisation and scalability purposes and programmed with in-house written C-codes. This enabled a more stable, noise-reduced and significantly faster Schmitt-trigger of up to 1 MHz.

3.4.2 Data acquisition software

Acquiring, plotting and logging experimentally derived signals in real-time was and is a prerequisite for any kind of experiments. Yet, finding a suitable and cost-efficient software that meets those requirements, is able to communicate with already present hardware loggers and may have features for future adjustments is cumbersome. Initial efforts were made by Emerson Zang, who developed a C-coded and QT-framework-based DAQ interface by using Measurement Computing's API[5] Universal Library (UL) to communicate with their USB hardware loggers. Due to significant issues at runtime regarding CPU-load and limited abilities for recording and adding new features, an alternative software solutions was needed. UL's programming capab-

SPICE developed at the University of California, Berkeley (UCB) as a derivative of CANCER ("Computer Analysis of Nonlinear Circuits, Excluding Radiation"), a reference to UCB's liberalism against financed US DoD radiation studies on circuit boards [90].

---

4 Reduced instruction set computer
5 Application programming interface
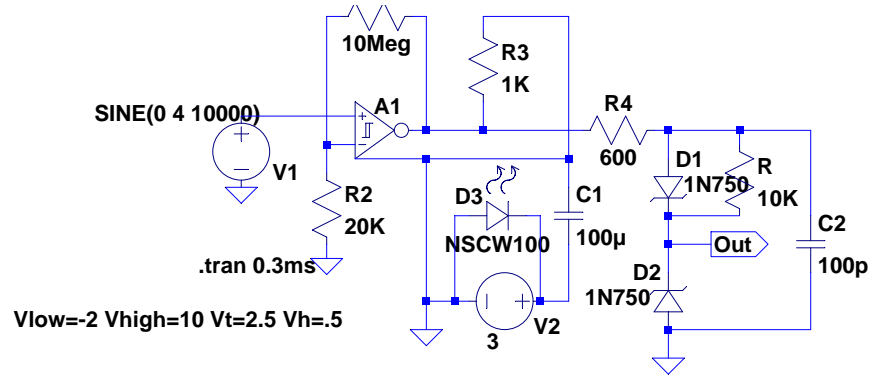
(a)
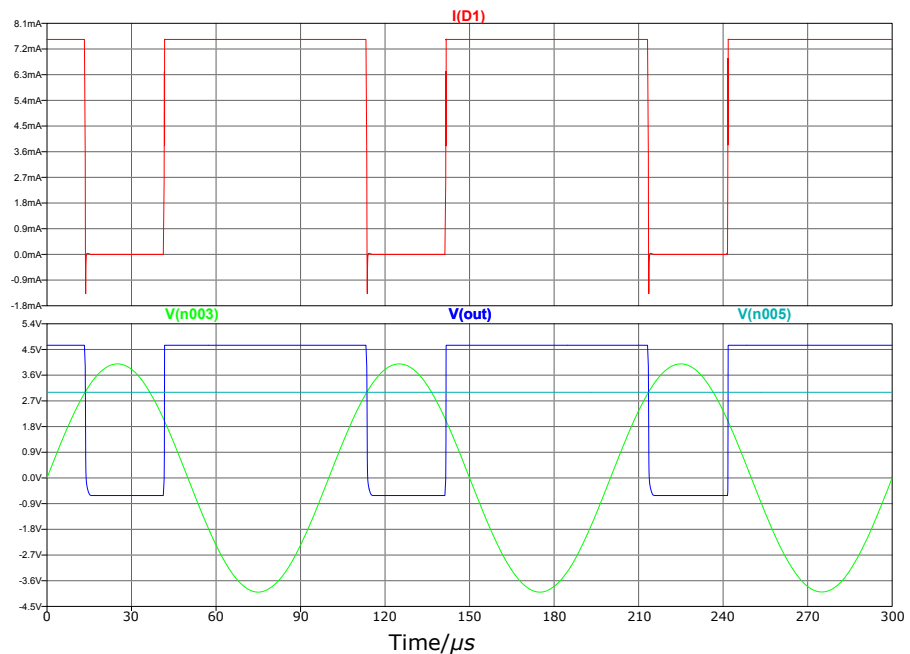
(b)

Figure 27: (a) SPICE simulation on a Schmitt trigger circuit with an input sine waveform SINE(<baseline>, <V_{pp}>, <frequency>), reference/threshold (V_t) and hysteresis (V_h) as well as power supply parameters V_{low} and V_{high}. (b) Simulated output over transient time scale (SPICE parameter .tran = 0.3 ms) at given parameters including trend of current.

Figure 28: Final dual Schmitt trigger setup with modular D-sub connector interface.

ilities enabled to interface data loggers via a Laboratory Virtual Instrumentation Engineering Workbench (LabVIEW®, National Instruments). With its modular structure UL-modules for hardware connectivity could be combined with LabVIEW®-modules for any kind of data processing. This included algorithms for peak-finding or FFT-analysis[6] as well as plotting and recording of multiple signals in parallel and in real-time. It was now possible to acquire data at utmost sufficient sample rates of up to 500 kS/s[7] depending on the connected hardware. This enabled to build a software (Figure 29 on the next page) with the following features:

- Interfacing hardware logging devices from Measurement Computing

- Configuration of analogue ports (port range, voltage range/precision, sampling rate)

- Plotting of analogue signals separately or simultaneously at adjustable time span

- Configuration of digital I/O ports (*e. g.* to remote control external devices) and counter input ports (for incoming pulses)

- Displaying counts as absolute value and as frequency

- When counter reaches an adjustable threshold, send notification visually and by triggering a digital out port

6 Fast Fourier transform—an algorithm to extract frequency information out of digital signals
7 S refers to samples, *i. e.* analogue signal intensities digitally converted

- Recording of multiple signals simultaneously into a text file with ASCII[8] format including an actual timestamp, a comment section, absolute and relative times, an automatically generated table header and a limited and unlimited recording time option

- Automatic detection of peaks, valleys, amplitude and period of a signal in real-time

- Security switches that deactivate certain acquisition configuration parameters when logging is active.
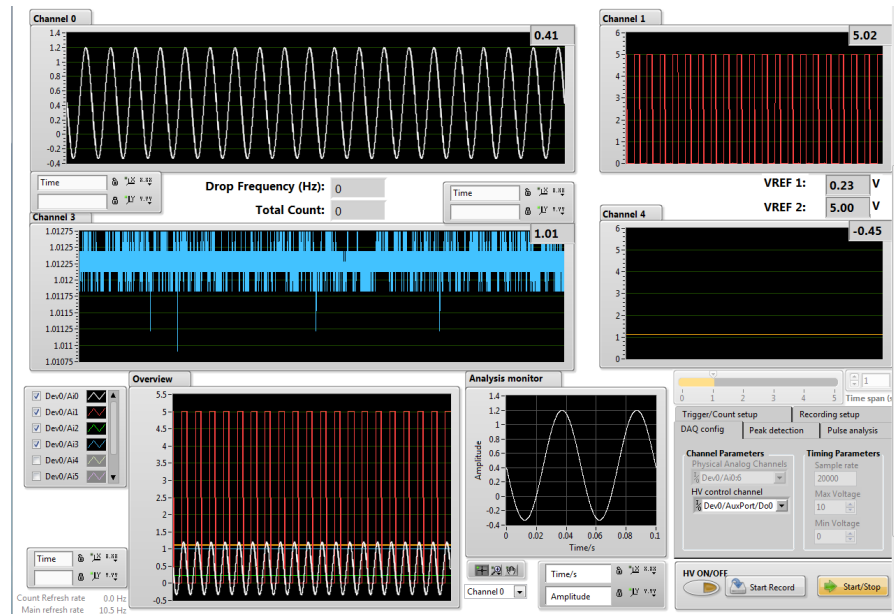
Figure 29: Custom LabVIEW®-based DAQ software front-end to visualise and process data acquisition from any Measurement Computing's logging hardware.

DAQ SOFTWARE ARCHITECTURE   The software was designed to minimise CPU load and use of resources. The framework is based on nested structures that enable an intelligent execution of program units on-demand. The primary structure is a stacked sequence with two frames that execute one after another. The first frame includes a main configuration while the second frame has two separate executable while loops and event structures with various substructures. A feature called value signalling is used for capturing changes from front-end controls (*i. e.* button pressed, value of a slider control adjusted) that is passed to linked local variables to trigger an event structure which in turn executes other functions. Here, the initiation of an event to create a virtual channel for data acquisition is triggered when Start is pressed by the user on the front panel (Figure 30). Further runtime optimisation included a main timeout loop of 100 ms,

---

8 American Standard Code for Information Interchange

translating to a refresh rate of 10 Hz, *i. e.*: Data will be collected from an internal buffer and displayed ten times a second. This could result in a buffer overflow in case more data is stored temporarily then collected. During the development phase, buffering issues were evaluated and adjusted to existing hardware requirements, accordingly.
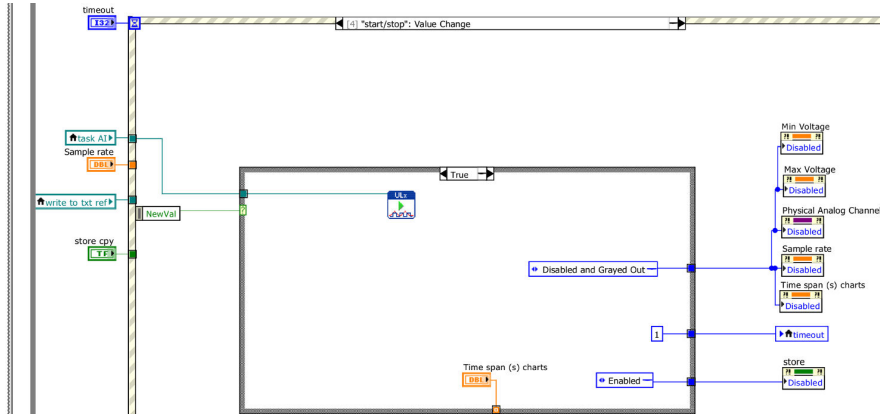
Figure 30: DAQ software execution procedure when pressing start after configuration is set. Outer left border shows stacked sequence, following a while loop and a triggered event structure.

3.4.3 Photolithography equipment

Evaluating designed microfluidic structures (as seen in Section 3.1 on page 16) in no time requires equipment for quick manufacturing like the production of PDMS chips (Section 2.1.2 on page 7). Since such devices are cost-intense, approaches were made to build necessary tools for in-house production. The general process flow includes a primary coating step of photoresist on a matrix (*e. g.* a silicon wafer) using centrifugal forces applied by a spincoater, subsequent polymerisation processes induced by light of a certain wavelength ($\lambda = 365$ nm, so called "i-line") and further developing, rinsing and baking steps.

SPINCOATER   The core components of this device is a drive of high speed and high precision that was dismounted from a PC hard drive. The induction motor was interfaced by a microcontroller. An in-house developed C-program was used to control the drive via various pulse width modulation (PWM) sequences. A precise revolution control was accomplished by utilising a high speed camera with a preset reference marking. Prior to its first use for spin coating, a vacuum connection was mounted by drilling a 3 mm borehole into the ball bearing drive shaft. Motor, microcontroller, a display and power supply IC's were finally mounted in a custom CAD-designed (Figure 47 on page 116, appendix) and 3D-printed polyamide housing (materialise on-site). With this, in-house coating procedures using SU-8 negative epoxy photoresist could be performed (Figure 31).
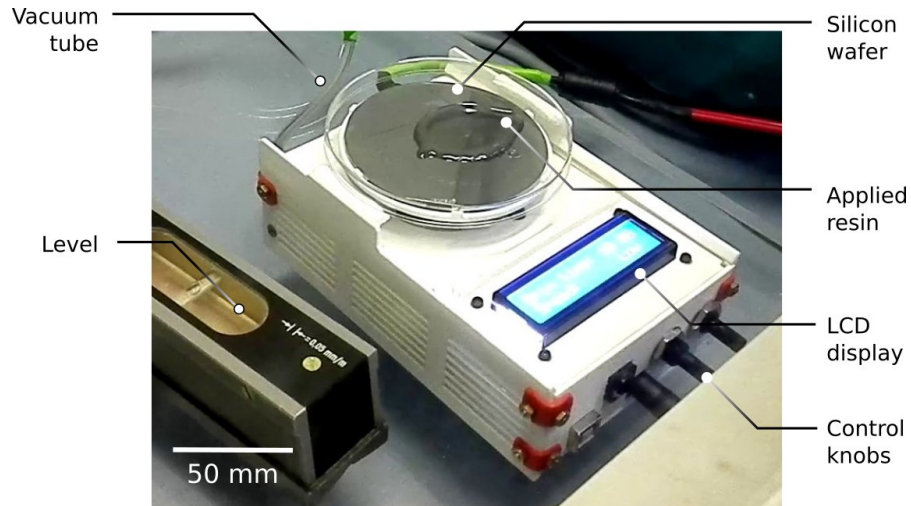
Figure 31: In-house developed spincoater with an Arduino controlled induction motor from a hard drive and a 3D-printed housing made of polyamide. Record shows first coating approach on a three inch wafer with applied negative resin.

UV-LIGHT SOURCE   A dimmable high power UV-light source needed to be developed for the hard-lithographic SU-8 development step. Since traditionally used mercury lamps are pricey, bulky and need additional cooling and optical filters, efficient and affordable UV-LEDs were evaluated. A high-power LED (NCSU276AT-U365, Nichia, λ_{max} = 365 nm) was combined with a PWM[9] remote controllable 500 mA current source (Lumitronix 95066) and a potentiometer with PWM function (Lumitronix 95019). This specific LED was chosen, as the spectral half width $\delta\lambda$ of 9 nm guarantees a controlled emission of UV radiation. Due to the LED's high divergency (±70° at 50 % radiant intensity) a 75 mm collimation lens (COP4-A, Thorlabs) was mounted above the LED to homogeneous irradiate the required wafer area (Figure 32 on the next page).

3.4.4 Solenoid valve controller

For performing a DOI dispensing experiment starting from reinjecting and sorting, at least two droplet populations at highly differing ratios had to be generated. Therefore, a precise fluid control mechanism was necessary that closes a diverting tubing from the chip to a reservoir, in case a preset droplet threshold count is reached. This was accomplished by utilising a pinch solenoid valve controlled by a customised relay board and an in-house developed LabVIEW® serial RS-232 interface control (Figure 33 on the following page).

COMMAND TRANSMISSION   The relay control was implemented into LabVIEW® via interfacing an on-board microcontroller which

---

9 PWM: Pulse width modulated

Figure 32: Developed high power UV-source using a NCSU276A LED
(Nichia Corp., Japan) for in-house hard lithographic production
of microchannel structures in SU-8, boxed and equipped with a
∅ 75 mm collimation lens (Thorlabs) to expose silicon wafers of
three inch diameter.

accepts a sequence of a 4-byte command sequence. An example for
simple data transmission is shown in Table 5. For testing purposes
the program HTerm was utilised to establish a serial communication
as well as sending and receiving serial data.

Table 5: Example of initialising a connection to relay card 1 (= the first card
in a card network) and switching relay 1 by sending a serial 4-byte
command frame represented as binary string.

	COMMAND	ADDRESS 1	DATA	CHECK SUM
Send Init	0000 0001 (1)	0000 0001 (1)	0000 0000 (0)	0000 0000 (0)
μC response	1111 1110 (254)	0000 0001 (1)	Info	–
Send switch	0000 0011 (3)	0000 0001 (1)	0000 0000 (0)	0000 0010 (2)
μC response	1111 1101 (253)	0000 0001 (1)	Data	–

HEAT DISSIPATION CONTROL   The here utilised valves can gener-
ate a maximum pinching strength of 0.25 kg at a power dissipation
of 4 W, resulting in a significant emission of heat. To avoid unwanted
heating of the mounted tubing and the inside flowing droplets, it was
necessary to adjust the applied current flow. Based on Faraday's law
of induction, limiting the current decreases the valve's heat dissipa-
tion but also the pinching strength of the force generating magnetic
coil

$$\epsilon = \frac{d\phi_B}{dt},$$
(9)

where ϵ is the electromotive force and ϕ_B the magnetic flux. Therefore, a balance had to be struck between the valve's closing ability and its power consumption by empirically testing high power resistors of different values (10–50 Ω).

VALVE-RELAY SETUP   In default mode, any physical valve-to-relay connection wires to NO (normally open) to ensure no current flow. Only when the user triggers a relay actuation, the circuit closes and the valve including the power resistors are energised. The C-common relay connection is wired in series starting from the main control (Figure 33, right).
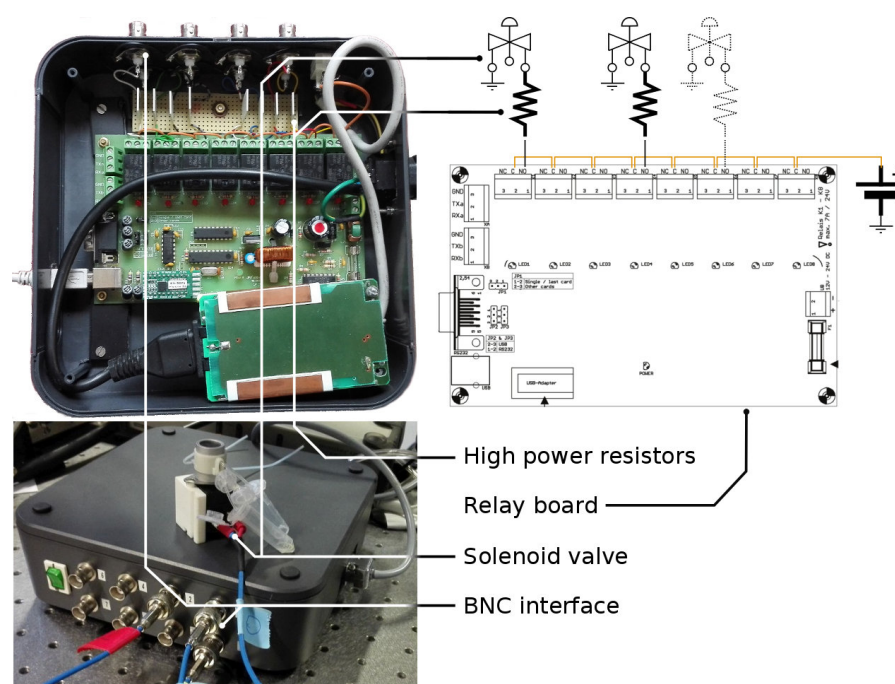
Figure 33: Developed valve-controller. Left: Prototype with connected solenoid valve and attached PTFE tubing for automated microfluidic process control. Right: Connection schematic.

3.4.5   Positioning and dispensing concepts

This section will introduce the basic structure of the developed positioning scripts to deposit a single droplet (see Listing 5 on page 101 (appendix) for complete code). Because it is directly connected to the dispensing process, both procedures will be explained here more in detail. The positioning process can be divided into multiple steps (Figure 34 on page 58). The primary step initiates the device communication and starts a positioning algorithm that sets required parameters by user-input, such as: default X/Y/Z-coordinates of waste position, relative geometric parameters of the target compartments (microwell plate, Petri dish, glass matrices) and a delay for droplet dispensing.

Out of that, terminating and boundary condition are calculated by the algorithm. In the next step, a conditional loop is executed that moves the capillary to a predefined waste position and checks if a terminating condition was reached. Such a condition can be the number of available compartments of a microwell plate. If the condition is true, the positioning process stops. If false, the script execution continues and waits for a trigger signal (a detected droplet) on the positioning systems I/O port. If this signal equals 1 (5 V TTL-signal) the loop execution continues and starts a delay timer to handle the spatial difference from droplet sensing to dispensing (Section 3.2.4). The capillary is then moved out of the waste to a calculated X/Y position. As an example, circular positions for a Petri dish were computed via

$$x = x_{\mathrm{def}} + r \cdot \cos\left(\frac{\alpha \cdot \pi}{180}\right) \tag{10}$$

$$y = y_{\mathrm{def}} + r \cdot \sin\left(\frac{\alpha \cdot \pi}{180}\right) \tag{11}$$

where x/y_{def} represents the waste position, α the preset angle pitch and r the Petri dish diameter. Based on the applied dispensing type, further executions can now take part: Either droplets will be transported by contacting the target surface or contact-free by moving the capillary to a proximate surface position and initiate a droplet transfer via pressurised gas (Figure 35 on page 59). In the next step the delay time is checked if being expired (droplet reached compartment). If true, the capillary is moved back to the waste position; if not, the capillary is kept in positioning until reaching temporal terminating condition.

ANALYSES OF POSITIONING SYSTEM'S AXIS SPEED For achieving a proper single droplet dispensing, the temporal characteristics of the positioning systems X/Y/Z-axis needed to be analysed. A crucial requirement is that the droplet delay time t_d must be greater or equal to the positioning time t_p. This includes an examination of the positioning route as described consecutively.

At maximum velocity, the Z-axis moves eight times slower than the X/Y-axis ($v_z = v_{xy}/8$ =25 mm/s). Having a Petri dish with a maximum usable radius of 40 mm and a central waste position (Figure 17 on page 35), the farthest location a droplet can be deposited, sums up to the following three steps:

1. One Z-movement of the capillary from central waste position until reaching a secure Z-position above the agar medium surface ($z1$, at fixed X/Y-position) calculates to a default of 5 mm plus agar medium height ($z2$, $\approx$2 mm).

2. A subsequent combined X/Y-movement of the Petri dish to locate the computed dispensing position beneath the capillary exit, gives a maximum of 40 mm.
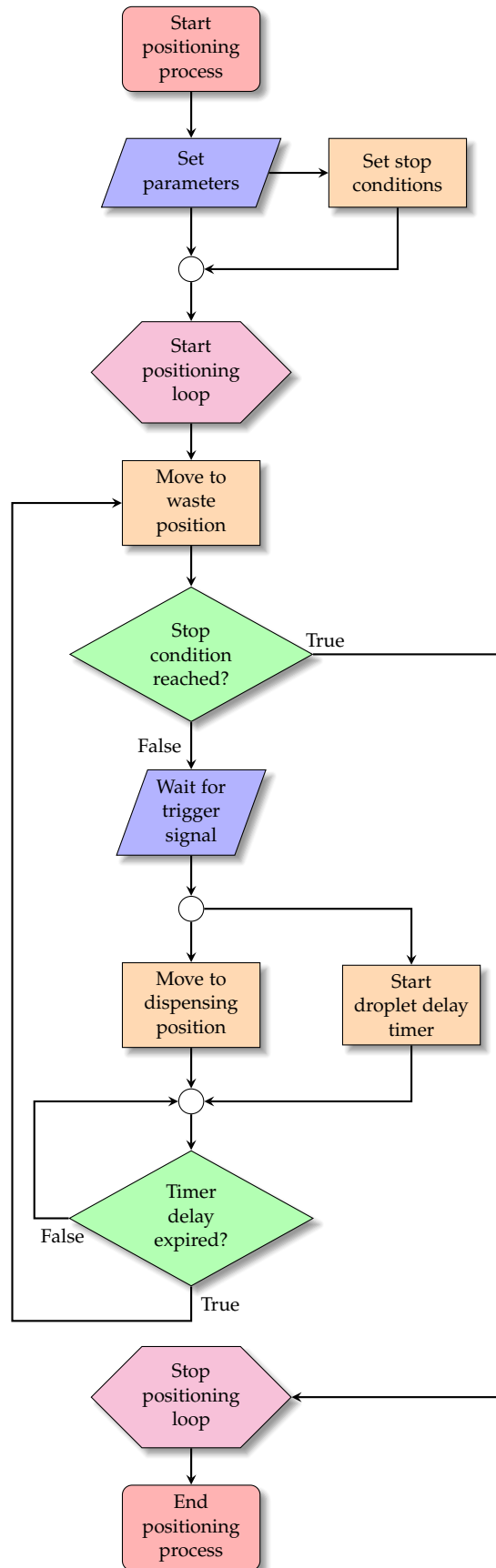
Figure 34: Flowchart for a single droplet positioning.
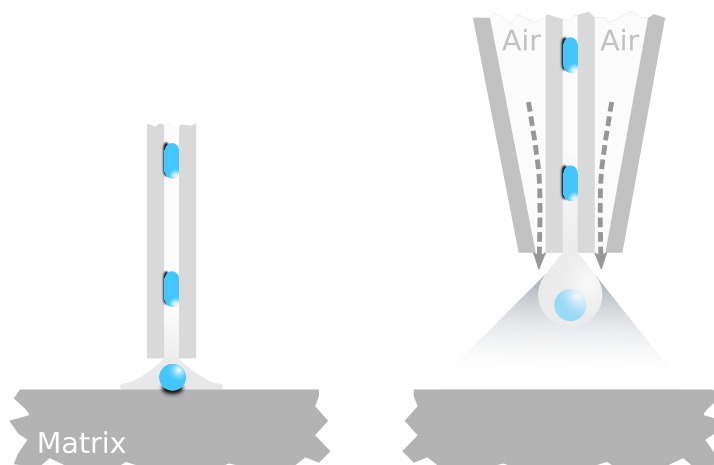
Figure 35: Droplet dispensing modes. Left: Contacting mode in which the capillary touches a target surface, so that carrier fluid and droplet will flow out passively. Right: Non-contacting mode, where the capillary is located proximate to the surface and an effluent droplet will be actively dispensed by a directed, pressurised air flow.

3. The last step includes one further Z-movement until contacting the agar medium surface; default $5\,mm$ (z1). The total position time then calculates to

$$t_p = 2t_{p,z1} + t_{p,z2} + t_{p,xy}. \tag{12}$$

The farthest positioning route can be processed in $680\,ms$ and meets the required condition of $t_d \geqslant t_p$, even if sorting in the chip takes place at up to five times higher speeds. Thus, at the selected droplet sorting speeds, the limiting factor to setup a dispensing delay mostly depends on the time that the droplet needs to exit the capillary after the sensor (delay time t_d).

3.4.6 Classification of dispensed droplets

A classification algorithm in R—similar to the peak recognition algorithm (Section 2.6.1 on page 12)—was developed to qualitatively and quantitatively estimate positions of dispensed droplets (Listing 4 on page 98, appendix). As recorded data sets of sensing and position differed regarding time and sample rate, a synchronisation step was needed. This necessitated the conversion of relative time stamp strings to absolute, second based daytime values and the introduction of adjustable time windows for value extraction by averaging. The synced data was then used to classify dispensed droplets into the following three types:

The utilised DAQ-card, configured to 10 kS/s could not be linked to the neMAXYS' internal data acquisition unit with a maximum sample rate of 10 S/s.

DISPENSED DROPLETS TYPE I ... define those, who generated a digital TTL-signal and initially triggered the positioning (Figure 36

on the next page, orange). Six different criteria (linked with a logical AND) were necessary to classify droplets of type I:

Criteria 1–3: Does the time stamp of a recognised peak with its corresponding current x- and y-value (Petri dish) and z-value (capillary) equal the Petri dish's waste position $p_{x,y,z}$?[10]
In other words: Is the capillary located in its default waiting position (waste) when a droplet peak occurs?

Criterion 4: Is the interpeak distance (*i. e.* difference between two proximate peaks, Figure 36 on the facing page) above a critical time range threshold?[11]
In other words: Are multiple droplets occurring at the sensor site in a short time? If yes, select the first that initiated the positioning process as type I and categorise the following droplets as type II/III.

Criterion 5: Does at a peak time plus 750 ms the z-value reach a maximum?
Or in other words: Did the capillary completely move out of the waste position to the highest preset z-position after the empirically estimated time of 750 ms? This border condition check should ensure that the positioning process started and a droplet will be dispensed.

Criterion 6: Does after a predefined delay time t_d the peak corresponding z-value match the z-value of the agar medium surface?
In other words: Is the capillary positioned on a x/y location of the agar medium surface after the assumed travel time, so that an exiting droplet will be correctly dispensed?

If non of all above listed criteria matched a current droplet peak identification, a further classification for type II and III was applied.

DISPENSED DROPLETS TYPE II/III ... include all droplets that passed the capillary during an active positioning, so-called inter-droplet candidates, or short: IDC. Those in turn can be sub-classified as IDCs that either contributed to a dispensing position (II, red) or went to waste (III, blue) (Figure 36). The following conditions will classify droplets by their corresponding z-values of the capillary, since x- and y-values greatly differ per dispensed position. The first condition logically combines one of the consecutively listed criteria 2, 3 or 4.

Criterion 1: Is the corresponding z-value after an approximated travel time unequal to the z-value of the agar medium surface?

---

10 Due to varying waste positions, waste coordinates were automatically extracted from raw positioning data by $p_{x,y} = (x,y)_{max} - 0.5d$ and $p_z = z_{min}$, where diameter d was calculated by $d = (x,y)_{max} - (x,y)_{min}$

11 Defined as the data sets sampling rate multiplied by a constant, here: 1000

Or in other words: Is the analysed droplet presumably heading to the waste position?

Criterion 2: Does, accordingly to the prior condition 1, the capillaries z-value match the waste z-value after the droplets travel time?

OR criterion 3: Does 300 ms[12] after the travel time expired, the z-value match the waste z-value?
In other words: If a droplet reaches the end of the capillary at the moment a movement back to waste occurs, the corresponding z-value might have an arbitrary value (border conditions). As positioning happens in under a second, a time of 300 ms was set to approximate the final dispensing position.

OR criterion 4: Is the z-value at travel time minus 1.1 to 1.25 s[12] matching the z-value of the agar medium surface?
Expressed differently: If condition 1 clearly assumes a waste deposition, but condition 2 and 3 fail, the capillaries z-value prior to the movement back to waste should equal the z-value of the agar medium surface.

After this conditional check, droplet peaks were classified as IDCs going to waste (type III) when two of the above specified conditions were met. In a reverse conclusion, all droplets that did not meet this condition, were classified as type II. The following sensing and positioning plot should help to understand this approach (Figure 36).
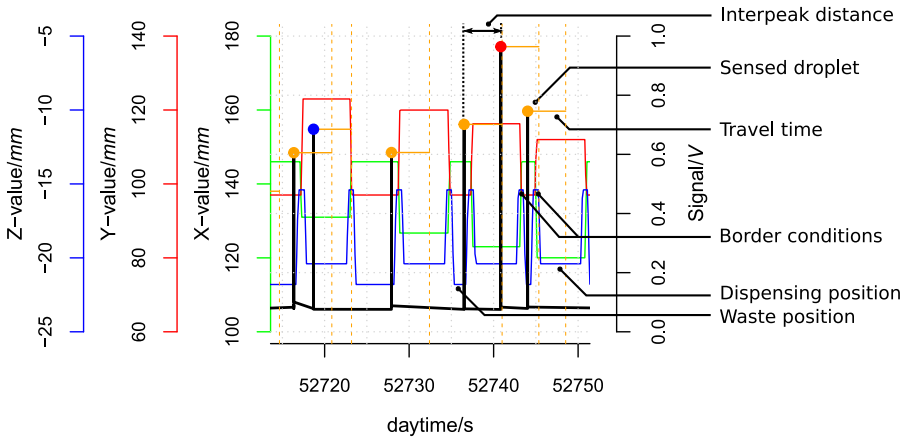
Figure 36: Sensing and positioning plot with droplet signals and x/y/z-values of the positioning system. Orange labelled peak dots depict droplets of type I (hits), red dots show type II (contributed) and blue markings indicate droplets of type III (waste).

---

12 empirically estimated

3.5   SYSTEM EVALUATION AND CHARACTERISATION

As a model for evaluating the here developed process it is necessary to prepare at least two different droplet populations regarding their ratio as well as their optical and biological content. By this, a sorting process can be set up to differentiate and relocate only those droplets matching the expected criteria. This furthermore simplifies the final readout after positioning and dispensing. The following experiment utilises an additional population to facilitate the configuration of initial fluidic and sorting parameters.

WORKFLOW   Three different droplet populations were generated: 1) *E. coli* producing the red fluorescent protein mCherry, 2) fluorescein at low concentration and 3) microparticles with high concentration of fluorescein (Section 2.2.1 on page 9). After generation, droplets were directed into an incubator unit [61] and incubated over night (Figure 38a on page 65). After reinjection into a sorting-chip, only highly green fluorescent droplets were deflected into the positive channel. Then, the connected CWI capillary guided the sorted droplets onto a Petri dish by contacting the agar medium surface. After dispensing, the Petri dish was sealed and incubated at 28 °C for 24 h. Deposited contents were then further analysed.
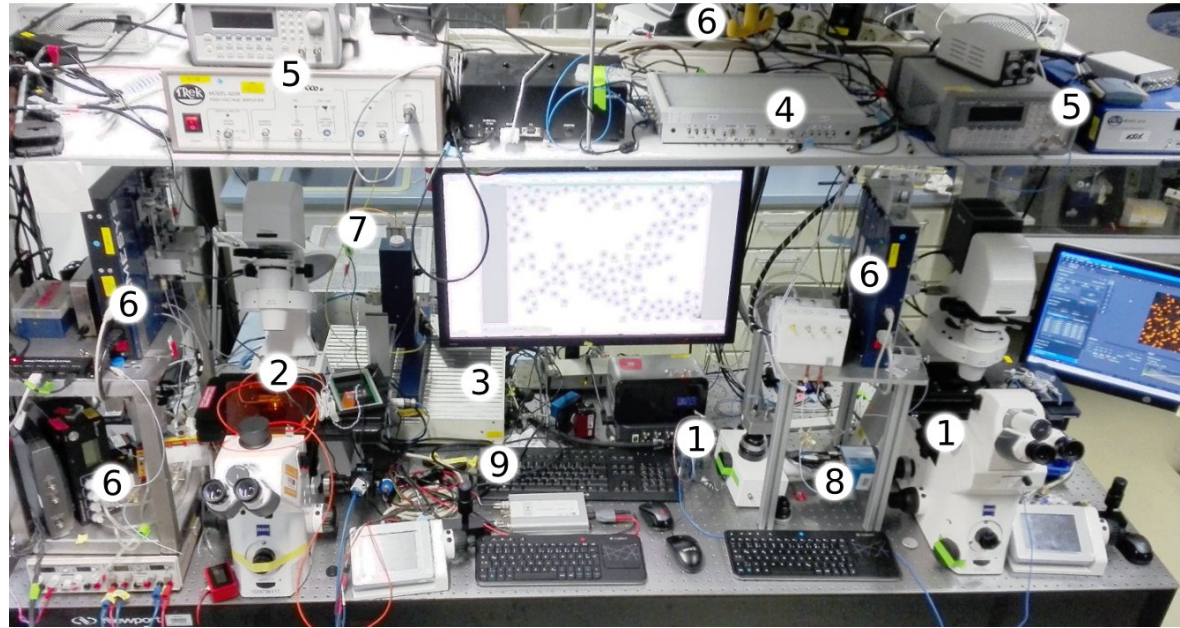
Figure 37: Lab view of established screening system. 1) shows the workstation for droplet generation and post-processing with the developed solenoid valve-controller at left side. 2) Workstation for droplet sorting connected via the CWI to a positioning system with installed sensor (3) to detect and deposit DOIs. Core components for process automation are the trigger unit with an integrated DAQ card and a photodetector amplifier (4). The linked frequency generator and high voltage amplifier (5) allows for DEP-based sorting. 6) show pressure and syringe-based pumps for precise flow control at nanolitre level. Light sources for fluorescence-based droplet sorting, *i.e.* lasers of different wavelength are encased inside a metal box (7). For image and optical signal recording high-speed cameras and a photomultiplier tube are depicted under 8 and 9.

3.5.1   Sorting results

Stable sorting conditions of 50–100 droplets/s were utilised to minimise false positives and negatives. In this steady five hour experiment ≈1.3 million droplets were reinjected. Using high-speed videos, it could be confirmed that no false positives were observed for 975 reinjected droplets at various points in time. Using triggered imaging [60], 115 sorted droplets were confirmed to be true positives, as all contained microparticles. However, 2 % satellite droplets ($\varnothing \leqslant 15\,\mu m$) were observed to bypass the sorting junction, *i.e.* passively flowed towards the positive channel and contaminated the downstream situated dispensing (Figure 39 on page 66). Sorted droplets were additionally validated by microscopic and fluorescent imaging (Figure 38b on the next page).

A complete record during the whole experimental time (97 min) would have resulted in 12 TB(!) of raw image data.

3.5.2   Analyses of inter-droplet spacing and delay timing

While spatial and temporal characteristics between reinjected droplets is fluidically controlled (Figure 40 on page 67, B), an exponential probability distribution (Figure 40, D) describes the waiting time for positive droplets that are sorted and subsequently detected in the capillary. In this experiment, two sorting events occurred either between 50 ms or up to 120 s, with an average of 6.42 s. A similar time of 6.59 s was calculated between two detected droplets in the sensor. This slight difference results of changes in droplet velocity at transitions (chip/capillary, capillary/Petri dish) and inside the capillary leading to drop in pressure.

As a fluidic opto-mechanical system certain boundaries restrict the throughput capabilities of the here presented system. The inter-droplet time is a critical factor that should be adjusted in order to maximise the dispensing frequency of single droplets. For this experiment, the physical positioning time t_p from waste to deposition location constitutes below one second and was maintained at the target for an additional ≈5 s. Thus, events occurring below 6 s might have been deposited together. Analyses of the collected signals indicate that multiple positions might have ended up with more than one droplet. Also a notable amount of droplets got deposited on the waste position (Figure 42 on page 69).

3.5.3   Results of droplet dispensing onto media in Petri dish

In order to evaluate the quality of the sorting and deposition process, microscopic observations of each dispensing spot were performed in bright field and fluorescence (Figure 41 on page 68). 70.5 % of all dispensed positions were found to contain microparticles (Table 6 on page 70). Additionally, less than 6 % of the positions contained both microparticles and cells, which most probably originated from satellite droplets containing cells. However, only cells were also ob-
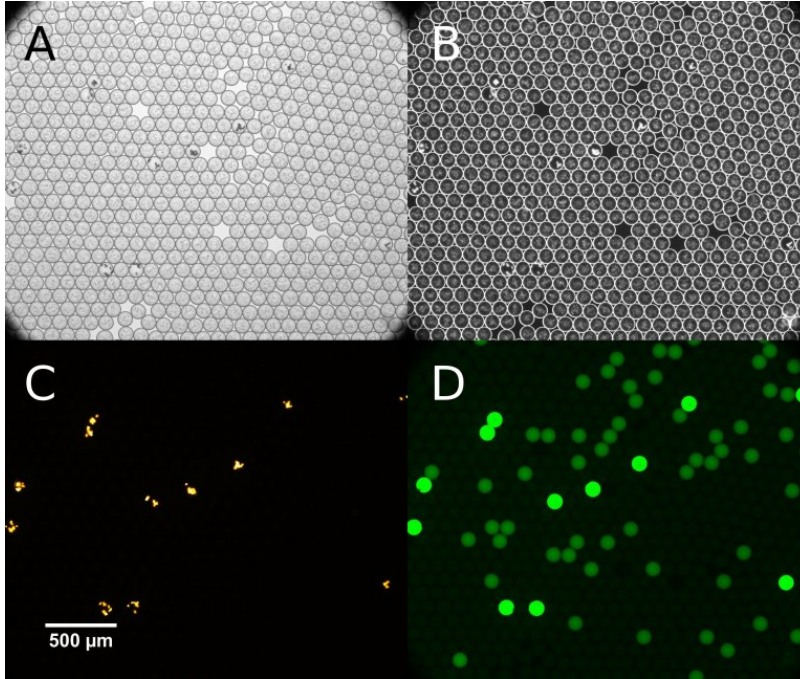
(a) Generated droplets showing three droplet populations in A) Bright-field, B) Phase contrast, C) Red filtered fluorescence and D) Green filtered fluorescence.
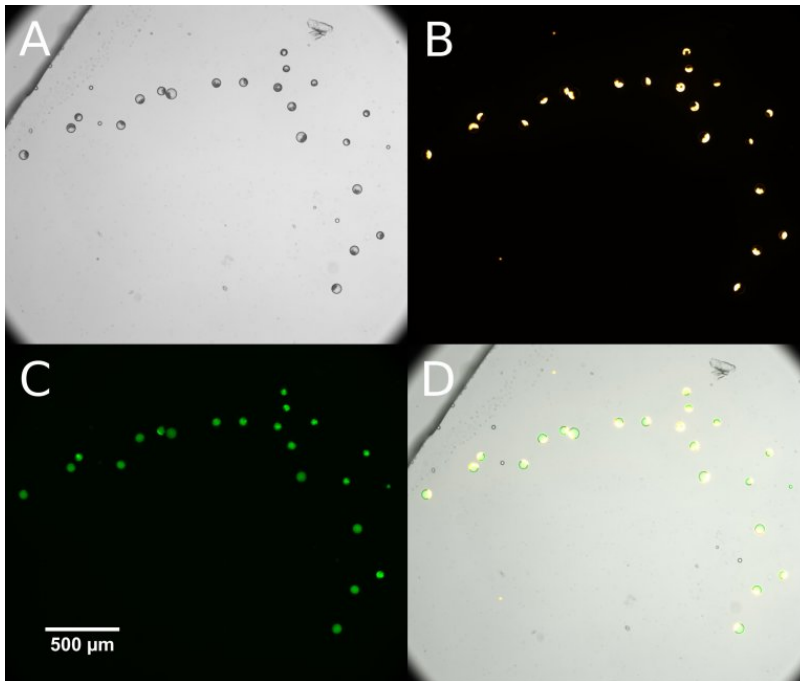
(b) Sorted droplets inside an observation chamber. A) Bright-field image, B) Fluorescence image at $\lambda_{ex}/\lambda_{em}$ 550/605 nm showing droplets with encapsulated microparticles, C) Fluorescence image at $\lambda_{ex}/\lambda_{em}$ 488/525 nm showing fluorescein labelling, D) Overlay of all images.

Figure 38: Comparison of generated and sorted droplet populations.
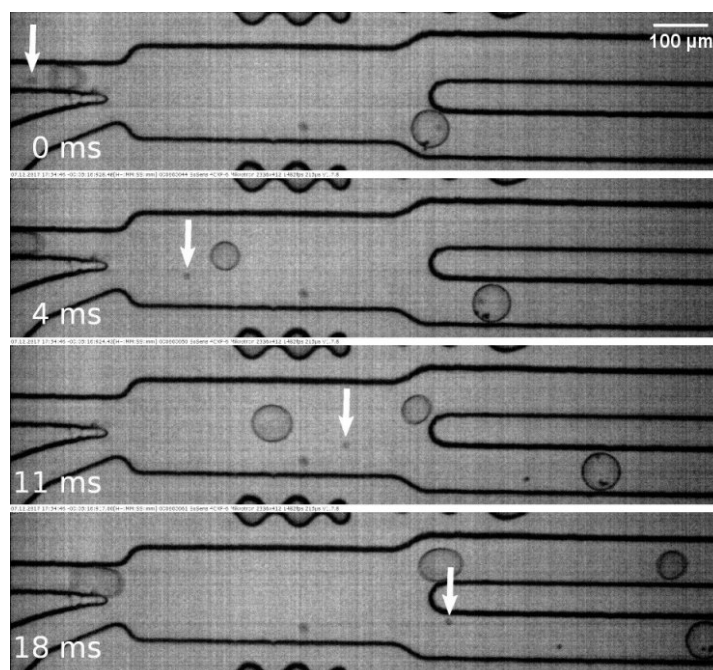
Figure 39: Droplet sorting and satellite contamination. While no false
negatives or false positives were observed, satellite droplets of
$\varnothing < 15\,\mu m$ can flow to the lower positive channel.

served in 5.2 % of the positions (Figure 43 on page 70, left). Lastly,
neither microparticles nor cells were found in 18.4 % of the positions.
This is most probably caused by either satellite droplets that wrongly
triggered dispensing or by droplets that moved slower through the
capillary than anticipated. In the end, these droplets were deposited
at the waste upon capillary return due to delay time expiration.

3.5.4   Estimation of deposited droplets

The number of actual deposited droplets of all 70.5 % dispensed posi-
tions was determined using manual microparticle count. The particle
number inside a droplet follows a Poisson distribution, in this case
with an average of 12.5 microparticles per droplet. Using this inform-
ation, it can be concluded that there is a 10 % probability for the
occurrence of droplets containing less than 7 or more than 18 mi-
croparticles. Hence, on positions with particles, approximately 45 %
are expected to have only one droplet. The remaining positions may
contain two or more droplets because of an unusual high number of
detected microparticles. However, these numbers are inferred from
probabilities and are therefore without complete certainty on these
proportions.

Based on the classification approach in Section 3.4.6 it was possible
to infer 91 positions in which more than one droplet would be de-
posited (Figure 42 on page 69). If it is assumed that all of them have
particles, the fraction would account to 45 % (91 of 203).
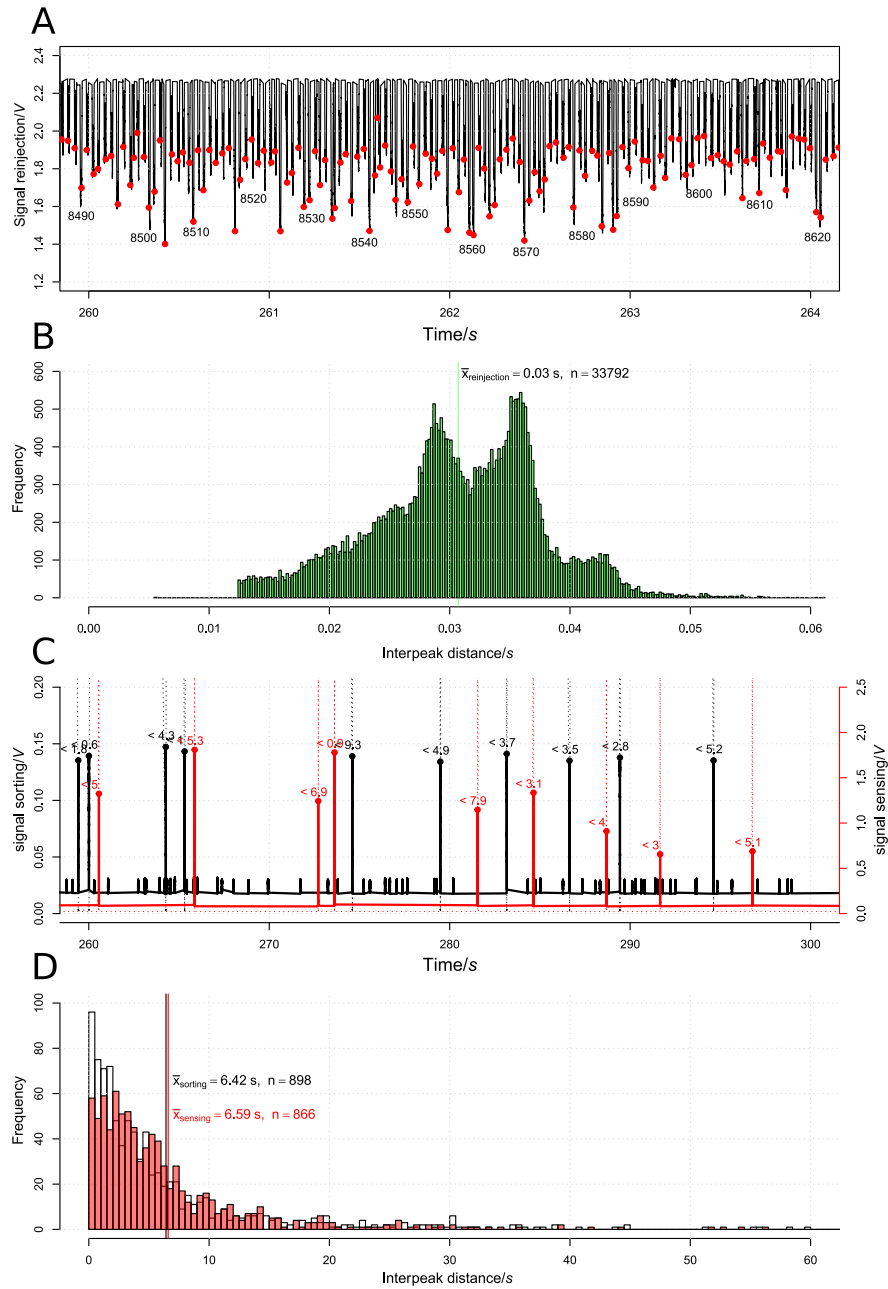
Figure 40: Distance between proximate droplet signal peaks at different process stages. A) Absorbance peaks at reinjection with corresponding droplet counts and histogram (B). C) Fluorescence peaks of sorted droplets on chip (black) and detected refraction-based peaks at sensor site (red) with interpeak distance to its predecessor and associated histogram (D). Coloured vertical lines mark position of average inter-droplet distance.
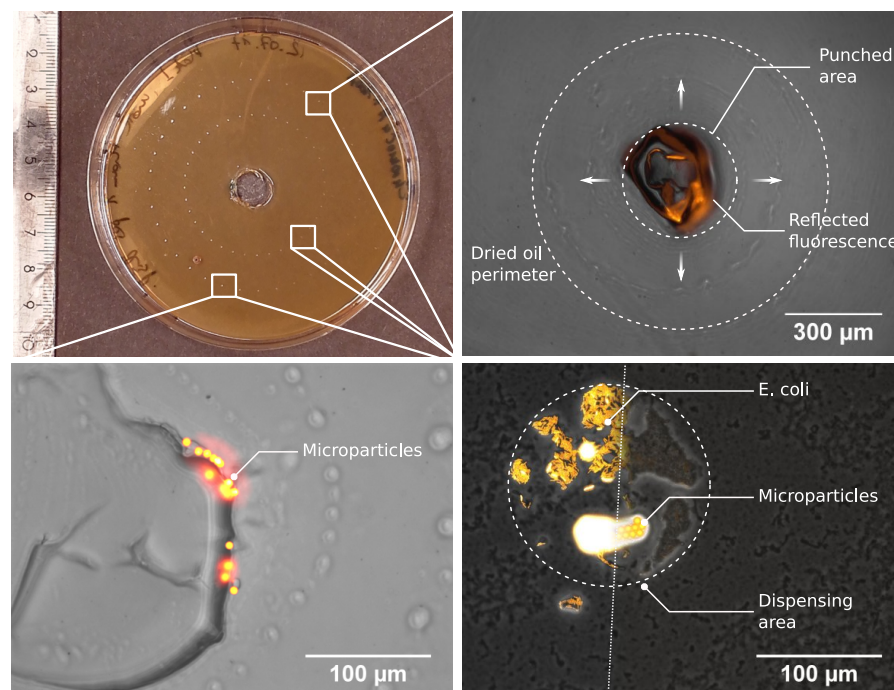
Figure 41: Triggered dispensing of single sorted droplets on Chromocult®
Coliform agar medium surface in a Petri dish (top left). Top
right: Area with no observed dispensed content. Dashed inner
circle represents capillary punching area, dashed outer circle
depicts circumference of evaporated continuous phase. Bottom
left: Deposited content of sorted droplet carrying fluorescent
microparticles of $\varnothing$ 5 μm. Bottom right: Co-deposited *E. coli*
and microparticles shown as an overlay of two different time-
exposures marked by a white angled line.

3.5.5   Comparative analyses

Similar results were obtained in an experiment in which sorted drop-
lets contained a GFP-producing *E. coli* strain. Droplets with the highest
green fluorescent signal were isolated from a vast majority of droplets
with *E. coli* producing mCherry. Over 66 % of the depositions (279/
420) contained a single green colony. The remaining spots were either
empty (17 %) or contaminated by a red colony (17 %). Here, it is im-
possible to determine if green colonies arise from a single or more
droplets with GFP-producing cells (Figure 43 on page 70, right). For
better conclusions, an additional quantitative PCR is necessary. With
this tool, it should be easier to determine if the amplification curves
result from the contents of a single or multiple droplets.
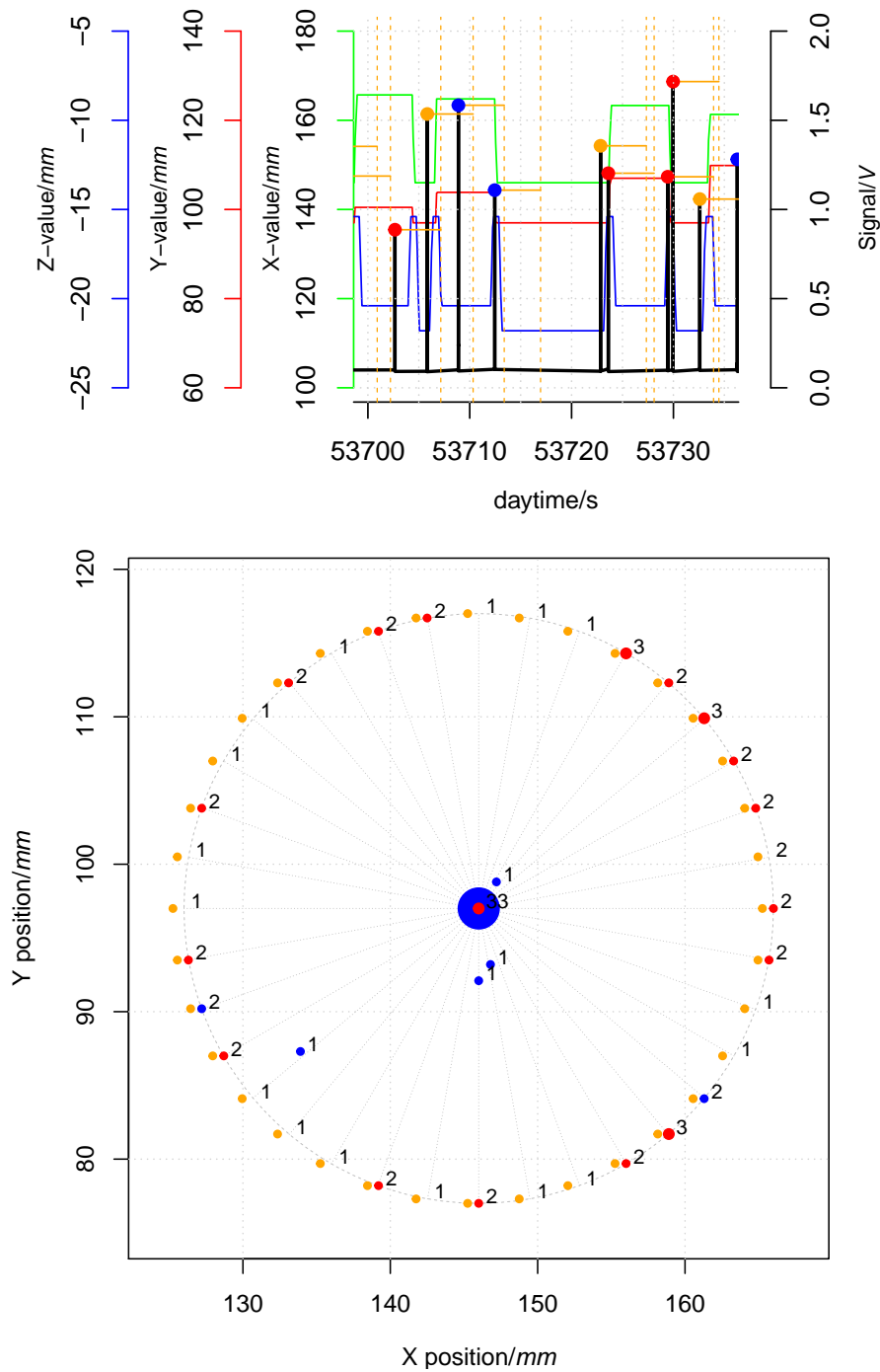
Figure 42: Representation of deposited droplets according to their time and associated X-, Y-, and Z-positions. A) X,Y and Z coordinates of positioning system synchronised with sensor signals. B) Petri dish like representation with dispensing coordinates and the number of possibly deposited droplets according to signal triggering and delay timing.

Table 6: Results of sorted and deposited droplets out of two different experiments targeting microparticles or *E. coli* producing GFP.

	SORTING AND DISPENSING OF	
CATEGORY	MICROPARTICLES	E. COLI /W GFP
Total amount	.... 288 (100 %)	.... 420 (100 %)
Empty	.... 53 (18.4 %)	.... 71 (17 %)
True sorted	.... 203 (70.5 %)	.... 279 (66 %)
False sorted[1]	.... 15 (5.2 %)	.... 29 (7 %)
Mixed[2]	.... 17 (5.9 %)	.... 44 (10 %)

[1] Positions where only contents of unsorted droplet were found (false positive sorted or satellite droplets containing *E. coli* with mCherry)

[2] Positions where beside positives, also contents of negative droplets were found
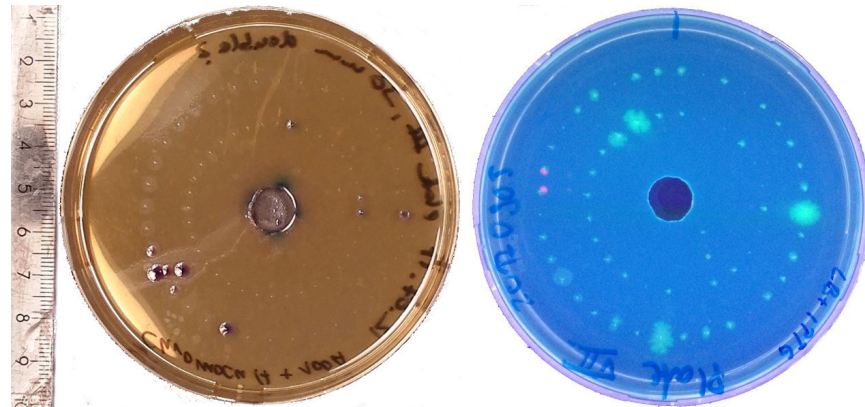
Figure 43: Petri dishes with dispensed droplets. Left: Positions with microparticles and purple-coloured *E. coli* contamination. Right: Positions with *E. coli* expressing GFP and two contaminations of mCherry-producing *E. coli* (pink) under UV-light.

4

DISCUSSION

The here presented work showed a first approach to extract and deposit single picolitre droplets from a microfluidic screening assay on separate target compartments. In that way, classic HTS systems can be replaced with highly efficient microfluidic systems in search of new natural compounds. The obtained results from over one million screened droplets with a rare population of encapsulated microparticles revealed promising performance values of approximately 55 % single deposited picolitre droplets and 45 % with more than one droplet per position. Insignificant better results were obtained for a screening of droplets with a scarce population of *E. coli* producing GFP.

For the realisation of such a process, all developed core components for sorting, transferring, positioning and dispensing had to be precisely adjusted like a clockwork: Every little gear-wheel interlocks with another one in a precise way. Only then it is possible to ensure a literally correct timing. Yet, if one pinion fails, the whole machinery presumably fails. Fortunately, probable emerging issues can be compensated to a certain degree. If, for example, a sudden change in system pressure leads to set value deviations, utilised pumps would use their internal feedback control to adjust the differing pressure automatically. In case of failing sorting electronics, all droplets would be directed towards the waste to not contaminate an active sorting pipeline. The following sections will elucidate more on these core developments and the final validation stage.

4.1 NOVEL SORTING STRUCTURES

Optimised chip and electrode structures such as the afore mentioned wider relaxation zone and bifurcation area as well as pressure-balanced outlets enabled a notably better DEP-based sorting than previous chip generations and were invariably utilised in the final validation experiments. Numerical simulations confirmed the obtained results, even though a realistic two-phase flow simulation as shown in a work of Bashir *et al.* [91] was substituted by a so called particle tracing module in the COMSOL Multiphysics simulation software. This strategy was successfully applied in a work of Piacentini *et al.* [63] that illustrated

theoretically and practically the separation of different-sized blood cells using dielectrophoretic forces—a model applicable to the here examined two-phase droplets.

One core enhancement of all structural changes was the redesign of sorting outlet channels. Based on various published works [36, 44, 45, 81], channel constrictions were initally designed to generate a pressure imbalance that changes the hydrodynamic pressure regime for a controlled droplet selection process. However, diminutive pressure changes can already occur when exchanging setup-related tubings and connectors due to varying length and inner surface condition compared to a fixed channel layout. Hence, outlet channels of new chip generations were kept equal-sized for a fully external control. Contrarily, such structures were also published [66, 70, 71, 92] showing that the ultimate channel design does not exist but rather has to be modelled according to its application.

Additional structural impact on the sorting efficiency was achieved by designing serrated electrodes resulting in an extended and increased electrical field density. As microfluidic DEP-based sorting is basically restricted by the two-dimensional contact surface between electrodes and fluid channels, novel accomplishments in this field are rare. Interestingly, an entirely new approach of Clark *et al.* [93] demonstrated an increased working surface by using concentric electrodes in conjunction with a curved sorting channel around it, making a sorting process even more efficient. However, in case a sorting fails the experimenter has to review dozens of different parameters. A trouble-shooting can therefore be to look for a needle in a haystack. Despite meticulous planning and years of experience, droplet sorting remains a challenging undertaking. Recently, Tran *et al.* [94] described a first approach to overcome this issue by automating workflows using already available commercial fluid-handling robots. There, even complex microfluidic processes, including sorting, can be executed without human intervention to increase reliability and convenience.

4.2 DATA MANAGEMENT

The amount of recorded digital data per experiment was adjusted according to droplet size and velocity/frequency using the sampling theorem [95] and predominant technical and experimental possibilities. Since image data were transferred in a raw binary format from the utilized high-speed camera, a fast data storage was required to handle up to 3 GB of data per second. While short-term recording could be realised by an adequate sized virtual RAM (random-access memory/main memory) drive, long-term storage over an entire experimental time (see Section 3.5.1 on page 64) led to restrictions in saving image data—even by applying additional spatial and temporal sampling calculations to estimate the minimum required frame rate

for still motion blur-free images, as described by Puelo [96]. It was a straight forward solution to use a random sample approach over the whole experimental period of time in combination with a camera feature called triggered burst mode.[1] In that way, data could be significantly reduced to an amount that statistically still represented a whole experimental record. Solutions for acquiring complete experimental image data could be the development of a software that handles incoming data in real-time, applies intelligent lossless compression algorithms to gain images of significantly reduced size [97–99] and outputs processed data onto a file storage system. Since image conversion generally requires certain encoding efforts, computational CPU resources could in turn become another limiting factor. In fact, alternative computing sources like graphical processing units can be applied. Originally designed for parallel and fast graphic data processing, this technology is able to handle large amounts of non-graphical data (known as GPGPU—General-purpose computing on graphics processing units) [100].

In contrary, restricted data flow from the utilised positioning system's built-in data logger (10 S/s) led to undersampling. Since the X/Y/Z-axes moved in preassigned ways, data interpolation was applied by manual pattern recognition and data comparison. An additional challenge posed the whole experimental data from the utilised DAQ card that was recorded at a needed sampling rate of 10 kS/s generating a single data set of 1 GB ($\approx$15 min. recording time). A post-analyses required not only special software, but also a considerable amount of main memory ($\approx$4 GB). Unless the utilised computer was equipped with excessive amount of RAM, simultaneous and comparative analyses of other data sets was only feasible by extracting specific subsets and purging unnecessary data in RAM to continue the analysis.

In summary, big data is a nowadays fast developing field in the digital era, since rapid developing technologies enable to acquire, process and store steady growing amounts of data faster than ever. Thus, extracting useful information at the tera- to petabytes scale becomes a real challenge that requires the development of new algorithms for data management as well as methods to understand and assess data in multiple dimensions [101–103].

4.3 AUTOMATED DEVICE CONTROL

Screening of hundreds to thousands of samples per second could only be realised by automating the here presented microfluidic system. Information flow from a droplet to and between developed device was realised by A/D conversion into TTL-compatible logic levels by the

---

1 Burst mode: One trigger event initiates an automatic recording of an image sequence rather than recording a single frame, a.k.a. single shot.

assembly of a Schmitt-trigger based comparator circuit. Due to its ubiquitous availability, the TTL standard was not only selected for wide range applicability purpose but also for future compatibility. Furthermore, in comparison to the CMOS logic family that is used to build microprocessors and other digital logic circuits, TTL components draw less power at high switching frequencies, are less susceptible to damage from electrostatic discharge and have easier design rules [104, 105]. Performance related issues between those two families can be neglected, since standard microfluidic application do not work at megahertz to gigahertz scale.

Prevalent personal computers (PC) were considered unfeasible for an automation approach, even being fast digital logic devices that are built on the aforementioned technologies. The reason for this is the operating system architecture consisting of multiple layers to maintain and control installed hardware and software-related communication. As a result, experimental signals cannot be processed in real time, but experience a significant delay. Solutions for this can either be found using special software [106], a real-time operating system [107] or a hardware-based approach called FPGA². The latter one requires knowledge on a special hardware description language (HDL) to be configured, resulting in high capital costs. A promising and inexpensive technology that can be found in smartphones and embedded devices are so called reduced instruction set computers (RISC). Compared to classic CISC approaches like the nowadays widespread x86 architecture, these microprocessor types demand less transistors, hence generating less heat but can still operate at considerable high computational speed [108, 109]. Current development platforms like the Arduino exclusively rely on these types of technology, which were subsequently applied in this work as a faster and more flexible approach to process experimental signals for a reliable automation.

4.4 SYSTEM PERFORMANCE

4.4.1 Performance of optical components

Label-free droplets of down to 15 µm diameter could be detected with the here developed low-cost refraction-based sensor. This was accomplished by utilising a small laser-LED, an ultra-compact LED-driver and an additive manufactured housing. Raytracing simulations and the comparison with a commercial fluid sensor proofed its unique capability to detect picolitre droplets with the observed signal progression and detection limit. However, acquired performance values are moderate when being compared to an optical microscope with a maximum resolution of 0.2 µm. Future improvements should therefore include the use of optics for enhanced beam shaping (collimation, focussing). To keep the sensor design compact, these need

---

2 Field-programmable gate array

to be capable of being integrated into the fibre mount. A solution can be so-called gradient-index (GRIN) lenses [110]) insertable into a fibre light beam using ferrule sleeves. In addition, a reference beam could be installed in conjunction with a second photodetector and a log-ratio-amplifier to significantly lower system related noise (light source, ambient temperature, detector and post-detection and digitization [111, 112])—a technology that is used by default in photometers [113]. Furthermore, utilising a light source with shorter wavelength (towards the high-energy UV range) would theoretically also lower the diffraction-limited LOD. But considering the fact that droplets carry biological samples, this strategy is not advisable.

4.4.2 Depositing performance analyses

The throughput of the here developed system amounts to $\approx 170\,\text{mHz}$—a result of various factors. One accounts to the utilised positioning system and its inherent movement capabilities. Another significant impact has the applied positioning strategy that, in turn, is related to the target matrix (Section 3.4.5). The integration of an IDC interrupt during an active depositing can be a way to speed-up the system. The positioning script would then alter the default return path at a detected IDC occurrence and immediately locate a proximate dispensing location. Another way can be to limit Z-movements to a minimum. This would increase the risk of cross contaminations, as a certain safe distance between capillary exit and agar medium surface can not be guaranteed anymore. A derived strategy can therefore be to completely eliminate the Z-axis, as already shown by Jiang *et al.* [114]. There, single droplets were continuously dispensed on streak plates in a spiral fashion. Yet, this approach has certain disadvantages as it is supposed to not run in a discontinuous fashion with a continuous flow of carrier fluid. At high flow rates and low spiral movement, carrier fluid would flood the Petri dish. The minimum angular velocity therefore limits the total depositing rate and time. An alternative, yet similar approach was developed by Küster *et al.* who built a laser-modified matrix with micrometer-sized hydrophilic spots and a hydrophobic surrounding [65]. This enabled a steady droplet dispensing across the surface excluding a Z-movement at $4\,\text{Hz}$, but relies heavily on almost reproducible occurring droplets. Bai *et al.* proposed a system to couple microfluidics with a commercial cell sorter (FACS) having an additional dispensing module [72], thereby completely avoiding a complex microfluidic depositing approach. This strategy, however, has some major disadvantages. It requires size-constricted gelated droplets that needs to be temperature-controlled and, most important, disrupt many of the possible standard droplet operations. In addition, expensive and sensitive equipment like microwell plates, a cell sorter and custom-made nozzles are needed. Problematic gelated droplets were bypassed by Zinchenko

et al. who presented a system using water-oil-water double-emulsion droplets coupled to a cell-sorter unit [115]. Though, that system heavily constricts the applied droplet diameter for use in cell sorter-based depositing. Moreover, it is doubtful whether single droplet depositing is reliable, particularly in samples of small size and low amount [116]. In addition, no evident data is yet available if double-emulsion droplets can maintain a reliable cultivation of microorganisms [117] over days or weeks, as shown in Mahler *et al.* [61]. This is a decisive parameter for future microbial screenings.

4.5 DOI MANAGEMENT

All normal-sized droplets (*i. e.* no satellites) located inside the CWI are supposed to be DOIs. However, those who appear between two depositing steps are defined as IDCs. These are wanted, however, false positioned DOIs that significantly contributed to over 40 % of positions with more than one statistically assumed droplet (type II, Section 3.4.6 on page 59). A reason for the occurrence of IDCs can be the sorting of two DOIs in a time lower than t_p—a rather uncontrollable randomly occurring event—or a diminishing of the interdroplet distance during its transfer from chip to target. The latter got addressed during the CWI development to ensure a steady and defined droplet transportation for a guaranteed single droplet depositing.

4.5.1 Droplet distance control

Interdroplet distances inside the CWI were kept steady in a passive way by various factors: 1) By adjusting the droplet-to-capillary diameter ratio, 2) by a minimised use of transitions and 3) by tubing surface-based friction. Buoyancy-related distance decrements was not investigated further as it is a hardly controllable factor that is inclusive to the utilised fluids. Similar issues and developed strategies can be seen in a recent work of Cole *et al.* [118] using a chip-integrated capillary. This approach makes a distance control more robust than the here used flexible CWI but significantly less flexible since it is fixed to a specific chip. Furthermore, an interdroplet distance is only assured over a length of 10 mm, while the here developed CWI presents a droplet transfer over 800 mm.

An active way of handling droplet distances could be realised by digital microfluidics (DMF). There, sorted DOIs might be temporarily parked on a typical DMF chip-array [119, 120], controlled via a software, and also released into the CWI pipeline based on a preset delay time. A lately published work of Li *et al.* [121] showed a promising and inexpensive approach to easily handle large DMF arrays, similar to controlling electrodes of a flatscreen matrix. Further solutions for handling IDCs can be found upstream at the sorting site by diminishing the total droplet sorting rate or by selecting a more

restrictive sorting criterion. The latter is usually the case in many ultrahigh-throughput screening experiments. Strategies for handling downstream appearing IDCs can be the modification of the positioning route (see Section 4.4.2 on page 75) and the introduction of a real-time droplet velocity monitor by a second sensor unit mounted beneath the first one. This would enable a more dynamic droplet depositing control by actively feeding back actual speed values to the positioning process control. Hence, the actual delay time can be optimised and combined with a second delay as mentioned above. In contrast, necessary droplet velocity measurements are already performed on-chip (Section 3.2.4) but are strongly altered inside the CWI capillary. Thus, another option would be to maximal shorten the transfer route. This is currently limited due to hardware dimensions of microscope and positioning system. The above mentioned work of Cole *et al.* presented a very similar concept that overcomes this issue by placing a microfluidic chip including sorting functions directly on a positioning stage [118]. Yet, limited sorting capabilities as well as the need for a special high-voltage dispensing target limits its applicability.

4.5.2 Satellite droplets influence depositing

Screening systems require decisive criteria to pick candidates of interest. The here developed sorting unit follows this principle and was used to reliably filter droplets with maximum fluorescent content. Yet, image-based analyses revealed uncontrollable satellite droplet flow at the sorting bifurcation. It is assumed that these significantly accounted for the obtained 5–7 % false-sorted droplets. According to prior performed raytracing simulations the sensor LOD is two times higher than the observed satellite droplets of $\varnothing 15\,\mu m$. It is therefore assumed that droplets of this size did not trigger their own dispensing. This hypothesis can be assured as the trigger threshold level was kept constantly high. The occurrence of satellite droplets prior to a triggered droplet with a velocity lower than initially estimated can be a more realistic explanation of those results. Such events can be minimised in future experimentation by altering the positioning process. Instead of immediately moving the capillary towards the dispensing position, it should remain at the waste for a preset relative second delay time (*e.g.* $t_{d2} = 0.7 t_d$) that effectively shortens the waiting time at the dispensing position. Thus, a reduced number of co-deposited droplets can be realised. Another strategy can be performed by actively removing such unwanted droplets. This can be done either at sorting site via pulsed pressure [122] or at depositing in non-contacting mode by a so-called vacuum-shutter system [123].

Beside the development of certain displacement strategies, it is advantageous to decrease the formation of satellite droplets from the beginning. This implies the understanding of their emergence. One pos-

sible reason could be the production of surfactants by encapsulated microorganisms themselves [124]. This, in turn, results in a reduced interfacial tension between aqueous and oil phase, thereby promoting droplet rupture [67]. The here applied *E. coli* K12 can express an outer membrane protein (OmpA) that is proven to act as an emulsion (de)stabiliser [125]. Yet, the exact impact on this system is unknown and should be investigated in future. Generally, siRNA could be introduced into the medium to transiently knockdown the transcription of genes [126] responsible for the production of surfactants. In a real screening approach, potential surfactant producers can not be selectively treated to minimise satellite droplets. Hence, this method would probably lead to minor impact. The reduction of satellites should therefore focus more on fluid-related procedures, *e. g.* chip structures that passively filter [127, 128] or actively direct satellite droplets towards the negative channel [59, 74].

4.6 SYSTEM SCALABILITY

All developed components of this system were built in a modular way. This allows for a versatile future applicability in commonly used greater nano- and microlitre droplet scales. Sorting geometries might need to be re-evaluated, since 2D-chip proportions do not scale linearly with the targeted volume. Associated DEP-sorting parameters equally necessitate adaptation. With the developed refraction-based droplet sensor inverted and multi-phase systems (oil-in-water/double/triple emulsions) can be applied. The CWI and adaptor mount require only minor adjustments. Yet, inner diameter and transfer length should be revised for hydraulic resistance impact on the applied fluidic system. On the part of hardware, trigger processing capabilities can be assured up to the nanosecond scale, thus easily enabling an ultrahigh-throughput screening of millions of samples per day. Concerning the depositing process, only minor modifications of the positioning script might be necessary, since it was designed to handle almost any target matrix. It can, for example, straightly be used to place selected droplets on a MALDI matrix or streak plate expanding the concept presented by Küster *et al.* [65] and Jiang *et al.* [114], respectively. Regarding the positioning throughput, indicated values of 170 mHz can be increased by major script modifications to at least six times higher values with Z-axis ($\approx$1 Hz) and minimum ten times higher values excluding a Z-movement.

5

CONCLUSION

State-of-the-art robotic liquid handling systems have been the golden standard for high throughput experimentation for several decades despite a large number of disadvantages. Meanwhile, droplet-based microfluidics rapidly evolved to a powerful alternative by means of quantitative and qualitative processing of encapsulated material up to the picolitre volume scale. Inevitably, it became important to link such microscopic operations with large-scale analytics and processing. So far, microfluidic developments focused on droplet generation, modification and sorting but neglected single droplet isolation out of a fluidic system/chip for further processing of valuable hits. This work aimed for the establishment of a chip-to-world interface in conjunction with an automation approach to handle individual picolitre entities with the ultimate goal to screen for unknown natural products:

1. By utilising a microbial screening model, single droplets of interest were automatically isolated from a bulk population via developed fluidic sorting structures at 100 events per second.

2. With a subsequent droplet redirection to addressable locations of a Petri dish, a a fully automated depositing was realised at a frequency of one single droplet every 6 s.

3. Previous encapsulated and cultivated microorganisms of interest were then able to grow to single colony forming units.

4. The required system automation and process control was realised by multiple core developments:

   - A chip-to-world interface enabling a sequential and robust droplet transfer from chip to target via

   - an optical sensor that detects droplets of up to $\varnothing$ 15 μm, so that subsequently

   - a high-speed A/D converter digitises droplet signals to be handled by

   - a dispensing unit and positioning algorithms as well as multiplexed high speed data acquisition software for an adjacent droplet depositing.

5. The developed system provides a simple strategy to interconnect functions at a volume difference higher than five orders of magnitude.

6. This enables its applicability in many fields such as microbiological and natural product research, advanced single cell readouts (combining phenotypic and genotypic analytics) as well as screenings for personalised medicine.

7. With short-term adjustments it is envisioned that this system will provide a reliable and reproducible single droplet depositing with more than 90 % success enabling powerful microfluidic-macroanalytic interfaces.

BIBLIOGRAPHY

[1] M. Wainwright, J. Lederberg and J. Lederberg. 'History of Microbiology'. *Encyclopedia of Microbiology* 2 (1992), 419–437.

[2] D. L. Nelson, A. L. Lehninger and M. M. Cox. *Lehninger Principles of Biochemistry*. Macmillan, 2008.

[3] H. Hahn and S. H. Kaufmann. *Medizinische Mikrobiologie und Infektiologie*. Springer-Verlag, 2006.

[4] E. P. Abraham and E. Chain. 'An enzyme from bacteria able to destroy penicillin'. *Nature* 146 (1940), 837.

[5] M. Demerec. 'Origin of bacterial resistance to antibiotics'. *Journal of Bacteriology* 56 (1948), 63.

[6] L. L. Ling, T. Schneider, A. J. Peoples, A. L. Spoering, I. Engels, B. P. Conlon, A. Mueller, T. F. Schäberle, D. E. Hughes and S. Epstein. 'A new antibiotic kills pathogens without detectable resistance'. *Nature* 517 (2015), 455–459. DOI: 10.1038/nature14098.

[7] H. Seppälä, T. Klaukka, J. Vuopio-Varkila, A. Muotiala, H. Helenius, K. Lager and P. Huovinen. 'The effect of changes in the consumption of macrolide antibiotics on erythromycin resistance in group A streptococci in Finland'. *New England Journal of Medicine* 337 (1997), 441–446. DOI: 10.1056/NEJM199708143370701.

[8] N. Cassir, J.-M. Rolain and P. Brouqui. 'A new strategy to fight antimicrobial resistance: the revival of old antibiotics'. *Frontiers in Microbiology* 5 (2014). DOI: 10.3389/fmicb.2014.00551.

[9] G. Thomas. *WHO's first global report on antibiotic resistance reveals serious, worldwide threat to public health*. 30th Apr. 2014. URL: http://www.who.int/mediacentre/news/releases/2014/amr-report/en/.

[10] J. Berdy. 'Bioactive microbial metabolites'. *The Journal of Antibiotics* 58 (2005), 1–26. DOI: 10.1038/ja.2005.1.

[11] G. W. Tyson and J. F. Banfield. 'Cultivating the uncultivated: a community genomics perspective'. *Trends in Microbiology* 13 (2005), 411–415. DOI: 10.1016/j.tim.2005.07.003.

[12] H. Steininger, G. Schicht, M. Peissker and H. Knöll. 'Das Autoselect-System–ein Automatensystem zur Selektion von Antibiotikaproduzenten. V. Achtfach-Pipettierautomat'. *Engineering in Life Sciences* 1 (1981), 296–299. DOI: 10.1002/abio.370010309.

[13]   L. M. Mayr and P. Fuerst. 'The future of high-throughput screening'. *Journal of Biomolecular Screening* 13 (2008), 443–448. DOI: 10.1177/1087057108319644.

[14]   A. Coates and Y. Hu. 'Novel approaches to developing new antibiotics for bacterial infections'. *British Journal of Pharmacology* 152 (2007), 1147–1154. DOI: 10.1038/sj.bjp.0707432.

[15]   M. A. Fischbach and C. T. Walsh. 'Antibiotics for emerging pathogens'. *Science* 325 (2009), 1089–1093. DOI: 10.1126/science.1176667.

[16]   W. Zheng, N. Thorne and J. C. McKew. 'Phenotypic screens as a renewed approach for drug discovery'. *Drug Discovery Today* 18 (2013), 1067–1073. DOI: 10.1016/j.drudis.2013.07.001.

[17]   T. Beneyton, S. Thomas, A. D. Griffiths, J.-M. Nicaud, A. Drevelle and T. Rossignol. 'Droplet-based microfluidic high-throughput screening of heterologous enzymes secreted by the yeast Yarrowia lipolytica'. *Microbial Cell Factories* 16 (2017), 18. DOI: 10.1186/s12934-017-0629-5.

[18]   G. M. Whitesides. 'The origins and the future of microfluidics'. *Nature* 442 (July 2006), 368–373. ISSN: 1476-4687. DOI: 10.1038/nature05058.

[19]   A. Manz, D. J. Harrison, E. M. Verpoorte, J. C. Fettinger, A. Paulus, H. Lüdi and H. M. Widmer. 'Planar chips technology for miniaturization and integration of separation techniques into monitoring systems: capillary electrophoresis on a chip'. *Journal of Chromatography A* 593 (1992), 253–258. DOI: 10.1016/0021-9673(92)80293-4.

[20]   D. Gerhold, T. Rushmore and C. T. Caskey. 'DNA chips: promising toys have become powerful tools'. *Trends in Biochemical Sciences* 24 (1999), 168–173. DOI: 10.1016/S0968-0004(99)01382-1.

[21]   S. Schumacher, J. Nestler, T. Otto, M. Wegener, E. Ehrentreich-Förster, D. Michel, K. Wunderlich, S. Palzer, K. Sohn and A. Weber. 'Highly-integrated lab-on-chip system for point-of-care multiparameter analysis'. *Lab on a Chip* 12 (2012), 464–473. DOI: 10.1039/c1lc20693a.

[22]   P. S. Dittrich and A. Manz. 'Lab-on-a-chip: microfluidics in drug discovery'. *Nature Reviews Drug Discovery* 5 (Mar. 2006), 210–218. ISSN: 1474-1784. DOI: 10.1038/nrd1985.

[23]   C. Wiles and P. Watts. 'Recent advances in micro reaction technology'. *Chemical Communications* 47 (2011), 6512. ISSN: 1364-548X. DOI: 10.1039/c1cc00089f.

[24]   C.-C. Chang, L.-M. Fu and R.-J. Yang. 'Active Mixer'. *Encyclopedia of Microfluidics and Nanofluidics*. Springer, 2015, 40–47.

[25] Y. T. Atalay, S. Vermeir, D. Witters, N. Vergauwe, B. Verbruggen, P. Verboven, B. M. Nicolaï and J. Lammertyn. 'Microfluidic analytical systems for food analysis'. *Trends in Food Science & Technology* 22 (2011), 386–404. DOI: 10.1016/j.tifs.2011.05.001.

[26] S. Moon, H. O. Keles, A. Ozcan, A. Khademhosseini, E. Hæggstrom, D. Kuritzkes and U. Demirci. 'Integrating microfluidics and lensless imaging for point-of-care testing'. *Biosensors and Bioelectronics* 24 (2009), 3208–3214. DOI: 10.1016/j.bios.2009.03.037.

[27] H. M. Hegab, A. ElMekawy and T. Stakenborg. 'Review of microfluidic microbioreactor technology for high-throughput submerged microbiological cultivation'. *Biomicrofluidics* 7 (Mar. 2013), 021502. ISSN: 1932-1058. DOI: 10.1063/1.4799966.

[28] S.-Y. Teh, R. Lin, L.-H. Hung and A. P. Lee. 'Droplet microfluidics'. *Lab on a Chip* 8 (2008), 198–220. DOI: 10.1039/b715524g.

[29] M. A. Unger, H.-P. Chou, T. Thorsen, A. Scherer and S. R. Quake. 'Monolithic microfabricated valves and pumps by multilayer soft lithography'. *Science* 288 (2000), 113–116. DOI: 10.1126/science.288.5463.113.

[30] D. C. Duffy, J. C. McDonald, O. J. Schueller and G. M. Whitesides. 'Rapid prototyping of microfluidic systems in poly (dimethylsiloxane)'. *Analytical Chemistry* 70 (1998), 4974–4984. DOI: 10.1021/ac980656z.

[31] J.-C. Baret. 'Surfactants in droplet-based microfluidics'. *Lab on a Chip* 12 (2012), 422–433. DOI: 10.1039/c1lc20582j.

[32] A. R. Abate, T. Hung, R. A. Sperling, P. Mary, A. Rotem, J. J. Agresti, M. A. Weiner and D. A. Weitz. 'DNA sequence analysis with droplet-based microfluidics'. *Lab on a Chip* 13 (2013), 4864–4869. DOI: 10.1039/c3lc50905b.

[33] E. Fradet, P. Abbyad, M. H. Vos and C. N. Baroud. 'Parallel measurements of reaction kinetics using ultralow-volumes'. *Lab on a Chip* 13 (2013), 4326–4330. DOI: 10.1039/c3lc50768h.

[34] J. Cao, L. Hafermann and J. M. Köhler. 'Stochastically reduced communities—Microfluidic compartments as model and investigation tool for soil microorganism growth in structured spaces'. *Engineering in Life Sciences* 17 (2017), 792–800. DOI: 10.1002/elsc.201600264.

[35] S. Cho, D.-K. Kang, S. Sim, F. Geier, J.-Y. Kim, X. Niu, J. B. Edel, S.-I. Chang, R. C. Wootton and K. S. Elvira. 'Droplet-based microfluidic platform for high-throughput, multi-parameter screening of photosensitizer activity'. *Analytical Chemistry* 85 (2013), 8866–8872. DOI: 10.1021/ac4022067.

[36] B. El Debs, R. Utharala, I. V. Balyasnikova, A. D. Griffiths and
      C. A. Merten. 'Functional single-cell hybridoma screening us-
      ing droplet-based microfluidics'. *Proceedings of the National Aca-
      demy of Sciences* 109 (2012), 11570–11575. DOI: 10.1073/pnas.
      1204514109.

[37] T. P. Lagus and J. F. Edd. 'High throughput single-cell and
      multiple-cell micro-encapsulation'. *Journal of Visualized Experi-
      ments: JoVE* (2012). DOI: 10.3791/4096.

[38] S. N. Bhatia and D. E. Ingber. 'Microfluidic organs-on-chips'.
      Nature Biotechnology 32 (2014), 760–772. DOI: 10.1038/nbt.
      2989.

[39] J. R. Coppeta, M. J. Mescher, B. C. Isenberg, A. J. Spencer,
      E. S. Kim, A. R. Lever, T. J. Mulhern, R. Prantil-Baun, J. C.
      Comolli and J. T. Borenstein. 'A portable and reconfigurable
      multi-organ platform for drug development with onboard mi-
      crofluidic flow control.' *Lab on a Chip* 17 (2016), 134–144. ISSN:
      1473-0189. DOI: 10.1039/c6lc01236a.

[40] J. Yang, Z. Chen, P. Ching, Q. Shi and X. Li. 'An integrated mi-
      crofluidic platform for evaluating in vivo antimicrobial activ-
      ity of natural compounds using a whole-animal infection model.'
      Lab on a Chip 13 (2013), 3373–3382. ISSN: 1473-0189. DOI: 10.
      1039/c3lc50264c.

[41] J. J. Agresti, E. Antipov, A. R. Abate, K. Ahn, A. C. Rowat,
      J.-C. Baret, M. Marquez, A. M. Klibanov, A. D. Griffiths and
      D. A. Weitz. 'Ultrahigh-throughput screening in drop-based
      microfluidics for directed evolution'. *Proceedings of the National
      Academy of Sciences* 107 (2010), 4004–4009. DOI: 10.1073/pnas.
      0910781107.

[42] T. C. Scanlon, S. M. Dostal and K. E. Griswold. 'A high-through-
      put screen for antibiotic drug discovery.' *Biotechnology and Bioen-
      gineering* 111 (2014), 232–243. ISSN: 1097-0290. DOI: 10.1002/
      bit.25019.

[43] X. Liu, R. Painter, K. Enesa, D. Holmes, G. Whyte, C. Garlisi, F.
      Monsma, M. Rehak, F. Craig and C. Smith. 'High-throughput
      screening of antibiotic-resistant bacteria in picodroplets'. *Lab
      on a Chip* 16 (2016), 1636–1643. DOI: 10.1039/c6lc00180g.

[44] L. Mazutis, J. Gilbert, W. L. Ung, D. A. Weitz, A. D. Grif-
      fiths and J. A. Heyman. 'Single-cell analysis and sorting using
      droplet-based microfluidics.' *Nature Protocols* 8 (2013), 870–891.
      ISSN: 1750-2799. DOI: 10.1038/nprot.2013.046.

[45] T. Beneyton, I. P. M. Wijaya, P. Postros, M. Najah, P. Leblond,
      A. Couvent, E. Mayot, A. D. Griffiths and A. Drevelle. 'High-
      throughput screening of filamentous fungi using nanoliter-range

droplet-based microfluidics'. *Scientific Reports* 6 (2016), 27223. DOI: 10.1038/srep27223.

[46] P. A. Romero, T. M. Tran and A. R. Abate. 'Dissecting enzyme function with microfluidic-based deep mutational scanning'. *Proceedings of the National Academy of Sciences* 112 (2015), 7159–7164. DOI: 10.1073/pnas.1422285112.

[47] B. M. Paegel and G. F. Joyce. 'Microfluidic compartmentalized directed evolution'. *Chemistry & Biology* 17 (2010), 717–724. DOI: 10.1016/j.chembiol.2010.05.021.

[48] F. Bunge, S. v. d. Driesche and M. J. Vellekoop. 'Microfluidic Platform for the Long-Term On-Chip Cultivation of Mammalian Cells for Lab-On-A-Chip Applications.' *Sensors (Basel, Switzerland)* 17 (2017). ISSN: 1424-8220. DOI: 10.3390/s17071603.

[49] J. Cao, D. Kürsten, K. Krause, E. Kothe, K. Martin, M. Roth and J. M. Köhler. 'Application of micro-segmented flow for two-dimensional characterization of the combinatorial effect of zinc and copper ions on metal-tolerant Streptomyces strains'. *Applied Microbiology & Biotechnology* 97 (2013), 8923–8930. DOI: 10.1007/s00253-013-5147-8.

[50] K. Martin, T. Henkel, V. Baier, A. Grodrian, T. Schön, M. Roth, J. M. Köhler and J. Metze. 'Generation of larger numbers of separated microbial populations by cultivation in segmented-flow microdevices'. *Lab on a Chip* 3 (2003), 202–207. DOI: 10.1039/b301258c.

[51] M. Tehranirokh, A. Z. Kouzani, P. S. Francis and J. R. Kanwar. 'Microfluidic devices for cell cultivation and proliferation.' *Biomicrofluidics* 7 (2013), 51502. ISSN: 1932-1058. DOI: 10.1063/1.4826935.

[52] K. Zengler, G. Toledo, M. Rappé, J. Elkins, E. J. Mathur, J. M. Short and M. Keller. 'Cultivating the uncultured'. *Proceedings of the National Academy of Sciences* 99 (2002), 15681–15686. DOI: 10.1073pnas.252630999.

[53] D. J. Collins, A. Neild, A.-Q. Liu, Y. Ai et al. 'The Poisson distribution and beyond: methods for microfluidic droplet production and single cell encapsulation'. *Lab on a Chip* 15 (2015), 3439–3459. DOI: 10.1039/c5lc00614g.

[54] T. Henkel, T. Bermig, M. Kielpinski, A. Grodrian, J. Metze and J. Köhler. 'Chip modules for generation and manipulation of fluid segments for micro serial flow processes'. *Chemical Engineering Journal* 101 (2004), 439–445. DOI: 10.1016/j.cej.2004.01.021.

[55] G. Christopher, J. Bergstein, N. End, M. Poon, C. Nguyen and S. L. Anna. 'Coalescence and splitting of confined droplets at microfluidic junctions'. *Lab on a Chip* 9 (2009), 1102–1109. DOI: 10.1039/b813062k.

[56] W.-H. Tan and S. Takeuchi. 'Timing controllable electrofusion device for aqueous droplet-based microreactors.' *Lab on a Chip* 6 (2006), 757–763. ISSN: 1473-0197. DOI: 10.1039/b517178d.

[57] A. R. Abate, T. Hung, P. Mary, J. J. Agresti and D. A. Weitz. 'High-throughput injection with microfluidics using picoinjectors'. *Proceedings of the National Academy of Sciences* 107 (2010), 19163–19166. DOI: 10.1073/pnas.1006888107.

[58] M. Mizuno, M. Yamada, R. Mitamura, K. Ike, K. Toyama and M. Seki. 'Magnetophoresis-integrated hydrodynamic filtration system for size-and surface marker-based two-dimensional cell sorting'. *Analytical Chemistry* 85 (2013), 7666–7673. DOI: 10.1021/ac303336f.

[59] A. Sciambi and A. R. Abate. 'Accurate microfluidic sorting of droplets at 30 kHz.' *Lab on a Chip* 15 (Jan. 2015), 47–51. ISSN: 1473-0189. DOI: 10.1039/c4lc01194e.

[60] E. Zang, S. Brandes, M. Tovar, K. Martin, F. Mech, P. Horbert, T. Henkel, M. T. Figge and M. Roth. 'Real-time image processing for label-free enrichment of Actinobacteria cultivated in picolitre droplets.' *Lab on a Chip* 13 (Sept. 2013), 3707–3713. ISSN: 1473-0189. DOI: 10.1039/c3lc50572c.

[61] L. Mahler, M. Tovar, T. Weber, S. Brandes, M. M. Rudolph, J. Ehgartner, T. Mayr, M. T. Figge, M. Roth and E. Zang. 'Enhanced and homogeneous oxygen availability during incubation of microfluidic droplets'. *RSC Advances* 5 (2015), 101871–101878. DOI: 10.1039/c5ra20118g.

[62] G. J. Sussman and G. L. Steele. 'Scheme: A interpreter for extended lambda calculus'. *Higher-Order and Symbolic Computation* 11 (1998), 405–439.

[63] N. Piacentini, G. Mernier, R. Tornay and P. Renaud. 'Separation of platelets from other blood cells in continuous-flow by dielectrophoresis field-flow-fractionation'. *Biomicrofluidics* 5 (2011), 034122. DOI: 10.1063/1.3640045.

[64] R Core Team. *R: A Language and Environment for Statistical Computing*. R Foundation for Statistical Computing. Vienna, Austria, 2017. URL: https://www.R-project.org.

[65] S. K. Küster, S. R. Fagerer, P. E. Verboket, K. Eyer, K. Jefimovs, R. Zenobi and P. S. Dittrich. 'Interfacing Droplet Microfluidics with Matrix-Assisted Laser Desorption/Ionization Mass Spectrometry: Label-Free Content Analysis of Single Droplets'. *Ana-*

lytical Chemistry 85 (2013). PMID: 23289755, 1285–1289. DOI:
`10.1021/ac3033189`.

[66] K. Ahn, C. Kerbage, T. P. Hunt, R. Westervelt, D. R. Link and
      D. Weitz. 'Dielectrophoretic manipulation of drops for high-
      speed microfluidic sorting devices'. *Applied Physics Letters* 88
      (2006), 024104. DOI: `10.1063/1.2164911`.

[67] J.-C. Baret, O. J. Miller, V. Taly, M. Ryckelynck, A. El-Harrak,
      L. Frenz, C. Rick, M. L. Samuels, J. B. Hutchison, J. J. Agresti,
      D. R. Link, D. A. Weitz and A. D. Griffiths. 'Fluorescence-
      activated droplet sorting (FADS): efficient microfluidic cell sort-
      ing based on enzymatic activity.' *Lab on a Chip* 9 (July 2009),
      1850–1858. ISSN: 1473-0197. DOI: `10.1039/b902504a`.

[68] H.-D. Xi, H. Zheng, W. Guo, A. M. Ganan-Calvo, Y. Ai, C.-W.
      Tsao, J. Zhou, W. Li, Y. Huang, N.-T. Nguyen and S. H. Tan.
      'Active droplet sorting in microfluidics: a review'. *Lab on a Chip*
      17 (2017), 751–771. DOI: `10.1039/C6LC01435F`.

[69] D. R. Gossett, W. M. Weaver, A. J. Mach, S. C. Hur, H. T. K.
      Tse, W. Lee, H. Amini and D. Di Carlo. 'Label-free cell separa-
      tion and sorting in microfluidic systems'. *Analytical and Bioana-
      lytical Chemistry* 397 (Aug. 2010), 3249–3267. ISSN: 1618-2650.
      DOI: `10.1007/s00216-010-3721-9`.

[70] F. Guo, X.-H. Ji, K. Liu, R.-X. He, L.-B. Zhao, Z.-X. Guo, W. Liu,
      S.-S. Guo and X.-Z. Zhao. 'Droplet electric separator micro-
      fluidic device for cell sorting'. *Applied Physics Letters* 96 (2010),
      193701. DOI: `10.1063/1.3360812`.

[71] S. W. Lim, T. M. Tran and A. R. Abate. 'PCR-activated cell
      sorting for cultivation-free enrichment and sequencing of rare
      microbes'. *PloS one* 10 (2015), e0113549. DOI: `10.1371/journal.`
      `pone.0113549.g001`.

[72] Y. Bai, E. Weibull, H. N. Joensson and H. Andersson-Svahn.
      'Interfacing picoliter droplet microfluidics with addressable
      microliter compartments using fluorescence activated cell sort-
      ing'. *Sensors and Actuators B: Chemical* 194 (2014), 249–254. ISSN:
      0925-4005. DOI: `10.1016/j.snb.2013.12.089`.

[73] R. Seemann, M. Brinkmann, T. Pfohl and S. Herminghaus.
      'Droplet based microfluidics'. *Reports on Progress in Physics* 75
      (2012), 016601. URL: `http://stacks.iop.org/0034-4885/75/`
      `i=1/a=016601`.

[74] D. Frenzel and C. A. Merten. 'Microfluidic train station: highly
      robust and multiplexable sorting of droplets on electric rails'.
      Lab on a Chip 17 (2017), 1024–1030. DOI: `10.1039/c6lc01544a`.

[75] *A chemically inert multichannel chip-to-world interface to connect
      microfluidic chips.* Vol. 8976. 2014, 89760E1–89760E6. DOI: `10.`
      `1117/12.2044660`.

[76]   K. W. Oh, C. Park, K. Namkoong, J. Kim, K.-S. Ock, S. Kim, Y.-A. Kim, Y.-K. Cho and C. Ko. 'World-to-chip microfluidic interface with built-in valves for multichamber chip-based PCR assays'. *Lab on a Chip* 5 (2005), 845–850. DOI: 10.1039/B503437J.

[77]   T. N. Ackermann, P. Gimenez-Gomez, X. Munoz-Berbel and A. Llobera. 'Plug and measure—a chip-to-world interface for photonic lab-on-a-chip applications'. *Lab on a Chip* 16 (2016), 3220–3226. DOI: 10.1039/C6LC00462H.

[78]   H. Bruus. *Theoretical microfluidics*. Oxford university press Oxford, 27th Sept. 2007, 368. ISBN: 9780199235094.

[79]   J. Schindelin, I. Arganda-Carreras, E. Frise, V. Kaynig, M. Longair, T. Pietzsch, S. Preibisch, C. Rueden, S. Saalfeld, B. Schmid, J.-Y. Tinevez, D. J. White, V. Hartenstein, K. Eliceiri, P. Tomancak and A. Cardona. 'Fiji: an open-source platform for biological-image analysis.' *Nature Methods* 9 (June 2012), 676–682. ISSN: 1548-7105. DOI: 10.1038/nmeth.2019.

[80]   B. Cahill, S. Wiedemeier and G. Gastrock. 'Measurement of droplet impedance in segmented flow'. *5. Miniaturisierte analytische Verfahren*. AMA. 2013, 276–278. ISBN: 978-3-9813484-5-3. DOI: 10.5162/11dss2013/E4.

[81]   F. Gielen, R. Hours, S. Emond, M. Fischlechner, U. Schell and F. Hollfelder. 'Ultrahigh-throughput-directed enzyme evolution by absorbance-activated droplet sorting (AADS).' *Proceedings of the National Academy of Sciences of the United States of America* 113 (Nov. 2016), E7383–E7389. ISSN: 1091-6490. DOI: 10.1073/pnas.1606927113.

[82]   J. H. Jung, K. H. Lee, K. S. Lee, B. H. Ha, Y. S. Oh and H. J. Sung. 'Optical separation of droplets on a microfluidic platform'. *Microfluidics and Nanofluidics* 16 (2014), 635–644. ISSN: 1613-4990. DOI: 10.1007/s10404-013-1263-0.

[83]   R. Gao, N. Choi, S.-I. Chang, S. H. Kang, J. M. Song, S. I. Cho, D. W. Lim and J. Choo. 'Highly sensitive trace analysis of paraquat using a surface-enhanced Raman scattering micro-droplet sensor.' *Analytica Chimica Acta* 681 (Nov. 2010), 87–91. ISSN: 1873-4324. DOI: 10.1016/j.aca.2010.09.036.

[84]   A. S. Basu. 'Droplet morphometry and velocimetry (DMV): a video processing software for time-resolved, label-free tracking of droplet parameters'. *Lab on a Chip* 13 (2013), 1892. ISSN: 1473-0189. DOI: 10.1039/c3lc50074h.

[85]   P. A. G. Butler, B. Mills and P. C. Hauser. 'Capillary Electrophoresis Detector Using a Light Emitting Diode and Optical Fibres'. *The Analyst* 122 (1997), 949–953. ISSN: 1364-5528. DOI: 10.1039/a703413j.

[86]   V. Trivedi, A. Doshi, G. K. Kurup, E. Ereifej, P. J. Vandevord and A. S. Basu. 'A modular approach for the generation, storage, mixing, and detection of droplet libraries for high-throughput screening'. *Lab on a Chip* 10 (2010), 2433. ISSN: 1473-0189. DOI: 10.1039/c004768f.

[87]   H. Kodama. 'Automatic method for fabricating a three-dimensional plastic model with photo-hardening polymer'. *Review of Scientific Instruments* 52 (Nov. 1981), 1770–1773. ISSN: 1089-7623. DOI: 10.1063/1.1136492.

[88]   M. Griot. *Introduction to Laser Technology*. Tech. rep. CVI Melles Griot, June 2009.

[89]   O. H. Schmitt. 'A thermionic trigger'. *Journal of Scientific Instruments* 15 (1938), 24. URL: http://stacks.iop.org/0950-7671/15/i=1/a=305.

[90]   L. W. Nagel and O. Enterprises. 'The life of SPICE'. *Bipolar Circuits and Technology Meeting*. 1996.

[91]   S. Bashir, J. M. Rees and W. B. Zimmerman. 'Simulations of microfluidic droplet formation using the two-phase level set method'. *Chemical Engineering Science* 66 (2011), 4733–4741. ISSN: 0009-2509. DOI: 10.1016/j.ces.2011.06.034.

[92]   O. Jakobsson, C. Grenvall, M. Nordin, M. Evander and T. Laurell. 'Acoustic actuated fluorescence activated sorting of microparticles'. *Lab on a Chip* 14 (2014), 1943–1950. DOI: 10.1039/C3LC51408K.

[93]   I. C. Clark, R. Thakur and A. R. Abate. 'Concentric electrodes improve microfluidic droplet sorting'. *Lab on a Chip* 18 (2018), 710–713. DOI: 10.1039/C7LC01242J.

[94]   T. M. Tran, S. C. Kim and A. R. Abate. 'Robotic automation of droplet microfluidics'. *bioRxiv* (2018). DOI: 10.1101/278556.

[95]   H. D. Luke. 'The origins of the sampling theorem'. *IEEE Communications Magazine* 37 (1999), 106–108. ISSN: 0163-6804. DOI: 10.1109/35.755459.

[96]   B. Pueo. 'High speed cameras for motion analysis in sports science'. *Journal of Human Sport and Exercise* 11 (2016), 53–73. DOI: 10.14198/jhse.2016.111.05.

[97]   A. H. Robinson and C. Cherry. 'Results of a prototype television bandwidth compression scheme'. *Proceedings of the IEEE* 55 (Mar. 1967), 356–364. ISSN: 0018-9219. DOI: 10.1109/PROC.1967.5493.

[98]   H. Sanchez-Cruz and R. M. Rodriguez-Dagnino. 'Compressing bilevel images by means of a three-bit chain code'. *Optical Engineering* 44 (2005), 1–8. DOI: 10.1117/1.2052793.

[99]   J. H. Pujar and L. M. Kadlaskar. 'A New Lossless Method of Image Compression and Decompression Using Huffman Coding Techniques'. 2010.

[100]   D. M. Chitty. 'A data parallel approach to genetic programming using programmable graphics hardware'. *GECCO*. 2007, 1566–1573. DOI: 10.1145/1276958.1277274.

[101]   S. Li, S. Dragicevic, F. A. Castro, M. Sester, S. Winter, A. Coltekin, C. Pettit, B. Jiang, J. Haworth, A. Stein and T. Cheng. 'Geospatial big data handling theory and methods: A review and research challenges'. *ISPRS Journal of Photogrammetry and Remote Sensing* 115 (2016). Theme issue 'State-of-the-art in photogrammetry, remote sensing and spatial information science', 119–133. ISSN: 0924-2716. DOI: 10.1016/j.isprsjprs.2015.10.012.

[102]   J.-G. Lee and M. Kang. 'Geospatial Big Data: Challenges and Opportunities'. *Big Data Research* 2 (2015). Visions on Big Data, 74–81. ISSN: 2214-5796. DOI: 10.1016/j.bdr.2015.01.003.

[103]   A. Dasgupta. *Big data: The future is in analytics*. 17th Apr. 2018. URL: https://www.geospatialworld.net/article/big-data-the-future-is-in-analytics/.

[104]   P. Horowitz. *The art of electronics*. 2nd ed. Cambridge University Press, 1989. ISBN: 9780521370950. DOI: 10.2277/0521370957.

[105]   F. Semiconductor. *CMOS, the ideal Logic Family*. Tech. rep. ON Semiconductor, 1983, 12. URL: https://www.fairchildsemi.com/application-notes/AN/AN-77.pdf.

[106]   R. Angstadt, J. Estrada, H. T. Diehl, B. Flaugher and M. Johnson. 'Microsecond Delays on Non-Real Time Operating Systems'. *2007 15th IEEE-NPSS Real-Time Conference*. IEEE, Apr. 2007. DOI: 10.1109/rtc.2007.4382803.

[107]   N. V. Satyanarayana, R. Mall and A. Pal. 'A layered architecture for real-time systems'. *Microprocessors and Microsystems* 20 (1996), 241–250. ISSN: 0141-9331. DOI: 10.1016/0141-9331(96)01087-3.

[108]   F. Masood. *RISC and CISC. Computer Architecture*. Tech. rep. National university of sciences and technology, 2011, 21. URL: https://arxiv.org/ftp/arxiv/papers/1101/1101.5364.pdf.

[109]   D. A. Patterson and C. H. Sequin. 'RISC I: A Reduced Instruction Set VLSI Computer'. *25 Years of the International Symposia on Computer Architecture (Selected Papers)*. ISCA '98. Barcelona, Spain: ACM, 1998, 216–230. ISBN: 1-58113-058-9. DOI: 10.1145/285930.285981.

[110] A. B. Tsiboulia. *Encyclopedia of Optical Engineering: Abe-Las*. Ed. by R. G. Drigger. Dekker Encyclopedias Series. Marcel Dekker, 2003. ISBN: 9780824742508. URL: `https://books.google.de/books?id=kxICp6t-CDAC`.

[111] P. Hauser. 'A multi-wavelength photometer based on light-emitting diodes'. *Talanta* 42 (Apr. 1995), 605–612. DOI: `10.1016/0039-9140(95)01455-k`.

[112] Newport. *Optical detection systems. Technical Note*. Newport. 2018. URL: `https://www.newport.com/n/optical-detection-systems`.

[113] H.-H. Perkampus. *Spektroskopie*. 1993. ISBN: 3-527-28303-X.

[114] C.-Y. Jiang, L. Dong, J.-K. Zhao, X. Hu, C. Shen, Y. Qiao, X. Zhang, Y. Wang, R. F. Ismagilov and S.-J. Liu. 'High-throughput single-cell cultivation on microfluidic streak plates'. *Applied and Environmental Microbiology* 82 (2016), 2210–2218. DOI: `10.1128/AEM.03588-15`.

[115] A. Zinchenko, S. R. Devenish, B. Kintses, P.-Y. Colin, M. Fischlechner and F. Hollfelder. 'One in a million: flow cytometric sorting of single cell-lysate assays in monodisperse picolitre double emulsion droplets for directed evolution'. *Analytical Chemistry* 86 (2014), 2526–2533. DOI: `10.1021/ac403585p`.

[116] A. Gross, J. Schoendube, S. Zimmermann, M. Steeb, R. Zengerle and P. Koltay. 'Technologies for Single-Cell Isolation'. *International journal of molecular sciences* 16 (2015), 16897–16919. DOI: `10.3390/ijms160816897`.

[117] C. B. Chang, J. N. Wilking, S.-H. Kim, H. C. Shum and D. A. Weitz. 'Monodisperse emulsion drop microenvironments for bacterial biofilm growth'. *Small* 11 (2015), 3954–3961. DOI: `10.1002/smll.201403125`.

[118] R. H. Cole, S.-Y. Tang, C. A. Siltanen, P. Shahi, J. Q. Zhang, S. Poust, Z. J. Gartner and A. R. Abate. 'Printed droplet microfluidics for on demand dispensing of picoliter droplets and cells'. *Proceedings of the National Academy of Sciences* 114 (2017), 8728–8733. DOI: `10.1073/pnas.1704020114`.

[119] K. Choi, A. H. Ng, R. Fobel and A. R. Wheeler. 'Digital Microfluidics'. *Annual Review of Analytical Chemistry* 5 (2012). PMID: 22524226, 413–440. DOI: `10.1146/annurev-anchem-062011-143028`.

[120] E. Samiei, M. Tabrizian and M. Hoorfar. 'A review of digital microfluidics as portable platforms for lab-on a-chip applications'. *Lab on a Chip* 16 (2016), 2376–2396. DOI: `10.1039/C6LC00387G`.

[121] C. Li, K. Zhang, X. Wang, J. Zhang, H. Liu and J. Zhou. 'Feedback control system for large scale 2D digital microfluidic platforms'. *Sensors and Actuators B: Chemical* 255 (2018), 3616–3622. ISSN: 0925-4005. DOI: 10.1016/j.snb.2017.09.071.

[122] Z. Cao, F. Chen, N. Bao, H. He, P. Xu, S. Jana, S. Jung, H. Lian and C. Lu. 'Droplet sorting based on the number of encapsulated particles using a solenoid valve.' *Lab on a Chip* 13 (Jan. 2013), 171–178. ISSN: 1473-0189. DOI: 10.1039/c2lc40950j.

[123] J. Riba, T. Gleichmann, S. Zimmermann, R. Zengerle and P. Koltay. 'Label-free isolation and deposition of single bacterial cells from heterogeneous samples for clonal culturing'. *Scientific Reports* 6 (2016), 32837. DOI: 10.1038/srep32837.

[124] J. D. Desai and I. M. Banat. 'Microbial production of surfactants and their commercial potential.' *Microbiology and Molecular Biology Reviews : MMBR* 61 (Mar. 1997), 47–64. ISSN: 1092-2172.

[125] S. M. A. Segura, A. P. Macías, D. C. Pinto, W. L. Vargas, M. J. Vives-Florez, H. E. C. Barrera, O. A. Álvarez and A. F. G. Barrios. 'Escherichia coli's OmpA as Biosurfactant for Cosmetic Industry: Stability Analysis and Experimental Validation Based on Molecular Simulations'. *Advances in Computational Biology* (1st Jan. 2014). DOI: 10.1007/978-3-319-01568-2_38.

[126] M. Matzke, A. J. Matzke and J. M. Kooter. 'RNA: guiding gene silencing'. *Science* 293 (2001), 1080–1083. DOI: 10.1126/science.1063051.

[127] R. Ding, W. L. Ung, J. A. Heyman and D. A. Weitz. 'Sensitive and predictable separation of microfluidic droplets by size using in-line passive filter'. *Biomicrofluidics* 11 (2017), 014114. DOI: 10.1063/1.4976723.

[128] D. Hyun Yoon, S. Numakunai, A. Nakahara, T. Sekiguchi and S. Shoji. 'Hydrodynamic on-rail droplet pass filter for fully passive sorting of droplet-phase samples'. *RSC Advances* 4 (2014), 37721–37725. DOI: 10.1039/C4RA08354G.

APPENDIX
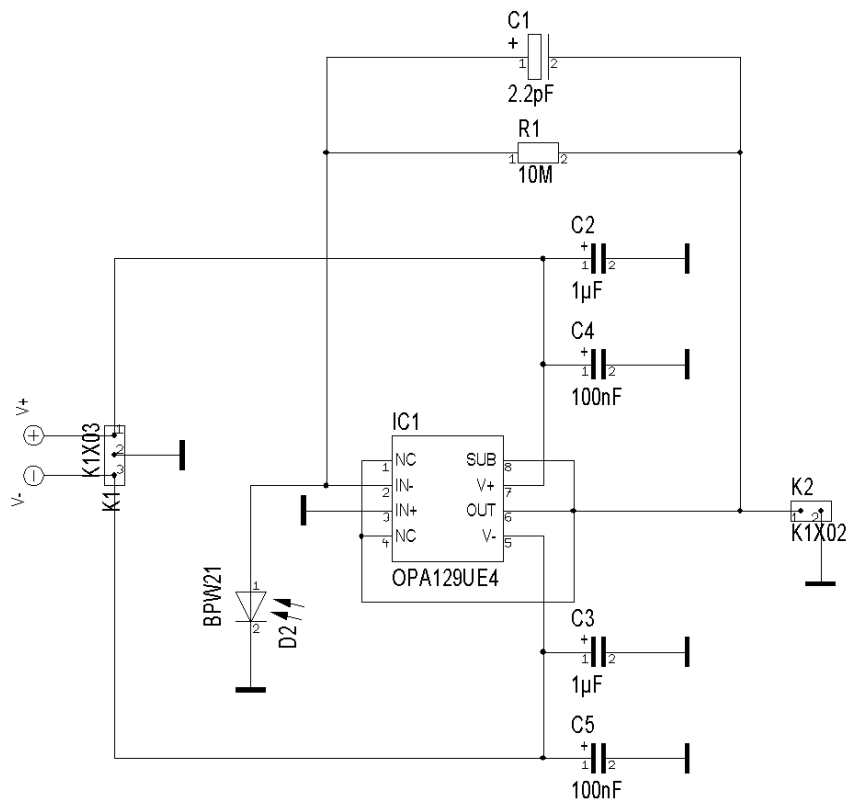
Figure 44: Photodetector circuit with silicon photodiode BPW 21 and transimpedance amplifier OPA 129 UE 4.
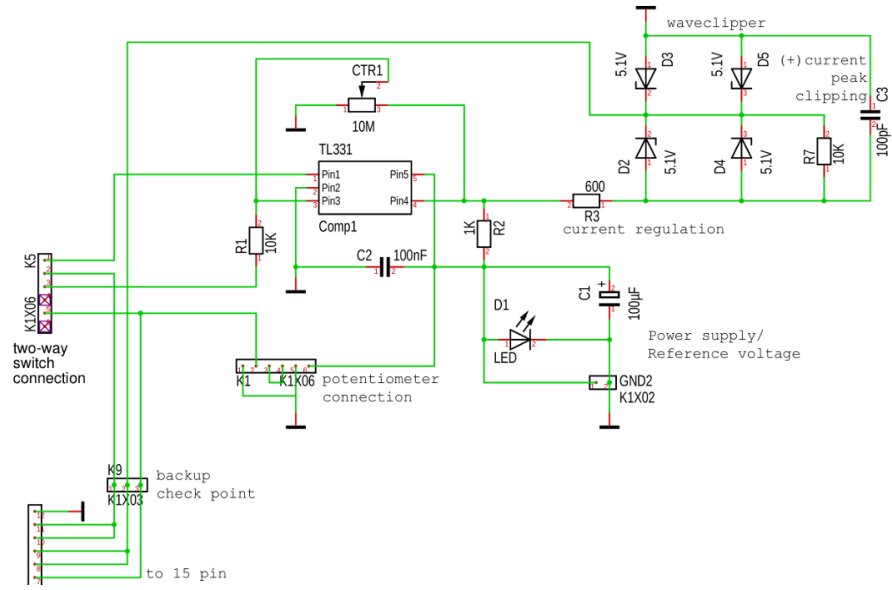
Figure 45: Schmitt-trigger circuit including a single differential comparator TL331, a reference/hysteresis adjustment as well as TTL conform signal output and inverting/non-inverting switchable states.

Table 7: Components of photodetector circuitry

Component	Manufacturer	Value
Photodetector part list		
Silicon Photodiode	Osram	BPW21
Transimpedance amplifier	Texas Instruments	OPA129UE4
Aluminium Housing	Deltron	459-0150
Metal resistor	TE Connectivity	YR1B1K0CC, $1\,k\Omega$
Metal resistor	Vishay Dale	PTF5610K000-BYEB, $10\,k\Omega$
Capacitor	Kemet	$2.2\,pF$
Ceramic capacitor	Holey Stone	X7R, $100\,nF$
Ceramic capacitor	muRata	$1\,\mu F$
Subminiature plug/jack	Binder	99 0075 100 03, 3 pin
SMA connector, male	Amphenol	RSMA6411A1-3GT50G
Amplifier part list		
Instrumentation Amp	Burr-Brown	PGA204/205
Inductor, dual	Würth Elektronik	744272472, $4700\,\mu H$
Inductor, single	muRata	RLB0712-100KL, $10\,\mu H$
Multi-Turn Trimmer	Vishay Spectrol	43 series, $500\,k\Omega$
SMD resistor	TE Connectivity	$100\,k\Omega$
Dip switch	NKK	On-On
SMD Ceramic capacitor	Yageo Phycomp	CC0805KRX-7R7BB104, $100\,nF$
Ceramic capacitor	Kemet	C320C474-M5U5TA, $470\,nF$
Ceramic capacitor	muRata	$1\,\mu F$
Aluminium capacitor	Panasonic	16SEPC100M, $100\,\mu F$
DC/DC power supply	Traco	TEN3-0522, $\pm 12\,V$

Table 8: Components of Schmitt trigger and valve controller

COMPONENT	MANUFACTURER	VALUE
Schmitt trigger part list		
Comparator	. . . Texas Instruments	. . . . TL-331
Housing	. . . . Hammond	. . . . 1455L1201, aluminium
Metal resistor	. . . . . TE Connectivity	. . YR1B1K0CC, 1 kΩ
Metal resistor	. . . . Vishay Dale	. . . . PTF5610K000-BYEB, 10 kΩ
Trimmer potentiometer	. . . . . TE Connectivity	CB10LV106N, 10 MΩ
Precision potentiometer	. . . . Bourns	. . . . 3590S, 10 kΩ
Precision control knob	. . . . . Vishay Spectrol	. . 11A11B10, 10 turns
Zener diode	. . On Semiconductor	. . MMBZ5231BLT1G, 5.1 V
Ceramic capacitor	. . . . Multicomp	. . . MC0805N101J500-A2.54MM, 100 pF
Ceramic capacitor	. . . . Holy Stone	. . . . X7R, 100 nF
Aluminium capacitor	. . . . Panasonic	16SEPC100M, 100 µF
D-SUB connector, female	. . . . Harting	. . . . . . 09 67 015 4701, 15-pin
D-SUB backshell	. . . . Harting	. . . . . . 09 67 015 0442, 15-pin
DPDT Slide switch	. . . . Multicomp	. . . . Miniature DPCO
Valve controller part list		
Relay board	Conrad Components	. . . . 197720 12 V/DC
High power resistor	. . . . . . BI technologies	. . . . BPC 5 (5 W)
Power supply	. . . . LSE Intl.	. . . . . LSE 9901 B 1260
BNC jack	. . . . Molex Corp.	. . . . . 50 Ω, solder tag
Solenoid valve	. . . . Sirai Srl	. . . . S104-12/S305
Valve connector	. . . . Binder	. . . . 43 1930 004 03
Housing	. . . . Takachi	. . . . PF20-6-20W

Listing 2: Excerpt of refined C-code for FPGA counting-based droplet sorting (based on [60]). A camera-based FPGA was interfaced and repurposed to count droplets in real-time. When reaching a preset threshold of detected events (here: 100), a DAQ-card (Section 2.6 on page 11) was used to output a digital TTL-signal that ultimately triggers the HVA.

```
1   FGStartDevice(hCamera);
2   while(Result == FCE_NOERROR && !kbhit())
3     {
4      do{
5          FGFRAME Frame;
6          Result=FGGetFrame(hCamera,&Frame,1000);
7        if(Result == FCE_NOERROR) {
8              Result=FGPutFrame(hCamera,&Frame);
9              i++;
10             if(i==100){
11                // TTL signal output
12                cbDBitOut(BoardNum,PortNum,BitNum,1);
13                cbDBitOut(BoardNum,PortNum,BitNum,0);
14                 i = 0;
15                }
16        }
17        if(Result == FCE_NOERROR){
18              Result = FGPutFrame(hCamera,&Frame);
19            }
20        } while ( Frame.Flags != FGF_LAST && !kbhit() );
21    }
22   FGStopDevice(hCamera);
```

Listing 3: Developed scheme code to simulate a refraction-based sensor by moving a droplet inside a capillary

```
1    (define movdropncap
2      (lambda ( )

4        (define iSt 1 )
5        (define iFi 50 )
6        (define iIn 0.5 )
7        (define jSt 0 )
8        (define jFi 200 )
9        (define jIn 1 )
10       (define step 1 )
11       (define port (open-input-output-file "dai1_100.txt"))

13       (do ((i iSt (+ i iIn)))
14         ((= i iFi) i)

16         (display "Changing sphere diameter +1")(newline)
17         (edit:clear-selection)
18         (edit:add-selection (entity:get-by-name "droplet"))
19         (modify:sphere (entity:get-by-name "droplet") i)
20         (display "Shifting objects +1 ")(newline)
21         (edit:move (list
22                     (entity:get-by-name "capillary")
23                     (entity:get-by-name "oil")
24                     (entity:get-by-name "coating")
25                     (entity:get-by-name "droplet")
26                     ) step 0 0
27           #f #t )
28         (display "Moving sphere to start")(newline)
29         (edit:clear-selection)
30         (edit:add-selection (entity:get-by-name "droplet"))
31         (edit:move (list
```

```
32              (entity:get-by-name "droplet")
33              ) 0 -100 0
34        #f #t) ; relative moving
35      (do ((j jSt (+ j jIn)))
36        ((= j jFi) j)
37        (display "Position ")(display j)
38        (display ", Round ")(display i)(newline)
39        (raytrace:all-sources)
40        (edit:clear-selection)
41        (edit:add-selection (tools:face-in-body 1 (entity:get-by-name "
              detector")))
42        (display "Getting irradiance info")(newline)
43        (print (analysis:get-current-irradiance-average) port)
44        (display "Moving droplet +1")(newline)
45        (edit:clear-selection)
46        (edit:add-selection (entity:get-by-name "droplet"))
47        (edit:move (list
48              (entity:get-by-name "droplet")
49              ) 0 step 0
50        #f #t ) ; end edit sphere move and raytrace
51      ) ; end do j
52    ) ; end do i
53    (close-output-port port)
54    )
55  )
```

Listing 4: R-code to estimate positions of dispensed droplets using recorded data sets of the sensor and positioning system.

```
1  # define delaytime sensing/positioning
2  delaytime = 4.5
3  # calculate some necessary vars for next petri dish plot
4  # xw/yw = x and y waste position
5  diameter <- round((max(possignal$neMAXYS1_X..Actual.Position,na.rm=TRUE)-min(
       possignal
7  $neMAXYS1_X..Actual.Position,na.rm=TRUE)))
8  xw = round(max(possignal$neMAXYS1_X..Actual.Position,na.rm=TRUE)-(diameter/2))
9  yw = round(max(possignal$neMAXYS1_Y..Actual.Position,na.rm=TRUE)-(diameter/2))
10 zw = round(min(possignal$neMAXYS1_Z..Actual.Position),2)
11 zmax = round(max(possignal$neMAXYS1_Z..Actual.Position),1)
12 # z value of dispensing (agar surface)
13 zdisp = -19.5
14 # coordinates of a horizontal line through waste
15 xgrid<-c(min(possignal$neMAXYS1_X..Actual.Position,na.rm=TRUE),max(possignal
17 $neMAXYS1_X..Actual.Position,na.rm=TRUE))
18 ygrid<-c(yw,yw)
20 # create empty data frames
21 peakset = data.frame()
22 peakset.triggered = data.frame()
23 peakset.triggered.timed = data.frame()
24 arrowlist <- data.frame()
25 # x, y and z values short before droplet trigger
26 xval0 <- vector('numeric')
27 yval0 <- vector('numeric')
28 zval0 <- vector('numeric')
29 # x, y and z values at droplet trigger
30 xval <- vector('numeric')
31 yval <- vector('numeric')
32 zval <- vector('numeric')
33 # x, y and z values short after droplet trigger
34 xval1 <- vector('numeric')
35 yval1 <- vector('numeric')
```

```r
36  zval1 <- vector('numeric')
37  # x, y and z values after delay time
38  xval2 <- vector('numeric')
39  yval2 <- vector('numeric')
40  zval2 <- vector('numeric')
41  # z value short after delay time
42  zval3 <- vector('numeric')
43  # z value short before delay time
44  zval4 <- vector('numeric')

46  for (i in 1:nrow(peak.listb)) {
47    # extract x, y and z data shortly before drop detection
48    peaktime0 <- peak.listb$daytime[i]
49    peaktime0 <- peaktime0 - 0.1
50    smallset0 <- subset(possignal1,
51                        daytime2 > peaktime0 - .1
52                        &
53                        daytime2 < peaktime0 + .1,
54                        select=c

56  ("neMAXYS1_X..Actual.Position","neMAXYS1_Y..Actual.Position","neMAXYS1_Z..
         Actual.Positio

58  n"))
59    xmean0<- round(mean(smallset0$neMAXYS1_X..Actual.Position,na.rm = TRUE),1)
60    ymean0<- round(mean(smallset0$neMAXYS1_Y..Actual.Position,na.rm = TRUE),1)
61    zmean0<- round(mean(smallset0$neMAXYS1_Z..Actual.Position,na.rm = TRUE),2)
62    xval0 <- append(xval0,xmean0)
63    yval0 <- append(yval0,ymean0)
64    zval0 <- append(zval0,zmean0)

66    # extract x, y and z data at droplet trigger
67    # and add certain +- time to bypass sampling limitations
68    smallset <- subset(possignal1,
69                       daytime2 > peak.listb$daytime[i] - .15
70                       &
71                       daytime2 < peak.listb$daytime[i] + .15,
72                       select=c

74  ("neMAXYS1_X..Actual.Position","neMAXYS1_Y..Actual.Position","neMAXYS1_Z..
         Actual.Positio

76  n"))
77    xmean<- round(mean(smallset$neMAXYS1_X..Actual.Position,na.rm = TRUE),1)
78    ymean<- round(mean(smallset$neMAXYS1_Y..Actual.Position,na.rm = TRUE),1)
79    zmean<- round(mean(smallset$neMAXYS1_Z..Actual.Position,na.rm = TRUE),2)
80    xval <- append(xval,xmean)
81    yval <- append(yval,ymean)
82    zval <- append(zval,zmean)

84    # extract x, y and z data shortly after drop detection
85    # z-axis needs 400-900 ms to reach max position
86    # x and y waste values stay const until 700 ms
87    peaktime1 <- peak.listb$daytime[i]
88    peaktime1 <- peaktime1 + 0.85
89    smallset1 <- subset(possignal1,
90                        daytime2 > peaktime1 - .125
91                        &
92                          daytime2 < peaktime1 + .125,
93                        select=c

95  ("neMAXYS1_X..Actual.Position","neMAXYS1_Y..Actual.Position","neMAXYS1_Z..
         Actual.Positio

97  n"))
98    xmean1<- round(mean(smallset1$neMAXYS1_X..Actual.Position,na.rm = TRUE),1)
```

```r
 99    ymean1<- round(mean(smallset1$neMAXYS1_Y..Actual.Position,na.rm = TRUE),1)
100    zmean1<- round(mean(smallset1$neMAXYS1_Z..Actual.Position,na.rm = TRUE),2)
101    xval1 <- append(xval1,xmean1)
102    yval1 <- append(yval1,ymean1)
103    zval1 <- append(zval1,zmean1)

105    # extract x, y and z data after delay time
106    peaktime2 <- peak.listb$daytime[i]
107    peaktime2 <- peaktime2 + delaytime
108    smallset2 <- subset(possignal1,
109                        daytime2 > peaktime2 - .15
110                        &
111                        daytime2 < peaktime2 + .15,
112                        select=c

114 ("neMAXYS1_X..Actual.Position","neMAXYS1_Y..Actual.Position","neMAXYS1_Z..
        Actual.Positio

116 n"))
117    xmean2<- round(mean(smallset2$neMAXYS1_X..Actual.Position,na.rm = TRUE),1)
118    ymean2<- round(mean(smallset2$neMAXYS1_Y..Actual.Position,na.rm = TRUE),1)
119    zmean2<- round(mean(smallset2$neMAXYS1_Z..Actual.Position,na.rm = TRUE),2)
120    xval2 <- append(xval2,xmean2)
121    yval2 <- append(yval2,ymean2)
122    zval2 <- append(zval2,zmean2)
123 }
124 # convert to data frames
125 xval0<-as.data.frame(xval0)
126 yval0<-as.data.frame(yval0)
127 zval0<-as.data.frame(zval0)
128 xval<-as.data.frame(xval)
129 yval<-as.data.frame(yval)
130 zval<-as.data.frame(zval)
131 xval1<-as.data.frame(xval1)
132 yval1<-as.data.frame(yval1)
133 zval1<-as.data.frame(zval1)
134 xval2<-as.data.frame(xval2)
135 yval2<-as.data.frame(yval2)
136 zval2<-as.data.frame(zval2)

138 # put everything in the arrowlist frame
139 arrowlist <- cbind(peak.listb$daytime,peak.listb$height,
140                    peak.listb$interpeakdistance2.c,
141                    xval0,yval0,zval0,
142                    xval,yval,zval,
143                    xval1,yval1,zval1,
144                    xval2,yval2,zval2)
145 colnames(arrowlist)<-c("daytime","height","ipd",
146                        "xvalo","yvalo","zvalo",
147                        "xval","yval","zval",
148                        "xval1","yval1","zval1",
149                        "xval2","yval2","zval2")

151 for (i in 1:nrow(arrowlist)) {
152   ifelse(arrowlist$xval[i]==xw  & # waste pos x
153          arrowlist$yval[i]==yw  & # waste pos y
154          arrowlist$zval[i]==zw  & # waste pos z
155          #arrowlist$zval0[i]==zw & # near left z ramp? exclude false positives
156          arrowlist$zval2[i]==zdisp & # disp pos z, after 4.5 sec
157          arrowlist$zval1[i]==zmax & # z-peak right of triggered peak
158          # check if nIDC are near to each other (interpeakdistance)
159          # if yes, define one as nIDC and others as IDC
160          # exclude first droplet with "NA" interpeakdistance
161          (arrowlist$ipd[i] > mean(samplingtime)*2000 |
162           is.na(arrowlist$ipd[i]) == TRUE),
163          arrowlist[i,16]<-"FALSE", # no interdroplet candidate
```

```
164          arrowlist[i,16]<-"TRUE" # idc
165          )
166 }
167 arrowlist.idc<-subset(arrowlist, arrowlist[,16]=="TRUE")
168 arrowlist.nidc<-subset(arrowlist, arrowlist[,16]=="FALSE")

170 # shortest waste waiting time approx 0.4 s
171 # z-move up and down takes approx 1.1 s
172 for (i in 1:nrow(arrowlist.idc)) {
173   # get z-values for right ramp
174   peaktime3 <- arrowlist.idc$daytime[i]
175   peaktime3 <- peaktime3 + (delaytime+0.3)
176   smallset3 <- subset(possignal1,
177                    daytime2 > peaktime3 - 0.1
178                    &
179                    daytime2 < peaktime3 + 0.1,
180                    select = c("neMAXYS1_Z..Actual.Position"))
181   zmean3<- round(mean(smallset3$neMAXYS1_Z..Actual.Position,na.rm = TRUE),2)
182   zval3 <- append(zval3,zmean3)
183   # get z-values for left ramp
184   peaktime4 <- arrowlist.idc$daytime[i]
185   peaktime4 <- peaktime4 + (delaytime - 1.25)
186   smallset4 <- subset(possignal1,
187                    daytime2 > peaktime4 - 0.1
188                    &
189                    daytime2 < peaktime4 + 0.1,
190                    select = c("neMAXYS1_Z..Actual.Position"))
191   zmean4<- round(mean(smallset4$neMAXYS1_Z..Actual.Position,na.rm = TRUE),2)
192   zval4 <- append(zval4,zmean4)
193   }
194 zval4<-as.data.frame(zval4)
195 arrowlist.idc<-cbind(arrowlist.idc,zval3,zval4)

197 # check if z-value before or after exit
198 # fits to z-waste or z-disp value
199 for (i in 1:nrow(arrowlist.idc)) {
200     ifelse(
201            arrowlist.idc$zval2[i]!=zdisp & # disp pos z after 4.5 sec
202            (
203            arrowlist.idc$zval2[i] ==zw |  # waste pos z after 4.5 sec
204            arrowlist.idc$zval3[i] ==zw |  # condition at ramp right
205            arrowlist.idc$zval4[i] ==zdisp
206            ),
207            arrowlist.idc[i,19]<-"TRUE", # droplet to waste
208            arrowlist.idc[i,19]<-"FALSE" #
209            )
210     }
211 arrowlist.idcw<-subset(arrowlist.idc, arrowlist.idc[,19]=="TRUE")
212 arrowlist.idcnow<-subset(arrowlist.idc, arrowlist.idc[,19]=="FALSE")
```

Listing 5: XML-based code for circular droplet depositing including a user-based input dialogue, camera recording, logging and a status monitor. Code was generated using QmixElements 2017.

```
1 <?xml version="1.0" encoding="UTF-8" standalone="yes" ?>
2 <!DOCTYPE boost_serialization>
3 <boost_serialization signature="serialization::archive" version="14">
4 <FunctionSequence class_id="0" tracking_level="1" version="4" object_id="_0">
5   <IScriptFunction class_id="1" tracking_level="0" version="2">
6     <Comment class_id="2" tracking_level="0" version="0"></Comment>
7     <Caption></Caption>
8   </IScriptFunction>
9   <ParallelSequence>0</ParallelSequence>
10  <LinkedFile></LinkedFile>
11  <FunctionCount>37</FunctionCount>
```

```
12    <FunctionType>Create Variable</FunctionType>
13    <Function class_id="3" class_name="QtLabb::Script::CSetVariableFunction"
            tracking_level="1" version="1" object_id="_1">
14      <IScriptFunction>
15        <Comment></Comment>
16        <Caption></Caption>
17      </IScriptFunction>
18      <VariableName>$loops</VariableName>
19      <VariableType>double</VariableType>
20      <VariableValue>0</VariableValue>
21      <CreateVariable>1</CreateVariable>
22    </Function>
23    <FunctionType>Create Variable</FunctionType>
24    <Function class_id_reference="3" object_id="_2">
25      <IScriptFunction>
26        <Comment></Comment>
27        <Caption></Caption>
28      </IScriptFunction>
29      <VariableName>$loopstotal</VariableName>
30      <VariableType>double</VariableType>
31      <VariableValue>0</VariableValue>
32      <CreateVariable>1</CreateVariable>
33    </Function>
34    <FunctionType>Create Variable</FunctionType>
35    <Function class_id_reference="3" object_id="_3">
36      <IScriptFunction>
37        <Comment></Comment>
38        <Caption></Caption>
39      </IScriptFunction>
40      <VariableName>$xdef</VariableName>
41      <VariableType>double</VariableType>
42      <VariableValue>0</VariableValue>
43      <CreateVariable>1</CreateVariable>
44    </Function>
45    <FunctionType>Create Variable</FunctionType>
46    <Function class_id_reference="3" object_id="_4">
47      <IScriptFunction>
48        <Comment></Comment>
49        <Caption></Caption>
50      </IScriptFunction>
51      <VariableName>$ydef</VariableName>
52      <VariableType>double</VariableType>
53      <VariableValue>0</VariableValue>
54      <CreateVariable>1</CreateVariable>
55    </Function>
56    <FunctionType>Create Variable</FunctionType>
57    <Function class_id_reference="3" object_id="_5">
58      <IScriptFunction>
59        <Comment></Comment>
60        <Caption></Caption>
61      </IScriptFunction>
62      <VariableName>$pitch</VariableName>
63      <VariableType>double</VariableType>
64      <VariableValue>0</VariableValue>
65      <CreateVariable>1</CreateVariable>
66    </Function>
67    <FunctionType>Create Variable</FunctionType>
68    <Function class_id_reference="3" object_id="_6">
69      <IScriptFunction>
70        <Comment></Comment>
71        <Caption></Caption>
72      </IScriptFunction>
73      <VariableName>$angle</VariableName>
74      <VariableType>double</VariableType>
75      <VariableValue>0</VariableValue>
76      <CreateVariable>1</CreateVariable>
```

```
 77 |  </Function>
 78 |  <FunctionType>Create Variable</FunctionType>
 79 |  <Function class_id_reference="3" object_id="_7">
 80 |    <IScriptFunction>
 81 |      <Comment></Comment>
 82 |      <Caption></Caption>
 83 |    </IScriptFunction>
 84 |    <VariableName>$r</VariableName>
 85 |    <VariableType>double</VariableType>
 86 |    <VariableValue>0</VariableValue>
 87 |    <CreateVariable>1</CreateVariable>
 88 |  </Function>
 89 |  <FunctionType>Create Variable</FunctionType>
 90 |  <Function class_id_reference="3" object_id="_8">
 91 |    <IScriptFunction>
 92 |      <Comment></Comment>
 93 |      <Caption></Caption>
 94 |    </IScriptFunction>
 95 |    <VariableName>$PI</VariableName>
 96 |    <VariableType>double</VariableType>
 97 |    <VariableValue>3.141592654</VariableValue>
 98 |    <CreateVariable>1</CreateVariable>
 99 |  </Function>
100 |  <FunctionType>Create Variable</FunctionType>
101 |  <Function class_id_reference="3" object_id="_9">
102 |    <IScriptFunction>
103 |      <Comment></Comment>
104 |      <Caption></Caption>
105 |    </IScriptFunction>
106 |    <VariableName>$stepZ</VariableName>
107 |    <VariableType>double</VariableType>
108 |    <VariableValue>0</VariableValue>
109 |    <CreateVariable>1</CreateVariable>
110 |  </Function>
111 |  <FunctionType>Create Variable</FunctionType>
112 |  <Function class_id_reference="3" object_id="_10">
113 |    <IScriptFunction>
114 |      <Comment></Comment>
115 |      <Caption></Caption>
116 |    </IScriptFunction>
117 |    <VariableName>$u</VariableName>
118 |    <VariableType>double</VariableType>
119 |    <VariableValue>0</VariableValue>
120 |    <CreateVariable>1</CreateVariable>
121 |  </Function>
122 |  <FunctionType>Create Variable</FunctionType>
123 |  <Function class_id_reference="3" object_id="_11">
124 |    <IScriptFunction>
125 |      <Comment></Comment>
126 |      <Caption></Caption>
127 |    </IScriptFunction>
128 |    <VariableName>$v</VariableName>
129 |    <VariableType>double</VariableType>
130 |    <VariableValue>0</VariableValue>
131 |    <CreateVariable>1</CreateVariable>
132 |  </Function>
133 |  <FunctionType>Create Variable</FunctionType>
134 |  <Function class_id_reference="3" object_id="_12">
135 |    <IScriptFunction>
136 |      <Comment></Comment>
137 |      <Caption></Caption>
138 |    </IScriptFunction>
139 |    <VariableName>$z</VariableName>
140 |    <VariableType>double</VariableType>
141 |    <VariableValue>0</VariableValue>
142 |    <CreateVariable>1</CreateVariable>
```

```
143    </Function>
144    <FunctionType>Create Variable</FunctionType>
145    <Function class_id_reference="3" object_id="_13">
146      <IScriptFunction>
147        <Comment></Comment>
148        <Caption></Caption>
149      </IScriptFunction>
150      <VariableName>$wait</VariableName>
151      <VariableType>double</VariableType>
152      <VariableValue>0</VariableValue>
153      <CreateVariable>1</CreateVariable>
154    </Function>
155    <FunctionType>Create Variable</FunctionType>
156    <Function class_id_reference="3" object_id="_14">
157      <IScriptFunction>
158        <Comment></Comment>
159        <Caption></Caption>
160      </IScriptFunction>
161      <VariableName>$lowestzwaste</VariableName>
162      <VariableType>double</VariableType>
163      <VariableValue>0</VariableValue>
164      <CreateVariable>1</CreateVariable>
165    </Function>
166    <FunctionType>Create Variable</FunctionType>
167    <Function class_id_reference="3" object_id="_15">
168      <IScriptFunction>
169        <Comment></Comment>
170        <Caption></Caption>
171      </IScriptFunction>
172      <VariableName>$zdiff</VariableName>
173      <VariableType>double</VariableType>
174      <VariableValue>0</VariableValue>
175      <CreateVariable>1</CreateVariable>
176    </Function>
177    <FunctionType>Create Variable</FunctionType>
178    <Function class_id_reference="3" object_id="_16">
179      <IScriptFunction>
180        <Comment></Comment>
181        <Caption></Caption>
182      </IScriptFunction>
183      <VariableName>$speed</VariableName>
184      <VariableType>double</VariableType>
185      <VariableValue>200</VariableValue>
186      <CreateVariable>1</CreateVariable>
187    </Function>
188    <FunctionType>User Input</FunctionType>
189    <Function class_id="4" class_name="QtLabb::Script::CUserInputFunction"
             tracking_level="1" version="0" object_id="_17">
190      <IScriptFunction>
191        <Comment></Comment>
192        <Caption>Radius of circle (in mm)</Caption>
193      </IScriptFunction>
194      <LabelText>Radius of circle (in mm):</LabelText>
195      <VariableName>$r</VariableName>
196      <InputType>double</InputType>
197    </Function>
198    <FunctionType>User Input</FunctionType>
199    <Function class_id_reference="4" object_id="_18">
200      <IScriptFunction>
201        <Comment></Comment>
202        <Caption>z-pitch (in mm)</Caption>
203      </IScriptFunction>
204      <LabelText>z-pitch (in mm):</LabelText>
205      <VariableName>$stepZ</VariableName>
206      <InputType>double</InputType>
207    </Function>
```

```
208    <FunctionType>User Input</FunctionType>
209    <Function class_id_reference="4" object_id="_19">
210      <IScriptFunction>
211        <Comment></Comment>
212        <Caption>Angle Pitch (in mm)</Caption>
213      </IScriptFunction>
214      <LabelText>Angle Pitch (in mm):</LabelText>
215      <VariableName>$pitch</VariableName>
216      <InputType>double</InputType>
217    </Function>
218    <FunctionType>Set Variable</FunctionType>
219    <Function class_id_reference="3" object_id="_20">
220      <IScriptFunction>
221        <Comment></Comment>
222        <Caption></Caption>
223      </IScriptFunction>
224      <VariableName>$loopstotal</VariableName>
225      <VariableType>Calculation</VariableType>
226      <VariableValue>360/$pitch</VariableValue>
227      <CreateVariable>0</CreateVariable>
228    </Function>
229    <FunctionType>User Input</FunctionType>
230    <Function class_id_reference="4" object_id="_21">
231      <IScriptFunction>
232        <Comment></Comment>
233        <Caption>Delay time</Caption>
234      </IScriptFunction>
235      <LabelText>Delay time (s):</LabelText>
236      <VariableName>$wait</VariableName>
237      <InputType>double</InputType>
238    </Function>
239    <FunctionType>User Input</FunctionType>
240    <Function class_id_reference="4" object_id="_22">
241      <IScriptFunction>
242        <Comment></Comment>
243        <Caption>Waste position x</Caption>
244      </IScriptFunction>
245      <LabelText>Waste position x (default center = 95 mm):</LabelText>
246      <VariableName>$xdef</VariableName>
247      <InputType>double</InputType>
248    </Function>
249    <FunctionType>User Input</FunctionType>
250    <Function class_id_reference="4" object_id="_23">
251      <IScriptFunction>
252        <Comment></Comment>
253        <Caption>Waste position y</Caption>
254      </IScriptFunction>
255      <LabelText>Waste position y (default center = 95 mm):</LabelText>
256      <VariableName>$ydef</VariableName>
257      <InputType>double</InputType>
258    </Function>
259    <FunctionType>Move XY</FunctionType>
260    <Function class_id="5" class_name="QtLabb::CMoveToXyScript" tracking_level="
            1" version="1" object_id="_24">
261      <CPositioningDeviceScript class_id="6" tracking_level="0" version="1">
262        <IScriptFunction>
263          <Comment></Comment>
264          <Caption>Waste XY</Caption>
265        </IScriptFunction>
266        <Device>neMAXYS1</Device>
267        <RunToCompletion>1</RunToCompletion>
268      </CPositioningDeviceScript>
269      <TargetPositionX class_id="7" tracking_level="0" version="0">
270        <Data>$xdef</Data>
271      </TargetPositionX>
272      <TargetPositionY>
```

```
273        <Data>$ydef</Data>
274      </TargetPositionY>
275      <Axis1Velocity>
276        <Data>$speed</Data>
277      </Axis1Velocity>
278      <Axis2Velocity>
279        <Data>$speed</Data>
280      </Axis2Velocity>
281    </Function>
282    <FunctionType>User Input</FunctionType>
283    <Function class_id_reference="4" object_id="_25">
284      <IScriptFunction>
285        <Comment></Comment>
286        <Caption>Lowest z-position surface (in mm)</Caption>
287      </IScriptFunction>
288      <LabelText>Lowest z-position surface (in mm):</LabelText>
289      <VariableName>$z</VariableName>
290      <InputType>double</InputType>
291    </Function>
292    <FunctionType>User Input</FunctionType>
293    <Function class_id_reference="4" object_id="_26">
294      <IScriptFunction>
295        <Comment></Comment>
296        <Caption>Lowest z-position Waste (in mm)</Caption>
297      </IScriptFunction>
298      <LabelText>Lowest z-position waste (in mm):</LabelText>
299      <VariableName>$lowestzwaste</VariableName>
300      <InputType>double</InputType>
301    </Function>
302    <FunctionType>Set Variable</FunctionType>
303    <Function class_id_reference="3" object_id="_27">
304      <IScriptFunction>
305        <Comment></Comment>
306        <Caption></Caption>
307      </IScriptFunction>
308      <VariableName>$zdiff</VariableName>
309      <VariableType>Calculation</VariableType>
310      <VariableValue>$z-$lowestzwaste</VariableValue>
311      <CreateVariable>0</CreateVariable>
312    </Function>
313    <FunctionType>Set Variable</FunctionType>
314    <Function class_id_reference="3" object_id="_28">
315      <IScriptFunction>
316        <Comment></Comment>
317        <Caption></Caption>
318      </IScriptFunction>
319      <VariableName>$z</VariableName>
320      <VariableType>Calculation</VariableType>
321      <VariableValue>$z-$zdiff</VariableValue>
322      <CreateVariable>0</CreateVariable>
323    </Function>
324    <FunctionType>Move Z</FunctionType>
325    <Function class_id="8" class_name="QtLabb::CMoveZScript" tracking_level="1"
              version="1" object_id="_29">
326      <CPositioningDeviceScript>
327        <IScriptFunction>
328          <Comment></Comment>
329          <Caption>Waste Z</Caption>
330        </IScriptFunction>
331        <Device>neMAXYS1</Device>
332        <RunToCompletion>1</RunToCompletion>
333      </CPositioningDeviceScript>
334      <TargetPosition>
335        <Data>$z</Data>
336      </TargetPosition>
337      <Velocity>
```

```xml
338        <Data>25</Data>
339      </Velocity>
340    </Function>
341    <FunctionType>Show Message</FunctionType>
342    <Function class_id="9" class_name="QtLabb::Script::CMessageFunction"
             tracking_level="1" version="0" object_id="_30">
343      <IScriptFunction>
344        <Comment></Comment>
345        <Caption></Caption>
346      </IScriptFunction>
347      <Message>x default posotion = $xdef mm
348 x default posotion = $ydef mm
349 lowest z position = $z mm
350 lowest z position waste = $lowestzwaste mm
351 z-pitch = $stepZ mm
352 radius of circle = $r mm
353 angle pitch = $pitch
354 delay time = $wait s</Message>
355      <Type>1</Type>
356      <InterrupScript>0</InterrupScript>
357    </Function>
358    <FunctionType>Interrupt Script</FunctionType>
359    <Function class_id="10" class_name="QtLabb::Script::CInterruptFunction"
             tracking_level="1" version="0" object_id="_31">
360      <IScriptFunction>
361        <Comment></Comment>
362        <Caption></Caption>
363      </IScriptFunction>
364    </Function>
365    <FunctionType>StartCsvLogger</FunctionType>
366    <Function class_id="11" class_name="DataLogger::CStartStopLoggingScript"
             tracking_level="1" version="0" object_id="_32">
367      <IScriptFunction>
368        <Comment></Comment>
369        <Caption></Caption>
370      </IScriptFunction>
371      <Mode>1</Mode>
372      <LoggerType>1</LoggerType>
373    </Function>
374    <FunctionType>Conditional Loop</FunctionType>
375    <Function class_id="12" class_name="QtLabb::Script::CConditionalLoop"
             tracking_level="1" version="1" object_id="_33">
376      <IScriptFunction>
377        <Comment></Comment>
378        <Caption></Caption>
379      </IScriptFunction>
380      <ConditionType>0</ConditionType>
381      <Condition>$loopstotal</Condition>
382      <VariableName>$loops</VariableName>
383      <Operator>&lt;</Operator>
384      <Content object_id="_34">
385        <IScriptFunction>
386          <Comment></Comment>
387          <Caption></Caption>
388        </IScriptFunction>
389        <ParallelSequence>0</ParallelSequence>
390        <LinkedFile></LinkedFile>
391        <FunctionCount>25</FunctionCount>
392        <FunctionType>Wait For Process Data</FunctionType>
393        <Function class_id="13" class_name="QtLabb::Script::
               CWaitForProcessDataFunction" tracking_level="1" version="1"
               object_id="_35">
394          <IScriptFunction>
395            <Comment></Comment>
396            <Caption></Caption>
397          </IScriptFunction>
```

```
398            <Device>neMAXYS1_DigIN2</Device>
399            <Property>On</Property>
400            <ComparisonOperator>=</ComparisonOperator>
401            <CompareValue>
402              <Data>1</Data>
403            </CompareValue>
404          </Function>
405          <FunctionType>Capture Image</FunctionType>
406          <Function class_id="14" class_name="CameraView::CCaptureImageScript"
                 tracking_level="1" version="0" object_id="_36">
407            <CCameraScript class_id="15" tracking_level="0" version="1">
408              <IScriptFunction>
409                <Comment></Comment>
410                <Caption></Caption>
411              </IScriptFunction>
412              <Camera>Qmix_CAM_1</Camera>
413              <RoiConfig class_id="16" tracking_level="0" version="0">
414                <Keys></Keys>
415              </RoiConfig>
416              <CamSettingsMode>0</CamSettingsMode>
417            </CCameraScript>
418            <ImageFile>C:/Users/MF0485.A0404.002/Pictures/QmixElements/
                 QmixElements_Capture.jpg</ImageFile>
419          </Function>
420          <FunctionType>Start Timer</FunctionType>
421          <Function class_id="17" class_name="QtLabb::Script::CStartTimerFunction"
                 tracking_level="1" version="1" object_id="_37">
422            <IScriptFunction>
423              <Comment></Comment>
424              <Caption></Caption>
425            </IScriptFunction>
426            <TimerName>timer1</TimerName>
427            <Interval>$wait 0 0</Interval>
428          </Function>
429          <FunctionType>Set Variable</FunctionType>
430          <Function class_id_reference="3" object_id="_38">
431            <IScriptFunction>
432              <Comment></Comment>
433              <Caption></Caption>
434            </IScriptFunction>
435            <VariableName>$z</VariableName>
436            <VariableType>Calculation</VariableType>
437            <VariableValue>$z+$stepZ+$zdiff</VariableValue>
438            <CreateVariable>0</CreateVariable>
439          </Function>
440          <FunctionType>Move Z</FunctionType>
441          <Function class_id_reference="8" object_id="_39">
442            <CPositioningDeviceScript>
443              <IScriptFunction>
444                <Comment></Comment>
445                <Caption>Move Z Up</Caption>
446              </IScriptFunction>
447              <Device>neMAXYS1</Device>
448              <RunToCompletion>1</RunToCompletion>
449            </CPositioningDeviceScript>
450            <TargetPosition>
451              <Data>$z</Data>
452            </TargetPosition>
453            <Velocity>
454              <Data>25</Data>
455            </Velocity>
456          </Function>
457          <FunctionType>Capture Image</FunctionType>
458          <Function class_id_reference="14" object_id="_40">
459            <CCameraScript>
460              <IScriptFunction>
```

```
461            <Comment></Comment>
462            <Caption></Caption>
463          </IScriptFunction>
464          <Camera>Qmix_CAM_1</Camera>
465          <RoiConfig>
466            <Keys></Keys>
467          </RoiConfig>
468          <CamSettingsMode>0</CamSettingsMode>
469        </CCameraScript>
470        <ImageFile>C:/Users/MF0485.A0404.002/Pictures/QmixElements/
               QmixElements_Capture.jpg</ImageFile>
471      </Function>
472      <FunctionType>Set Variable</FunctionType>
473      <Function class_id_reference="3" object_id="_41">
474        <IScriptFunction>
475          <Comment></Comment>
476          <Caption></Caption>
477        </IScriptFunction>
478        <VariableName>$angle</VariableName>
479        <VariableType>Calculation</VariableType>
480        <VariableValue>$angle+$pitch</VariableValue>
481        <CreateVariable>0</CreateVariable>
482      </Function>
483      <FunctionType>Set Variable</FunctionType>
484      <Function class_id_reference="3" object_id="_42">
485        <IScriptFunction>
486          <Comment></Comment>
487          <Caption></Caption>
488        </IScriptFunction>
489        <VariableName>$u</VariableName>
490        <VariableType>Calculation</VariableType>
491        <VariableValue>Math.cos($angle*$PI/180)*$r+$xdef</VariableValue>
492        <CreateVariable>0</CreateVariable>
493      </Function>
494      <FunctionType>Set Variable</FunctionType>
495      <Function class_id_reference="3" object_id="_43">
496        <IScriptFunction>
497          <Comment></Comment>
498          <Caption></Caption>
499        </IScriptFunction>
500        <VariableName>$v</VariableName>
501        <VariableType>Calculation</VariableType>
502        <VariableValue>Math.sin($angle*$PI/180)*$r+$ydef</VariableValue>
503        <CreateVariable>0</CreateVariable>
504      </Function>
505      <FunctionType>Show Message</FunctionType>
506      <Function class_id_reference="9" object_id="_44">
507        <IScriptFunction>
508          <Comment></Comment>
509          <Caption></Caption>
510        </IScriptFunction>
511        <Message>Angle = $angle
512  Position X = $u
513  Position Y = $v
514  $loops / $loopstotal</Message>
515        <Type>1</Type>
516        <InterrupScript>0</InterrupScript>
517      </Function>
518      <FunctionType>Move XY</FunctionType>
519      <Function class_id_reference="5" object_id="_45">
520        <CPositioningDeviceScript>
521          <IScriptFunction>
522            <Comment></Comment>
523            <Caption></Caption>
524          </IScriptFunction>
525          <Device>neMAXYS1</Device>
```

```
526              <RunToCompletion>1</RunToCompletion>
527            </CPositioningDeviceScript>
528            <TargetPositionX>
529              <Data>$u</Data>
530            </TargetPositionX>
531            <TargetPositionY>
532              <Data>$v</Data>
533            </TargetPositionY>
534            <Axis1Velocity>
535              <Data>$speed</Data>
536            </Axis1Velocity>
537            <Axis2Velocity>
538              <Data>$speed</Data>
539            </Axis2Velocity>
540          </Function>
541          <FunctionType>Capture Image</FunctionType>
542          <Function class_id_reference="14" object_id="_46">
543            <CCameraScript>
544              <IScriptFunction>
545                <Comment></Comment>
546                <Caption></Caption>
547              </IScriptFunction>
548              <Camera>Qmix_CAM_1</Camera>
549              <RoiConfig>
550                <Keys></Keys>
551              </RoiConfig>
552              <CamSettingsMode>0</CamSettingsMode>
553            </CCameraScript>
554            <ImageFile>C:/Users/MF0485.A0404.002/Pictures/QmixElements/
                    QmixElements_Capture.jpg</ImageFile>
555          </Function>
556          <FunctionType>Set Variable</FunctionType>
557          <Function class_id_reference="3" object_id="_47">
558            <IScriptFunction>
559              <Comment></Comment>
560              <Caption></Caption>
561            </IScriptFunction>
562            <VariableName>$z</VariableName>
563            <VariableType>Calculation</VariableType>
564            <VariableValue>$z-$stepZ</VariableValue>
565            <CreateVariable>0</CreateVariable>
566          </Function>
567          <FunctionType>Move Z</FunctionType>
568          <Function class_id_reference="8" object_id="_48">
569            <CPositioningDeviceScript>
570              <IScriptFunction>
571                <Comment></Comment>
572                <Caption>Move Z Down</Caption>
573              </IScriptFunction>
574              <Device>neMAXYS1</Device>
575              <RunToCompletion>1</RunToCompletion>
576            </CPositioningDeviceScript>
577            <TargetPosition>
578              <Data>$z</Data>
579            </TargetPosition>
580            <Velocity>
581              <Data>25</Data>
582            </Velocity>
583          </Function>
584          <FunctionType>Capture Image</FunctionType>
585          <Function class_id_reference="14" object_id="_49">
586            <CCameraScript>
587              <IScriptFunction>
588                <Comment></Comment>
589                <Caption></Caption>
590              </IScriptFunction>
```

```
591         <Camera>Qmix_CAM_1</Camera>
592         <RoiConfig>
593           <Keys></Keys>
594         </RoiConfig>
595         <CamSettingsMode>0</CamSettingsMode>
596       </CCameraScript>
597       <ImageFile>C:/Users/MF0485.A0404.002/Pictures/QmixElements/
                QmixElements_Capture.jpg</ImageFile>
598     </Function>
599     <FunctionType>Wait for Timer</FunctionType>
600     <Function class_id="18" class_name="QtLabb::Script::
                CWaitForTimerFunction" tracking_level="1" version="0" object_id="
                _50">
601       <IScriptFunction>
602         <Comment></Comment>
603         <Caption></Caption>
604       </IScriptFunction>
605       <TimerName>timer1</TimerName>
606     </Function>
607     <FunctionType>Set Variable</FunctionType>
608     <Function class_id_reference="3" object_id="_51">
609       <IScriptFunction>
610         <Comment></Comment>
611         <Caption></Caption>
612       </IScriptFunction>
613       <VariableName>$z</VariableName>
614       <VariableType>Calculation</VariableType>
615       <VariableValue>$z+$stepZ</VariableValue>
616       <CreateVariable>0</CreateVariable>
617     </Function>
618     <FunctionType>Move Z</FunctionType>
619     <Function class_id_reference="8" object_id="_52">
620       <CPositioningDeviceScript>
621         <IScriptFunction>
622           <Comment></Comment>
623           <Caption>Move Z Up</Caption>
624         </IScriptFunction>
625         <Device>neMAXYS1</Device>
626         <RunToCompletion>1</RunToCompletion>
627       </CPositioningDeviceScript>
628       <TargetPosition>
629         <Data>$z</Data>
630       </TargetPosition>
631       <Velocity>
632         <Data>25</Data>
633       </Velocity>
634     </Function>
635     <FunctionType>Capture Image</FunctionType>
636     <Function class_id_reference="14" object_id="_53">
637       <CCameraScript>
638         <IScriptFunction>
639           <Comment></Comment>
640           <Caption></Caption>
641         </IScriptFunction>
642         <Camera>Qmix_CAM_1</Camera>
643         <RoiConfig>
644           <Keys></Keys>
645         </RoiConfig>
646         <CamSettingsMode>0</CamSettingsMode>
647       </CCameraScript>
648       <ImageFile>C:/Users/MF0485.A0404.002/Pictures/QmixElements/
                QmixElements_Capture.jpg</ImageFile>
649     </Function>
650     <FunctionType>Move XY</FunctionType>
651     <Function class_id_reference="5" object_id="_54">
652       <CPositioningDeviceScript>
```

```
653          <IScriptFunction>
654            <Comment></Comment>
655            <Caption></Caption>
656          </IScriptFunction>
657          <Device>neMAXYS1</Device>
658          <RunToCompletion>1</RunToCompletion>
659        </CPositioningDeviceScript>
660        <TargetPositionX>
661          <Data>$xdef</Data>
662        </TargetPositionX>
663        <TargetPositionY>
664          <Data>$ydef</Data>
665        </TargetPositionY>
666        <Axis1Velocity>
667          <Data>$speed</Data>
668        </Axis1Velocity>
669        <Axis2Velocity>
670          <Data>$speed</Data>
671        </Axis2Velocity>
672      </Function>
673      <FunctionType>Capture Image</FunctionType>
674      <Function class_id_reference="14" object_id="_55">
675        <CCameraScript>
676          <IScriptFunction>
677            <Comment></Comment>
678            <Caption></Caption>
679          </IScriptFunction>
680          <Camera>Qmix_CAM_1</Camera>
681          <RoiConfig>
682            <Keys></Keys>
683          </RoiConfig>
684          <CamSettingsMode>0</CamSettingsMode>
685        </CCameraScript>
686        <ImageFile>C:/Users/MF0485.A0404.002/Pictures/QmixElements/
                QmixElements_Capture.jpg</ImageFile>
687      </Function>
688      <FunctionType>Set Variable</FunctionType>
689      <Function class_id_reference="3" object_id="_56">
690        <IScriptFunction>
691          <Comment></Comment>
692          <Caption></Caption>
693        </IScriptFunction>
694        <VariableName>$z</VariableName>
695        <VariableType>Calculation</VariableType>
696        <VariableValue>$z-$stepZ-$zdiff</VariableValue>
697        <CreateVariable>0</CreateVariable>
698      </Function>
699      <FunctionType>Move Z</FunctionType>
700      <Function class_id_reference="8" object_id="_57">
701        <CPositioningDeviceScript>
702          <IScriptFunction>
703            <Comment></Comment>
704            <Caption>Move Z Down</Caption>
705          </IScriptFunction>
706          <Device>neMAXYS1</Device>
707          <RunToCompletion>1</RunToCompletion>
708        </CPositioningDeviceScript>
709        <TargetPosition>
710          <Data>$z</Data>
711        </TargetPosition>
712        <Velocity>
713          <Data>25</Data>
714        </Velocity>
715      </Function>
716      <FunctionType>Capture Image</FunctionType>
717      <Function class_id_reference="14" object_id="_58">
```

```
718          <CCameraScript>
719            <IScriptFunction>
720              <Comment></Comment>
721              <Caption></Caption>
722            </IScriptFunction>
723            <Camera>Qmix_CAM_1</Camera>
724            <RoiConfig>
725              <Keys></Keys>
726            </RoiConfig>
727            <CamSettingsMode>0</CamSettingsMode>
728          </CCameraScript>
729          <ImageFile>C:/Users/MF0485.A0404.002/Pictures/QmixElements/
                  QmixElements_Capture.jpg</ImageFile>
730        </Function>
731        <FunctionType>Set Variable</FunctionType>
732        <Function class_id_reference="3" object_id="_59">
733          <IScriptFunction>
734            <Comment></Comment>
735            <Caption></Caption>
736          </IScriptFunction>
737          <VariableName>$loops</VariableName>
738          <VariableType>Calculation</VariableType>
739          <VariableValue>$loops+1</VariableValue>
740          <CreateVariable>0</CreateVariable>
741        </Function>
742      </Content>
743    </Function>
744    <FunctionType>StopCsvLogger</FunctionType>
745    <Function class_id_reference="11" object_id="_60">
746      <IScriptFunction>
747        <Comment></Comment>
748        <Caption></Caption>
749      </IScriptFunction>
750      <Mode>0</Mode>
751      <LoggerType>1</LoggerType>
752    </Function>
753    <FunctionType>Show Message</FunctionType>
754    <Function class_id_reference="9" object_id="_61">
755      <IScriptFunction>
756        <Comment></Comment>
757        <Caption></Caption>
758      </IScriptFunction>
759      <Message>Operation finished.
760 $loopstotal positions dispensed.</Message>
761      <Type>1</Type>
762      <InterrupScript>0</InterrupScript>
763    </Function>
764    <FunctionType>Move Z</FunctionType>
765    <Function class_id_reference="8" object_id="_62">
766      <CPositioningDeviceScript>
767        <IScriptFunction>
768          <Comment></Comment>
769          <Caption></Caption>
770        </IScriptFunction>
771        <Device>neMAXYS1</Device>
772        <RunToCompletion>1</RunToCompletion>
773      </CPositioningDeviceScript>
774      <TargetPosition>
775        <Data>0</Data>
776      </TargetPosition>
777      <Velocity>
778        <Data>25</Data>
779      </Velocity>
780    </Function>
781    <FunctionType>Move XY</FunctionType>
782    <Function class_id_reference="5" object_id="_63">
```

```
783       <CPositioningDeviceScript>
784         <IScriptFunction>
785           <Comment></Comment>
786           <Caption></Caption>
787         </IScriptFunction>
788         <Device>neMAXYS1</Device>
789         <RunToCompletion>1</RunToCompletion>
790       </CPositioningDeviceScript>
791       <TargetPositionX>
792         <Data>0</Data>
793       </TargetPositionX>
794       <TargetPositionY>
795         <Data>0</Data>
796       </TargetPositionY>
797       <Axis1Velocity>
798         <Data>200</Data>
799       </Axis1Velocity>
800       <Axis2Velocity>
801         <Data>200</Data>
802       </Axis2Velocity>
803     </Function>
804   </FunctionSequence>
805 </boost_serialization>
```
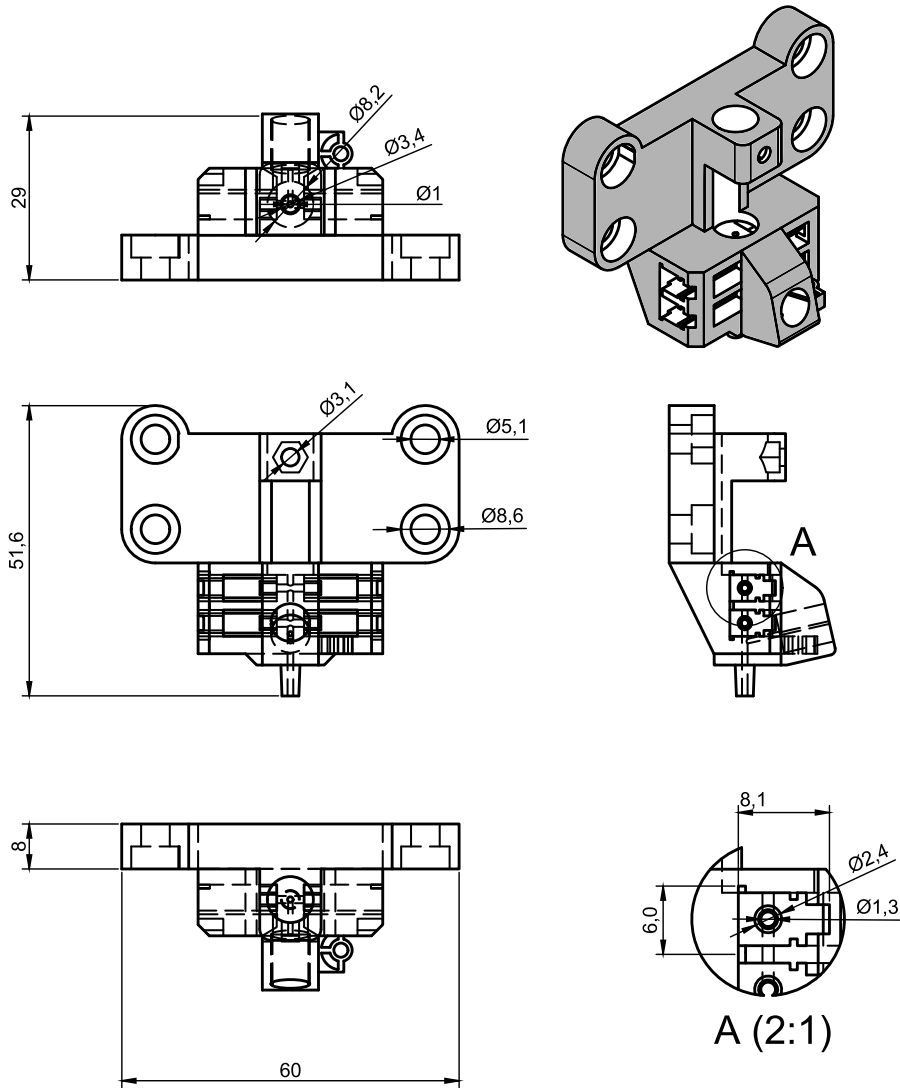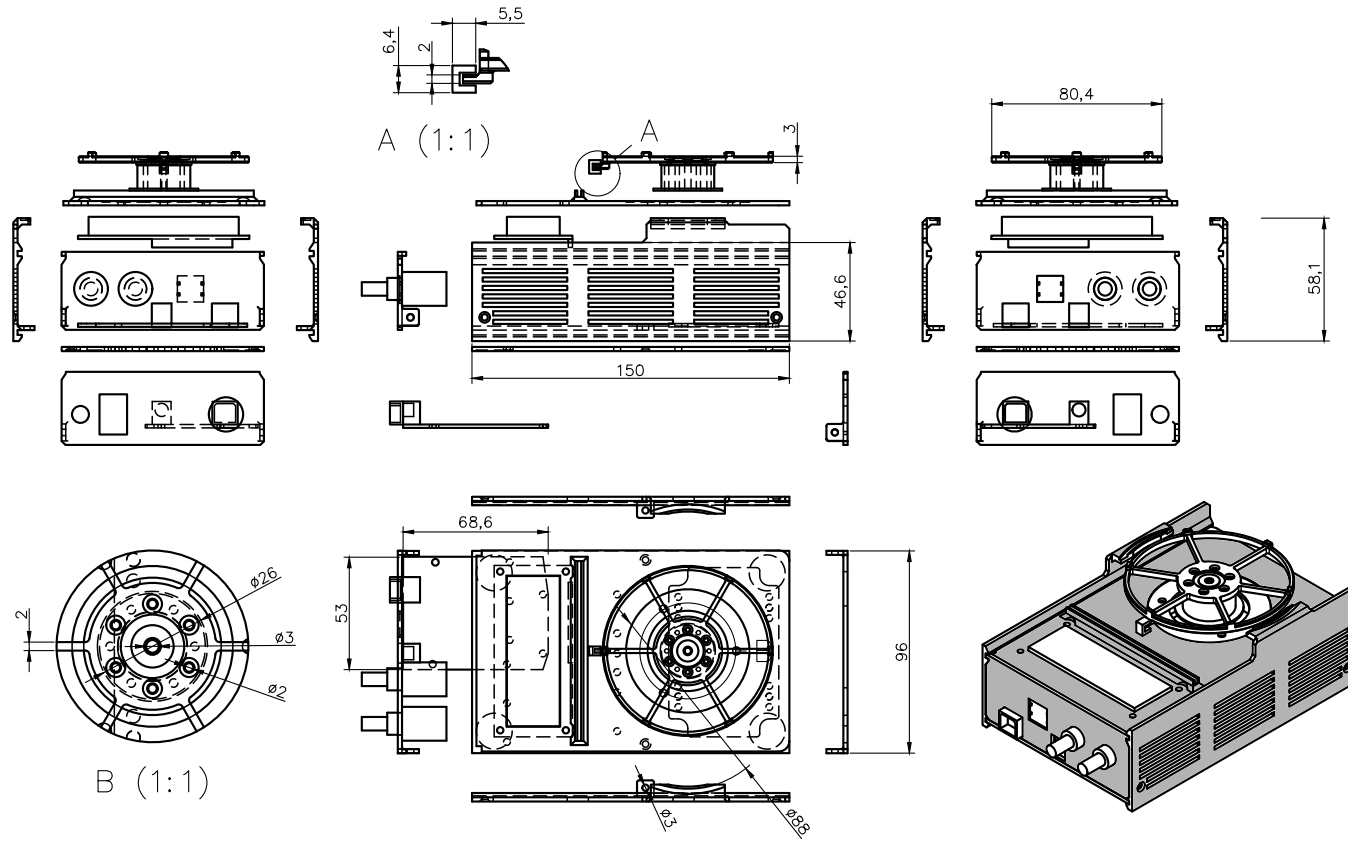
Figure 46: CAD drawing of developed droplet sensor.

Figure 47: CAD drawing of developed spincoater.

INDEX

CURRICULUM VITÆ

PERSONAL INFORMATION

Thomas Weber
Born 20.05.1985 in Lichtenstein (Saxony), Germany
Married to Azade Sanei-Weber

WORK EXPERIENCE

2018–today	Process engineer at Bilfinger Industrietechnik Salzburg Department pharmaceutical plant engineering
2017–2012	Doctoral student at Leibniz Institute for Natural Product Research and Infection Biology—Hans-Knöll-Institute Department Bio Pilot Plant, Microfluidics
03/2012–06/2012	Research assistant at Institute for photonic technologies, Jena Fields of research: RNA-Isolation, spectroscopic analyses of SERS-active substrates
03/2010–06/2010	Research assistant at Institute of physical chemistry, Friedrich-Schiller University Jena Fields of research: Raman spectroscopy of toxins, sample preparation

STUDY

2009–2012	Master of science in Pharma-Biotechnology at University of applied sciences Jena Thesis title: Optical detection of isolated RNA of Lactobacillus via magnetic microparticles
2006–2009	Bachelor of engineering in Biotechnology at University of applied sciences Jena Thesis title: Detection of heat shock proteins in human carcinoma cells in vitro after heat treatment

EDUCATION

2005	General qualification for university entrance at Goethe Gymnasium Chemnitz Main subjects Biology and German

MANUSCRIPT CONTRIBUTIONS

1. L. Mahler, M. Tovar, T. Weber, S. Brandes, M. M. Rudolph, J. Ehgartner, T. Mayr, M. T. Figge, M. Roth and E. Zang. 'Enhanced and homogeneous oxygen availability during incubation of microfluidic droplets'. *RSC Advances* 5 (123 2015), 101871–101878. DOI: 10.1039/C5RA20118G

   • Manuscript revisions
   • Experimental hard- and software support

2. M. Tovar, E. Zang and T. Weber. 'Device and method for extracting individual picoliter droplets from microfluidic emulsions for further analysis and scale-up'. EP3017868 A1. EP Patent App. EP20,150,193,893. 2016. URL: https://worldwide.espacenet.com/publicationDetails/biblio?CC=EP&NR=3017868A1&KC=A1&FT=D

   • Inventor and corresponding author
   • Writing of initial patent document
   • Design of patent figures
   • Revision and reference investigations

3. T. Weber, M. Tovar, L. Mahler and M. Roth. 'A microfluidic picoliter droplet based approach enabling an automatized ultrahigh throughput screening '. *18. Heiligenstädter Kolloquium*. Vol. 18. Institut für Bioprozess- und Analysenmesstechnik. 2016

   • First and corresponding author and presenter (see below)
   • Writing of manuscript
   • Performing and planning of experiments, data analysis

4. M. Tovar, T. Weber, S. Hengoju, A. Lovera, O. Shvydkiv and M. Roth. '3D-glass molds for facile production of complex droplet microfluidic chips'. *Biomicrofluidics* 12.2 (2018), 024115. DOI: 10.1063/1.5013325

   • Co-first author
   • Design and generation of 3D-CAD structures and graphics
   • Co-writing of initial document and revisions

5. M. Tovar, S. Hengoju, T. Weber, L. Mahler, M. Choudhary, T. Becker and M. Roth. 'One Sensor for Multiple Colors: Fluorescence Detection in Droplet Microfluidics Using Frequency-Division Multiplexing'. *Analytical Chemistry* 91.4 (Jan. 2019), 3055–3061. DOI: 10.1021/acs.analchem.8b05451

   • Revision of manuscript, graphic design
   • Support in hard- and software configuration

6. T. Weber, M. Tovar, S. Hengoju, O. Shvydkiv, M. Choudhary, L. Mahler, E. Zang and M. Roth. 'Recovery and isolation of individual microfluidic droplets by triggered deposition in wells or Petri dishes'. *in preparation* (2018)

   - Co-first and corresponding author
   - Experimental planning, hard- and software development, data analysis
   - Performing of experiments
   - Writing of initial manuscript and revisions

7. L. Mahler, K. Martin, T. Weber and M. Roth. 'Unravelling complex microbial communities inside microfluidic droplets using highly parallelized incubation and screening for natural product biosynthesis'. *in preparation* (2018)

   - Manuscript revision, graphic design
   - Experimental planning
   - Positioning and dispensing development

8. C.-M. Svensson, O. Shvydkiv, S. Dietrich, T. Weber, M. Choudhary, L. Mahler, M. Tovar, M. T. Figge and M. Roth. 'Coding of Experimental Conditions in Microfluidic Droplet Assays Using Colored Beads and Machine Learning Supported Image Analysis'. *Small* (Dec. 2018), 1802384. DOI: `10.1002/smll.201802384`

   - Manuscript revision
   - Technical support

POSTER

1. T. Weber, E. Zang, M. Tovar, P. Horbert, T. Henkel and M. Roth. 'Development of a refractivity based sensor for real time pico-litre droplet detection'. *European lab automation Hamburg*. 2013

2. T. Weber, E. Zang, M. Tovar, P. Horber, T. Henkel and M. roth. 'Construction of a refractivity sensor for real time picoliter droplet detection'. *7th Workshop of Chemical and Biological Micro Laboratory Technology*. 2013

3. T. Weber, M. Tovar, L. Mahler and M. Roth. 'Automatized deposition of individual, single picoliter droplets from microfluidic emulsions'. *8th Workshop of Chemical and Biological Micro Laboratory Technology*. 2016

4. T. Weber, M. Tovar, L. Mahler, M. Roth and J. M. Köhler. 'An ultrahigh throughput screening approach via fully automated sorting and depositing of microfluidic single picoliter droplets'. *EMBL Conference Microfluidics*. 2016

TALKS

1. T. Weber, M. Tovar, L. Mahler and M. Roth. 'A microfluidic pico-liter droplet based approach enabling an automatized ultrahigh throughput screening '. *18. Heiligenstädter Kolloquium*. Vol. 18. Institut für Bioprozess- und Analysenmesstechnik. 2016

2. T. Weber, M. Tovar, L. Mahler, M. Roth and J. M. Köhler. 'An ultrahigh throughput screening approach via fully automated sorting and depositing of microfluidic single picoliter droplets'. *EMBL Conference Microfluidics*. 2016

3. T. Weber. 'Empowering droplet microfluidics for biotechnological processes with technical and optical research'. *Jahreskongress Biotechnologie 2020+ − InfectControl 2020*. 2016

*Nature is inexorable and immutable;
she never transgresses the laws imposed upon her, or cares a whit
whether her abstruse reasons and methods of operation
are understandable to men.*

— Galileo Galilei

ACKNOWLEDGEMENTS

I would like to thank first of all everybody who supported me in all respects during this time.

Most important I would like to thank my beloved wife *Azade*. You have been there for me in good and bad days regardless of any circumstances.

DECLARATION

I certify that I prepared the submitted thesis independently without undue assistance of a third party and without the use of others than the indicated aids. Data and concepts directly or indirectly taken over from other sources have been marked stating the sources.

When selecting and evaluating the following materials, the persons listed below helped me in the way described respectively for a charge/free of charge[1]):

    1. . . . .

    2. . . . .

    3. . . . .

Further persons were not involved in the content-material-related preparation of the thesis submitted. In particular, I have not used the assistance against payment offered by consultancies or placing services (doctoral consultants or other persons). I did not pay any money to persons directly or indirectly for work or services which are related to the content of the thesis submitted.

So far the thesis has not been submitted identically or similarly to an examination office in Germany or abroad.

I have been notified that any incorrectness in the submitted above mentioned declaration is assessed as attempt to deceive and, according to § 7 para. 10 of the PhD regulations, this leads to a discontinuation of the doctoral procedure.

Ilmenau, April 2019   . . . .
                                                            Signature

---

1 Delete as applicable.